Application of biomimetic high valence state iron complexes to contaminant oxidation

Author:
Chang, Yingyue

Publication Date:
2018

DOI:
https://doi.org/10.26190/unsworks/3621

Application of biomimetic high valence state iron complexes to contaminant oxidation

Yingyue Chang

A thesis in fulfilment of the requirements for the degree of

Doctor of Philosophy

School of Civil and Environmental Engineering

Faculty of Engineering

August 2018

Thesis/Dissertation Sheet

Surname/Family Name	:	**Chang**
Given Name/s	:	**Yingyue**
Abbreviation for degree as give in the University calendar	:	**PhD**
Faculty	:	**Engineering**
School	:	**Civil and Environmental Engineering**
Thesis Title	:	**Application of biomimetic high valence state iron complexes to contaminant oxidation**

Abstract 350 words maximum: (PLEASE TYPE)

Catalysed oxidation processes are of interest in water/wastewater treatment for recalcitrant pollutant degradation. Inspired by natural oxidative enzymes, iron complexes that can be activated to a high valence state are recognized as potential potent oxidation catalysts though there are still significant gaps with regard to their application in ambient aqueous environments. Investigating iron complexes with such potential and studying their application to degradation of organic contaminants pushing them further in that direction is thus important to harness this potential in real technologies. In this thesis, two iron complexes studied are Fe-TAML (TAML = tetraamido macrocylic ligand) and Fe-tpena (tpena– = N,N,N'-tris(2-pyridylmethyl)ethylenediamine-N'-acetate).

To enhance feasibility, Fe-TAML is immobilized by graphite and used to catalyze rhodamine B (RhB) degradation by both hydrogen peroxide and electrolysis. RhB can be efficiently degraded by both activation methods in the presence of Fe-TAML/Graphite. The graphite support not only largely reduces Fe-TAML concentration in the liquid phase, it also facilitates RhB degradation in different ways: on one hand, it enriches RhB concentration at the liquid-solid interface which results as an immediate degradation upon peroxide addition; on the other hand, it enhances electron transfer and thus enables Fe(IV)TAML generation which is hardly detected in homogenous condition. In comparison, electrochemical activation enables Fe(IV)-TAML to degrade RhB at neutral pH rather than the basic pH used for peroxide activation.

To better understand the behaviour of Fe-tpena in aqueous solution, this thesis examines a range of methods for its homogeneous activation including electrolysis, hydrogen peroxide, and hypochlorite; all of which have been found to show promise for contaminant degradation. At potentials higher than 1.3V (vs NHE), Fe-tpena can be activated to Fe(IV)-tpena at its natural pH of ~3; the resulting Fe(IV)-tpena solution is relatively stable and has shown oxidative activity toward various substances including RhB and formate. Activated by peroxide at circumneutral pH, Fe-tpena can catalyze RhB or formate degradation through generating both HO• and Fe(IV)-tpena. While HO• leads to significant destruction of the Fe-tpena complex, activation by hypochlorite leads to more extensive Fe(IV)-tpena generation and greater stability of the Fe-tpena complex.

FOR OFFICE USE ONLY Date of completion of requirements for Award:

ORIGINALITY STATEMENT

‘I hereby declare that this submission is my own work and to the best of my knowledge it contains no materials previously published or written by another person, or substantial proportions of material which have been accepted for the award of any other degree or diploma at UNSW or any other educational institution, except where due acknowledgement is made in the thesis. Any contribution made to the research by others, with whom I have worked at UNSW or elsewhere, is explicitly acknowledged in the thesis. I also declare that the intellectual content of this thesis is the product of my own work, except to the extent that assistance from others in the project's design and conception or in style, presentation and linguistic expression is acknowledged.’

Signed …….....

Date …….....

COPYRIGHT STATEMENT

AUTHENTICITY STATEMENT

INCLUSION OF PUBLICATIONS STATEMENT

UNSW is supportive of candidates publishing their research results during their candidature as detailed in the UNSW Thesis Examination Procedure.

Publications can be used in their thesis in lieu of a Chapter if:

- The student contributed greater than 50% of the content in the publication and is the "primary author", ie. the student was responsible primarily for the planning, execution and preparation of the work for publication
- The student has approval to include the publication in their thesis in lieu of a Chapter from their supervisor and Postgraduate Coordinator.
- The publication is not subject to any obligations or contractual agreements with a third party that would constrain its inclusion in the thesis

Please indicate whether this thesis contains published material or not.

☐ *This thesis contains no publications, either published or submitted for publication*

☒ *Some of the work described in this thesis has been published and it has been documented in the relevant Chapters with acknowledgement*

☐ *This thesis has publications (either published or submitted for publication) incorporated into it in lieu of a chapter and the details are presented below*

CANDIDATE'S DECLARATION

I declare that:

- I have complied with the Thesis Examination Procedure
- where I have used a publication in lieu of a Chapter, the listed publication(s) below meet(s) the requirements to be included in the thesis.

Name	**Signature**	**Date (dd/mm/yy)**
Yingyue Chang		

Abstract

Catalysed oxidation processes are of interest in water and wastewater treatment for recalcitrant pollutant degradation. Inspired by natural oxidative enzymes, iron complexes that can be activated to a high valence state are recognized as potential potent oxidation catalysts though there are still significant gaps with regard to their application in ambient aqueous environments. Investigating iron complexes with such potential and systematically studying their application to degradation of organic contaminants is thus important to harness this potential in real technologies. In this thesis, two iron complexes are studied: Fe-TAML (TAML = tetraamido macrocylic ligand) and Fe-*tpena* (*tpena*$^{-}$ = *N*,*N*,*N*'-tris(2-pyridylmethyl)ethylenediamine-*N*'-acetate).

Fe-TAML has been previously widely studied in aqueous solution, however, in order to enhance feasibility, in this thesis Fe-TAML was immobilized to graphite and used to catalyze rhodamine B (RhB) degradation, with activation of the Fe-TAML by both hydrogen peroxide and electrolysis. RhB can be efficiently degraded by both activation methods in the presence of Fe-TAML/Graphite. The graphite support not only largely reduces Fe-TAML concentration in the liquid phase, it also facilitates RhB degradation in different ways: on one hand, it enriches RhB concentration at the liquid-solid interface which results as an immediate degradation upon H_2O_2 addition; on the other hand, it enhances electron transfer and thus enables Fe^{IV}-TAML generation which is hardly detected in homogenous condition. In comparison, electrochemical activation enables Fe^{IV}-TAML to degrade RhB at neutral pH rather than the basic pH used for H_2O_2 activation.

Fe-*tpena* has had little previous research other than demonstration of its ability to support an Fe^{IV} oxidation state. To better understand the behaviour of Fe-*tpena* in aqueous solution, this thesis examines a range of methods for its homogeneous activation including electrolysis, H_2O_2, and hypochlorite; all of which have been found to show promise for contaminant degradation. At potentials higher than 1.3 V (vs NHE), Fe-*tpena* can be activated to Fe^{IV}- *tpena* at its natural pH of ~3, with the resulting Fe^{IV}-

tpena solution relatively stable (in the absence of substrates) and found to exhibit extensive oxidative activity toward various substances including RhB and formate.

H_2O_2 activation of Fe-*tpena* at circumneutral pH was also found to be effective, with the oxidation of RhB or formate also demonstrated, however, H_2O_2 activation resulted in the formation of both $HO^{\bullet}$ and Fe^{IV}-*tpena*, with $HO^{\bullet}$ leading to significant undesirable destruction of the Fe-*tpena* complex. Activation of Fe-*tpena* by hypochlorite was also found to be effective, with more extensive Fe^{IV}-tpena generation observed coupled with greater stability of the Fe-*tpena* complex.

Acknowledgments

At first, I would like to express my deepest gratitude to my supervisor Professor David Waite and co-supervisor Dr. Christopher Miller for their guidance, support, and encouragement throughout the whole journey. None of this work would be possible without their input. I would also like to thank my colleagues in the Water Research Centre for inspiration I have gained through interacting with them, in particular to Dr. An Ninh Pham and Dr. Jeffrey Huijie Yu.

Special thanks to Professor Christine McKenzie and her group from the University of Southern Denmark for providing the iron complex and any necessary support for this work, especially to Dr. David de Sousa for collaborating with me on the electrochemical experiments.

I would like to thank UNSW for providing a supportive research environment with all sorts of high-quality services including child care centers, IT and health center, and various professional development programs that have enriched my candidature.

Finally, I am very grateful to my husband Lei Cui and my daughter Phoebe for their love and accompany. I am also deeply indebted to my parents and family in China for their unconditional support.

Table of Contents

Chapter 1.
Introduction

Oxidation, a common process in nature, is also employed in water and wastewater treatment, with use of oxidants much more powerful than oxygen required for effective pollutant decomposition, especially for non-biodegradable compounds. A popular choice of potent oxidants are reactive oxygen species (ROS), with processes for their generation referred to as "advanced oxidation processes (AOPs)" (Glaze et al., 1987). Another option that has been proposed in recent years involves high valence state iron complexes with these species similar in nature and function to oxidation-catalysing enzymes. Numerous studies of the use of biomimetic complexes have been described with a wide variety of ligands, oxidants, solvents and reaction conditions employed for different potential applications (Que and Tolman, 2008, Costas et al., 2000, Collins and Ryabov, 2017). Given our interest in examining the potential use of biomimetic high valence state iron complexes in water/wastewater treatment, we focus here on aqueous-favouring Fe^{IV} systems and their activity toward both simple organic ompounds as well as examples of common pollutants.

In this chapter, studies of high-valent iron complexes, especially those have been or can be used to degrade contaminants in an aqueous environment, are reviewed following presentation of an overview of popular AOPs. Details of the planned research is provided in Section 1.6.

1.1 Advanced oxidation processes

While oxidizing agents such as ozone and hydrogen peroxide (H_2O_2) have been used widely for disinfection purposes in water treatment, potential exists for combining these moderate strength oxidants with either additional energy dissipation or chemical

additives resulting in the generation of strongly oxidising hydroxyl radicals ($HO^{\bullet}$) that, in turn, can be applied to degrade recalcitrant organic pollutants.

One way of producing $HO^{\bullet}$ is to use transition-metal catalysts such as iron ions in combination with H_2O_2 via the so-called Fenton reaction: $Fe^{2+} + H_2O_2 + H^+ \rightarrow Fe^{3+} + H_2O + HO^{\bullet}$ (Brillas et al., 2009, Fenton, 1894). If performed under strongly acidic conditions (normally at pH 3), the process can be catalytic with the Fe^{3+} resulting from the primary reaction re-reduced to Fe^{2+} via reaction with H_2O_2 and the hydroperoxyl radical, $HO_2^{\bullet}$ (Duesterberg et al., 2005). A homogenous Fenton process requires a considerable amount of ferrous ion to be effective with this resulting in extensive generation of waste ferric oxyhydroxide sludge. One possible way to avoid this generation of excessive waste is to make use of nano-zero valent iron (Babuponnusami and Muthukumar, 2014, Joo et al., 2004) though this material will eventually oxidize resulting in a mixture of iron oxyhydroxides (Ma et al., 2016). Other heterogeneous options in include iron oxides and hydroxides and transition metal substituted iron oxides (Pouran et al., 2014). However, most Fenton variants still require acidic conditions though the heterogeneous counterparts usually favour a broader pH range. This often requires addition of acid and must then be countered by base addition after treatment to bring the pH back to near neutral for discharge.

Other AOPs, involving technologies such as photocatalysis, electrolysis, ultrasound irradiation, and their combinations with Fenton process, often require high cost while lacking good energy efficiency (Pignatello et al., 2006, Vilhunen and Sillanpaa, 2010, Brillas et al., 2009). Besides UV source, photocatalysis also requires the presence of a semiconducting material that is photoactive, stable and non-toxic such as TiO_2 (Kanakaraju et al., 2014). Sometimes photocatalysis is combined with ozonation to induce better pollutant degradation performance with this approach considered more cost-effective in spite of the requirement of additional energy for ozone generation (Mehrjouei et al., 2015). Electrochemical AOPs, having been applied to full-scale water treatment recently, suffer from high electrode prices, especially the most popular boron-doped diamond electrodes (Sires et al., 2014). Some other options of electrodes for production of $HO^{\bullet}$ include doped-SnO_2, PbO_2, doped-TiO_2 and suboxides of TiO_2 (Chaplin, 2014). Ultrasound irradiation is barely used alone because of ineffectiveness

and is usually combined with other AOPs to achieve further contaminant degradation (Sathishkumar et al., 2016).

In all the above-mentioned AOPs, $HO^{\bullet}$ is the main active oxidant and, while a very powerful oxidant, is non-selective and exhibits high activity toward common anions such as chloride with unwanted byproducts such as chlorate reducing pollutant degradation efficiency and inducing toxicity problems (Bergmann et al., 2014, Kiwi et al., 2000).

1.2 Biomimetic iron-based complexes

In contrast to above-mentioned struggles in finding proper catalysts for AOPs, nature never lacks efficient catalysts for oxidation reactions. Three common oxidative enzymes that use dioxygen (O_2) or H_2O_2 as the primary oxidant are the cytochrome P450 enzymes, peroxidases, and dioxygenases with most of these enzymes found to generate high-valent iron intermediates as key species according to a wide range of experimental and theoretical studies (Nam, 2007, Bassan et al., 2006, Nam et al., 2014, Rittle and Green, 2010). Scientists have invested considerable effort in developing analogues of cytochrome P450 enzymes and peroxidases (Collins, 1994, Gu et al., 2014, Rutkowska-Zbik et al., 2014). These biomimetic Fe^{III} compounds can form high-valent iron (Fe^{IV} or Fe^{V}) complexes which are strongly oxidising and could be a promising technology for contaminant oxidation (Collins and Walter, 2006, Engelmann et al., 2016).

Synthetic iron porphyrins have been used as models for peroxidase and cytochrome P450 in biomimetic studies since the 1980s (Groves et al., 1981, Groves et al., 1979). Although a catalytic mechanism involving putative oxoiron(IV) porphyrin π-cation radical species was already established at that time, it was not until the late 2000s that direct experimental evidence was provided to prove that Fe^{IV}-oxo intermediates, rather than oxidant-Fe(III) porphyrin intermediates, are actually the active oxidants (Hessenauer-Ilicheva et al., 2007, Han et al., 2008). Either way, there is no doubt Fe porphyrins are capable of catalysing various oxidative reactions such as alkane hydroxylation (Lim et al., 1999, Nam et al., 1999) and olefin epoxidation (Kumar et al.,

2013, Nam et al., 2002) and can be used not only in organic solution but also in aqueous solution (Oszajca et al., 2014).

In environmentally-relevant research, a common application of the Fe^{IV}-porphyrin system is the degradation of chlorophenols in wastewater and soil. To reduce the formation of toxic byproducts such as dioxin during chlorophenols oxidation, Fukushima and co-workers introduced humic substances into the Fe-porphyrin/$KHSO_5$ system to incorporate the chlorinated intermediates (Fukushima et al., 2003a) and found that humic substances containing less aromatic moieties and carboxylic groups were more effective (Fukushima et al., 2003b). By introducing Fe-porphyrin into functionalized humic acid, they obtained more stable catalysts and further hindered the formation of toxic byproducts (Fukushima et al., 2010). Other oxygen donors such as H_2O_2 (Hahn et al., 2007) or even dissolved oxygen in the presence of light (Šmejkalová and Piccolo, 2006) were also found to be effective. An Fe-porphyrin/H_2O_2 system has been found effective in treating olive mill waste waters, whose major components are phenolic compounds (Celano et al., 2008).

However, chlorophenols were not fully mineralized in the processes mentioned above. Their removal by Fe^{IV}-porphyrin systems is generally referred to as coupling or polymerization, because the phenolic moieties were oxidized by Fe^{IV} porphyrin cation radicals and transformed into free radicals which are then stabilized by spontaneous coupling and thus avoid further biodegradation (Šmejkalová et al., 2006, Fontaine and Piccolo, 2012). Therefore, porphyrin based high-valent iron species seem to be less robust than what is needed; energy input like illumination is sometimes still needed to enhance their performance to some extent (Fontaine et al., 2014).

Besides working as homogeneous catalysts as mentioned above, Fe-porphyrins have also been immobilized on solid supports including electrodes, which could enable the recycling and reuse of the catalysts, activation of the catalysts in a more sustainable manner or introduce other possibilities. For example, a heterogeneous Fe-porphyrin/SiO_2 material prepared by Christoforidis et al. (2010) showed better catalytic activity than the homogeneous counterpart, and Fe^{IV} intermediates were found when activated by $NaIO_4$. Halma et al. (2009) reported that employing layered double

hydroxide as a support for Fe-porphyrin can change the efficiency and selectivity of the catalysts. A modified electrode prepared by Tu et al. (2010) consisting of an Fe-porphyrin supported on nitrogen-doped multiwalled carbon nanotubes showed good catalytic activity for electrooxidation of sulfite.

Another common biomimetic complex that structurally resembles porphyrin is phthalocyanine. Usually used heterogeneously and assisted by illumination, iron-phthalocyanine has been found to be effective in desulfurization of fuels (Liu et al., 2017) and degradation of organic pollutants, in the presence of H_2O_2 or peroxymonosulfate (Han et al., 2016, Zhu et al., 2017, Wang et al., 2017, Chen et al., 2017, Wu et al., 2017). In these processes, Fe^{IV} oxo complexes are working together with free radicals $HO^{\bullet}$ and $SO_4^{\bullet}$ with the free radicals usually serving as the main active oxidants.

1.3 Iron TAML

To make high valence state iron more accessible, Collins and colleagues (Collins et al., 1998) focused on strongly σ-donating chelates with high anionic charge and successfully developed the tetraamido macrocyclic ligands (TAML), which are now the most famous and advanced peroxidase mimics. In Fe-TAML systems, while Fe^{IV} species – Fe^{IV}-O-Fe^{IV} units – can be generated in dichloromethane when reacted with oxygen under mild conditions (Ghosh et al., 2005), there is also evidence that Fe^{V}-oxo intermediates are formed in the presence of peracid in *n*-butyronitrile at -60 ℃ (Tiago de Oliveira et al., 2007). More facile generation of Fe^{V}-oxo has been achieved very recently with modified TAML ligands with activation methods including hypochlorite activation at 13 ℃ in water (Mills et al., 2016), electrochemical activation in 0.1 M HNO_3 (Demeter et al., 2014), and m-chloroperbenzoic acid activation in different solvents (Ghosh et al., 2017). In comparison with the analogues of cytochrome P450 and the peroxidases, Fe-TAML systems have been shown to possess much more potent catalytic activity.

To date, Fe-TAML has been used in lab-scale studies to remove a range of contaminants from water at ambient temperature and pressure. Dye removal has been of

particular interest since modern dyes are usually found very resistant to conventional technologies. A fundamental study by Chahbane et al. (2007b) showed that the azo dye Orange II can be degraded rapidly by more than 60% by Fe-TAML/H_2O_2 system at pH 10, generating small biodegradable and mineralization products such as CO_2, CO, phthalic acid, formic acid and oxalic acid. Beach et al. (2011) reported that the commercial azo dye tartrazine can be degraded by more than 90% to environmentally benign and biodegradable products by Fe-TAML/H_2O_2 at optimized dosing and alkaline conditions (pH > 9). Besides these simple solutions, real-world wastewater, such as pulp and paper mill effluents (Wingate et al., 2004) and textile effluents (Chahbane et al., 2007a) can also be efficiently decolourized by TAML/H_2O_2 system at pH 11. In all these studies, alkaline conditions are required since the performance strongly depends on pH.

Besides dyes, Fe-TAML/H_2O_2 systems have also showed efficiency in degradation of other important persistent contaminants such as organophosphorus pesticides (Chanda et al., 2006a), active pharmaceutical ingredients (Shen et al., 2011) and endocrine disrupting chemicals (Shappell et al., 2008). One study by Collins's group (Sen Gupta et al., 2002) that has drawn particularly wide attention to the Fe-TAML/H_2O_2 system showed that chlorophenols can be efficiently degraded to biodegradable small molecules and inorganic matter at pH 10 with other technologies and high-valent iron systems unable to induce such effective degradation. The Fe-TAML/H_2O_2 system has also been tested at neutral pH and shown to result in near complete degradation of pentachlorophenol but only after 12 hours using the most active Fe-TAML which has a CF_2 tail. Such fluorine-tailed Fe-TAML/H_2O_2 systems with chlorine heads has also been found efficient in removing mono- and di-nitrophenolic pollutants from water at pH 8 (Kundu et al., 2015).

Despite the broad spectrum efficacy of Fe-TAMLs, some issues remain to be addressed before their application in large-scale water treatment can be realised. Firstly, the widely-studied first generation Fe-TAMLs are most effective at pH around 10 and much less effective at circumneutral pH and undergo slow self-destruction over the course of the oxidation reaction because of a suicide inactivation process (Chanda et al., 2006b). Although a variety of alternate TAML ligands have been developed (Collins and

Ryabov, 2017), they lack comprehensive study. For now, $Fe^{IV/V}$-TAMLs are still quite unstable in aqueous conditions at room temperature given their fast reaction with water (Ellis et al., 2010) with such a trait clearly undesirable in water treatment processes.

Unknown toxicity is another issue. Generally used as a homogeneous catalyst, most Fe-TAML would remain in the effluent. Although Fe-TAML catalysts are composed of low-toxicity elements, their influence on human or environmental health remains unclear. Studies have shown that TAML activators are not toxic to zebrafish at low concentrations but morphological malformations were observed for some Fe-TAML catalysts at relatively high concentration (Truong et al., 2013). Pending sufficient research on the toxicity of Fe-TAML, it is important that the release of residual Fe-TAML in the effluent be minimized with such an approach also likely to be more cost-effective.

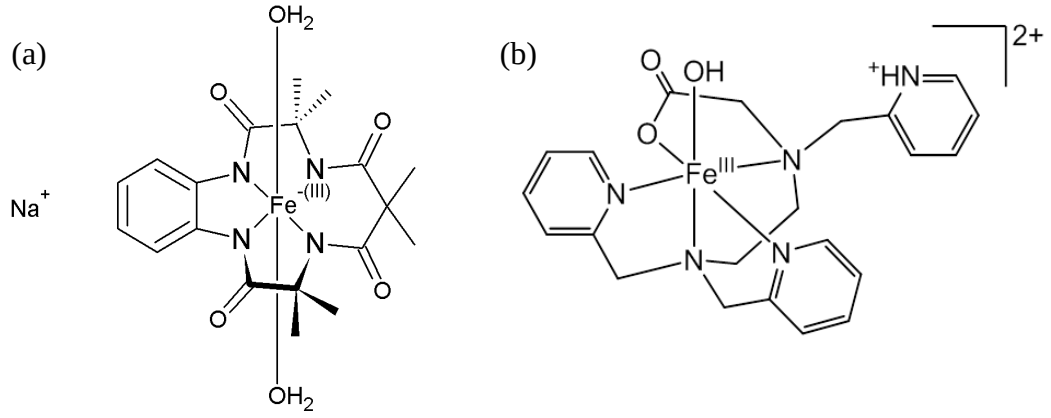

Figure 1-1 Fe-TAML (a) and Fe-*tpena* (b) used in this work

1.4 Fe-*tpena*

Besides the well-developed Fe-porphyrin, phthalocyanine and TAML systems, there are identified Fe(IV) species supported by other kinds of ligands that have received minimal investigation to date with regard to their potential use in water and wastewater treatment applications. One that has come to our attention is an aqueous non-heme Fe^{III} system with a carboxylate-containing hexadentate ligand, Fe-*tpena* (*tpena*$^{-}$ = *N*,*N*,*N*'-

tris(2-pyridylmethyl)ethylenediamine-*N*'-acetate), developed by Prof. C.J. McKenzie and her group at the University of Southern Denmark.

As a newly developed ligand, works related to *tpena* are rare but interesting. The *tpena* ligand contains a carboxylate donor as do many non-heme dioxygenases and such ligands have demonstrated oxygen activating ability when combined to cobalt (Vad et al., 2011). When combining to Fe, an aqueous Fe^{IV}-oxo complex can form upon the activation by cerium(IV) ammonium nitrate (Vad et al., 2012). A more gentle activation by a commonly used oxyen transfer agent – iodosylarene – has also been applied with chemically masked non-heme Fe^{V} species proposed to be the active oxidant (Lennartson and McKenzie, 2012). Of particular interest is that the high-valent Fe-*tpena* has an overall positive charge and thus strongly electrophilic. With iodosylbenzene activation, Fe-*tpena* has been used for sulfoxidation and epoxidation with Fe^{IV} species formed in gas-phase but not in solution (de Sousa et al., 2016).

According to the various studies conducted by McKenzie's group, *tpena* is a dioxygenase with a neutral ligand that is electrophilic with high-valent iron complex that is stable in water but not in organic solutions. All these features benefit organic pollutant oxidation in water yet has not been investigated further.

1.5 Key research gaps

As well developed ligands, iron porphyrin and phthalocyanine systems have been used for contaminant oxidation in a variety of ways including in attached form to solid supports that enable ligand recycle. However, interest in these systems for water-treatment purposes is shifting to more robust hypervalent iron complexes. Replacing Fe-porphyrins with complexes such as Fe-TAML could result in more robust catalysts.

Studies on Fe-TAML have mostly been undertaken in homogeneous conditions to date, leaving Fe-TAML in the effluent and introducing an unknown risk to receiving waters. A heterogeneous counterpart with similar catalytic activity could not only reduce this risk, but may also improve the stability and catalytic activity of Fe-TAML as has been achieved in the Fe-porphyrin system. However, few heterogeneous catalysts based on Fe-TAML have been reported to date except a couple of Fe-TAML modified electrodes.

For example, an Fe^{III}/Fe^{IV} oxidation in an Fe-TAML modified electrode has been reported by (Demeter et al., 2014), suggesting the material as a promising electrocatalyst for oxygen evolution reactions. Wang and co-workers (Wang et al., 2010) also reported good electrocatalytic performance toward hydrogen peroxide of an Fe-TAML modified electrode. To make Fe-TAML more suitable for water treatment, further study of electro-oxidation reactions catalysed by Fe-TAML modified electrodes would seem promising, as would other means of using immobilized heterogeneous Fe-TAML catalysts.

As for other underdeveloped hypervalent iron precursors, Fe-*tpena* stands out as a potential candidate for contaminant oxidation in aqueous conditions in two aspects. Firstly, the Fe^{IV} oxo species is relatively stable in slightly acidic to neutral aqueous solution and exhibits a half-time of more than one hour in the absence of oxidisable species, which is orders-of-magnitude greater than that observed for Fe^{IV}-TAML (~3 min as reported by Chanda et al. (2006b)). Secondly, the Fe-*tpena*$^{-}$ system has an overall positive charge, which is favourable for oxidising electron-rich substrates. Despite these positive aspects the application of the promising Fe-*tpena* system is hindered by the absence of any investigation of its catalytic performance.

In conclusion, Fe-porphyrin is currently the most well-studied high valent iron system but lacks competency in treatment applications, while Fe-TAML catalysts have demonstrated efficiency in degrading a wide range of contaminants but need to be further developed to be more feasible for water/wastewater treatment. As for other systems, Fe-*tpena* could make a better catalyst than Fe-porphyrin and Fe-TAML given its potent oxidizing ability, neutral optimal pH and positive charge, but has yet to be investigated for this application.

1.6 Thesis focus

To propel the application of high valent iron complexes for contaminant oxidation in water treatment processes, this thesis aims to answer the following questions:

1) As the currently most advanced type in this group, how could Fe-TAML be better applied to water contaminant oxidation in terms of recyclability?

2) Seeming to possess promising characteristics for application in aqueous conditions, how would Fe^{IV}-*tpena* behave as an oxidant when activated in a sustainable manner?

Chapter 2 is focussed on answering the first question by preparing immobilized Fe-TAML which is then utilized for dye removal upon proper activation. A typical first generation Fe-TAML (Figure 1-1a) is used in this work.

Chapter 3 - 5 is focussed on answering the second question with investigation of the activation of Fe-*tpena* by electrochemical means, peroxide addition and hypochlorite addition. The Fe^{III}-*tpena* ($[Fe^{III}2(\mu\text{-}O)(tpenaH)_2](ClO_4)_4$) used in this study (Figure 1-1b) is provided by Professor C.J. McKenzie and her group from the University of Southern Denmark who are collaborating closely with us on this aspect of the work. Results in Chapter 3 have been published in: *de Sousa, D. P., Miller, C. J., Chang, Y., Waite, T. D. & Mckenzie, C. J. 2017. Electrochemically Generated cis-Carboxylato-Coordinated Iron(IV) Oxo Acid–Base Congeners as Promiscuous Oxidants of Water Pollutants. Inorganic Chemistry, 56, 14936-14947*

An overall methodology flow chart for the work presented in this thesis is shown in Figure 1-2.

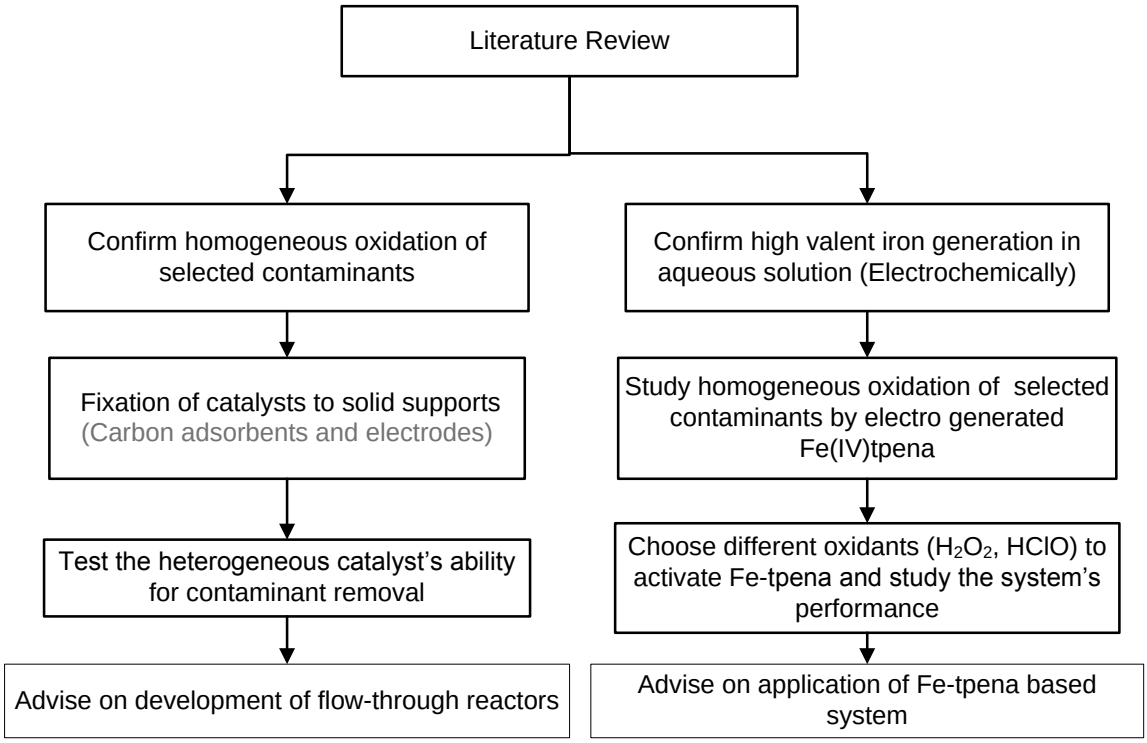

Figure 1-2 Research methodology

Chapter 2.
Rhodamine B removal catalysed by immobilized Fe-TAML

2.1 Introduction

As demonstrated in Chapter 1, the most widely used activating oxidant in aqueous conditions for Fe-TAML is H_2O_2. However, it has been reported that Fe-TAMLs display both peroxidase-like and catalase-like activity when used as H_2O_2 activator (Ghosh et al., 2008). This means, after having been activated by H_2O_2, the oxidized high valent Fe species can either be deactivated by H_2O_2 and generate O_2 (catalase activity), or oxidize substrate (peroxidase activity) (Ryabov, 2013). Although peroxidase-like activity usually dominates in the presence of electron donor substrates, H_2O_2 dosage used in current studies are usually tens or even hundreds of equivalence of the target substrate. These excess concentrations of H_2O_2 could induce deactivation of the high valence state iron species and reduce their efficiency for contaminant degradation. As such, an approach whereby H_2O_2 is introduced in some "slow bleed" manner will be required in order to achieve higher degradative efficiency and an overall faster degradation.

Another possible activation that eliminates the above-mentioned problem is electro-chemical activation. Electrochemically formation of Fe^{IV}-TAML species established by differential pulse voltammetry in water at a quite basic pH of 12.6 has been reported by Popescu et al. (2010). Having found that homogeneous Fe-TAML generate poor cyclic votammograms, Demeter et al. (2014) immobilized Fe-TAML on electrodes using black carbon which can enhance oxygen evolution in acidic condition. There are barely no

other convincing studies of electro-activated Fe-TAML nor their use for contaminant oxidation.

Besides optimising the activation methods, immobilising the compounds is also one way to render these compounds more suitable for water treatment which makes them recyclable and removable at the end of the treatment. In addition to the above-mentioned carbon black, another solid support that has been used for Fe-TAML is pyrolytic graphite reported by Wang et al. (2010): with the ligand incorporated in sodium alginate and then attached to the electrode, the catalyst shows activity towards hydrogen peroxide but electrochemical formation of high-valent iron species was not established. Being chemically stable and electro-active, carbon materials represent potentially excellent solid supports though the activity of immobilized Fe-TAML needs to be examined in further detail.

In this chapter, Fe-TAML will be affixed to graphite and the ability of the supported Fe-TAML to degrade rhodamine B (RhB) upon H_2O_2/electro-chemical activation will be examined and compared to the effectiveness of homogenous Fe-TAML. RhB is chosen in part because it is a convenient model refractory organic dye but also because the concentrations of RhB and its de-ethylated products are easy to quantify using UV-vis spectroscopy.When activated by H_2O_2, the consumption of H_2O_2 will also be monitored, which, together with rhodamine species variation, could shed some light on the mechanism operating. Additionally, the effect of a variety of system variables on the catalytic performance of graphite supported Fe-TAML will be examined including pH, Fe-TAML loading, H_2O_2 dosage and initial RhB concentration.

2.2 Materials and methods

2.2.1 Reagents and materials

Rhodamine B (Laser grade, 99+%) was obtained from Acros, Fe-TAML was purchased from GreenOx Catalysts Inc. and methanol (200 proof, HPLC/Spectrophotometric grade) was obtained from Sigma–Aldrich. Graphite (SP-1, spectroscopic powders) was supplied by Bay Carbon Inc. All other reagents were at least of analytical reagent grade

and used without further purification. All solutions were prepared in 18 MΩ cm Milli-Q water (mQ) from a Millipore Milli-Q system.

Standard commercial electrodes were purchased from ALS (Japan). Glassy carbon electrodes (CH104 from www.chinstruments.com) were polished sequentially with 1.5 mm α-Al_2O_3 and 0.3 mm α-Al_2O_3 to mirror like surface and washed with MQ water. Graphite felt (99%, G100PAN-based battery felt, AVCarb) was purchased from FuelCellStore.com and was pre-treated by sonication under heating in methanol followed by repeated sonication in water and thorough drying to ensure removal of all traces of methanol. The graphite felt was then sonicated and washed with MQ water before use. A microAg/AgCl reference (leak-free) electrode was made by casing a AgCl coated Ag-wire in a ~0.3 mm Ø PTFE tube fitted with a microporous frit (custom-made).

A 20.0 mM H_2O_2 stock solution and stock solutions of 100 μM Amplex Red (AR; Invitrogen) mixed with 50 U/mL horseradish peroxidase (HRP) for H_2O_2 determination were prepared and stored as previously undertaken in Prof. T. David Waite's research group (Garg et al., 2007).

2.2.2 Preparation of Fe-TAML/Graphite

Fe-TAML/Graphite (FeTG) was prepared by direct adsorption in methanol. A certain amount of Fe-TAML was dissolved in certain volume of methanol, with the original concentration determined by UV-vis spectrum using a Cary 50 spectrophotometer. 2.0 g graphite was then added to the Fe-TAML methanol solution and shaken vigorously. The mixture was then sonicated for 30 minutes, sealed and left in the dark to settle out for an hour. Afterwards, the sludge was centrifuged until clear. Subsequently, a certain amount of supernatant was taken out and scanned by UV-vis to determine the amount of Fe-TAML adsorbed onto the graphite. The remaining sludge was then dried in a 40 ℃ oven. The dried solid was then resuspend in mQ water and shaken vigorously to wash off loosely adsorbed Fe-TAML. The volume and Fe-TAML concentration in supernatant were then measured to calculate the Fe-TAML present in the solid phase. The final FeTG solid was obtained after 2-3 times mQ wash with no Fe-TAML detected in the supernatant.

A stock solution for glass carbon electrode modification (for CV measurements) was prepared by adding 85:15 w/w% Fe–TAML/graphite (50 mg) and nafion binder (190 μL of a 5 wt% stock, 8.2 mg) in isopropanol (810 μL). The resulting mixture was shaken thoroughly and sonicated to obtain a homogeneous ink before use.

2.2.3 RhB removal by H_2O_2 activated Fe-TAML

FeTG was weighed (25 mg) and dispersed into 20 mL of rhodamine B solution in carbonate buffer of a particular pH. The suspension was then stirred at room temperature for 30 min to achieve adsorption equilibrium. H_2O_2 stock solution was then added to the suspension to final H_2O_2 concentration of 100 μmol/L. At certain time intervals, 1 mL of the reaction solution was removed and then centrifuged to remove the residual catalysts. The supernatant was then diluted to 3 mL by pH 4 acetate buffer to stop potential reactions of leached Fe-TAML. The UV–vis spectrum and fluorescence spectrum of the diluted supernatant was then determined for rhodamine species concentrations and H_2O_2 concentration, respectively. Dissolved Fe-TAML was also used for RhB degradation in the same procedure without centrifugation as a comparison with an equivalent amount of Fe-TAML used.

2.2.4 RhB removal by electrochemically activated Fe-TAML/Graphite

In addition to H_2O_2-activated FeTG, the ability of electrochemically activated FeTG to oxidise RhB was also examined. In these studies, the activation voltage was controlled using a CH Instruments 600D electrochemical work station. Cyclic Voltammetry (CV) was performed first to confirm the feasibility of electo-activation, using a conventional 3-eletrode setup consisting of a glassy carbon working electrode, a platinum counter electrode and a Ag/AgCl (3 M KCl) reference electrode. The glassy carbon electrode was modified with FeTG by carefully dropping a certain amount of the FeTG/nafion ink on to the surface. Blank graphite/nafion ink was used for comparison.

For bulk electrolysis experiments, graphite felt electrodes with titanium wires (1.5 × 1.5 × 0.4 cm) were employed as the cathode and anode with the microAg/AgCl (3 M KCl) used as the reference electrode. All electrochemical experiments in this portion of the study were conducted in a 0.1 M $NaClO_4$ electrolyte (pH ~6.5) without any pH control.

FeTG (25 mg as free particals) and RhB (10 μM) were added to 20 mL of electrolyte. The suspension was then stirred at room temperature for 30 min to achieve adsorption equilibrium before introducing the electrodes. At the end of the experiment (2 hour reaction), the suspension was centrifuged at 4000 RPM to separate the graphite particles, which were then soaked in a certain amount of methanol to extract adsorbed species. The carbon felt electrodes were washed in the same way in order to determine the amounts of adsorbed rhodamine species.

2.2.5 Data analysis

RhB and the N-deethylated rhodamine chromophores, namely N,N,N'-triethyl-rhodamine (TER), N,N'-diethyl-rhodamine (DER), N-ethyl-rhodamine (MER) and rhodamine (Rh) were analysed by UV-vis spectra and a Microsoft Excel-assisted deconvolution process as published previously (Miller et al., 2013).

H_2O_2 concentrations were measured by the HRP-catalyzed oxidation of AR using a Cary Eclipse spectrophotometer. The diluted supernatant withdrawn from the reactor was then further diluted to a 0.1-1 μmol/L H_2O_2 concentration range by pH 8.0 carbonate buffer and then mixed in a quartz cuvette with AR/HRP stock solution to final AR and HRP concentrations of 2.0 μmol/L and 1.0 kU/L, respectively.

To minimize the influence of rhodamine chromophores, three points of the fluorescence spectrum were used to calculate H_2O_2 concentration, including [Ex585, Em600] (AR without much RhB interference, but weak), [Ex575, Em585] (highest H_2O_2 in presence of RhB) and [Ex550, Em570] (highest RhB in presence of H_2O_2). The concentration of H_2O_2 was then calculated as follows:

$$\begin{bmatrix} F(585,600) \\ F(575,585) \\ F(550,570) \end{bmatrix} = \begin{bmatrix} S_{1,H_2O_2} & S_{1,RhB} \\ S_{2,H_2O_2} & S_{2,RhB} \\ S_{3,H_2O_2} & S_{3,RhB} \end{bmatrix} \times \begin{bmatrix} [H_2O_2] \\ [RhB] \end{bmatrix}$$

$$F = SC$$

$$S^T F = S^T SC$$

$$\left(S^T S\right)^{-1} S^T F = \left(S^T S\right)^{-1} S^T SC$$

$$C = \left(S^T S\right)^{-1} S^T F$$

where S is the matrix of the slopes obtained from H_2O_2 and RhB standard solutions.

All potentials are given *versus* the normal hydrogen electrode (NHE). Experimental potentials measured *vs.* Ag/AgCl (3 M KCl) were referenced to the NHE by adding +0.21 V. Potentials measured *vs.* microAg/AgCl (3 M KCl) were referenced to the NHE by adding +0.25 V. These calibration values were determined using the redox potential of the $[Fe^{III}(CN)_6]^{3-}$ / $[Fe^{II}(CN)_6]^{4-}$ (HCF) couple (10 mM, 0.5 M KCl, $E_{½}$ = 0.456 V *vs.* NHE) (Hanania et al., 1967) as standard:

$$E(Ag/AgCl\ vs.NHE) = 0.456\,V - E(HCF\ vs.Ag/AgCl)$$

2.3 Results and discussion

2.3.1 RhB degradation by dissolved Fe-TAML/H_2O_2

RhB removal by dissolved Fe-TAML/H_2O_2 was first examined and results shown in Figure 2-1. 10 μM RhB can be degraded to an undetectable level in the presence of 3.1 μmol/L Fe-TAML with two additions of H_2O_2 under homogeneous conditions (Figure 2-1a) with about 2 μM of the final oxidation product rhodamine (Rh) and ~2.6 μM Fe-TAML (determined by UV, spectrum not shown) remaining in solution. De-ethylated rhodamine species in the order TER, DER and Rh are formed as ethyl groups are removed sequentially from RhB. The fact that the presence of MER was undetectable could be attributed to the fragility of the one last ethyl group on rhodamine.

To investigate the durability of Fe-TAML, four sequential additions of RhB were added within a 60-minute interval (Figure 2-1b). RhB reduction becomes slower as activation proceeds with the accumulation of TER, DER and Rh indicative of the deactivation of the catalyst. All in all, RhB can be efficiently degraded by dissolved Fe-TAML, mainly via a deethylation pathway though some is directly oxidised.

In both sets of studies, H_2O_2 is always exponentially consumed after addition of each spike (insert figures in Figure 2-1). H_2O_2 consumption is much slower in the absence of RhB but Fe-TAML deactivation was much more severe given that the third spike of H_2O_2 is barely consumed (Figure 2-2). H_2O_2 consumption by Fe-TAML mainly involves the activation/re-activation of Fe-TAML (where Fe^{IV}-O-Fe^{IV} dimer is dominant with possibly Fe^{III}-O-Fe^{IV} formed but no Fe^{V}, according to detailed studies published by Collins' group (Collins and Ryabov, 2017, Tang et al., 2015, Mills et al., 2015)) and intra- and intermolecular ("suicide") inactivation (Chanda et al., 2006b). As RhB also quenches the Fe^{IV} species, Fe-TAML self-destruction is blocked to some extent because of competition and H_2O_2 is consumed faster on activation as a result of the faster regeneration of the rest state Fe-TAML. In other words, in terms of contaminant degradation, excess H_2O_2 leads to lower efficiency because of its high activity towards high valent Fe-TAML species, which would result in a significant deactivation of the catalyst over time. Similar behaviour has also been reported for Fe-N4Py (N4Py = 1,1-bis(pyridin-2-yl)-N,N-bis(pyridin-2-ylmethyl)methanamine) (Chen et al., 2018); when excess H_2O_2 is used, the key intermediate species (Fe^{III}–OOH) for Fe^{IV}=O formation reacts mainly with H_2O_2, forming resting-state Fe^{III} species rather than Fe^{IV}, which largely reduces its catalytic efficiency.

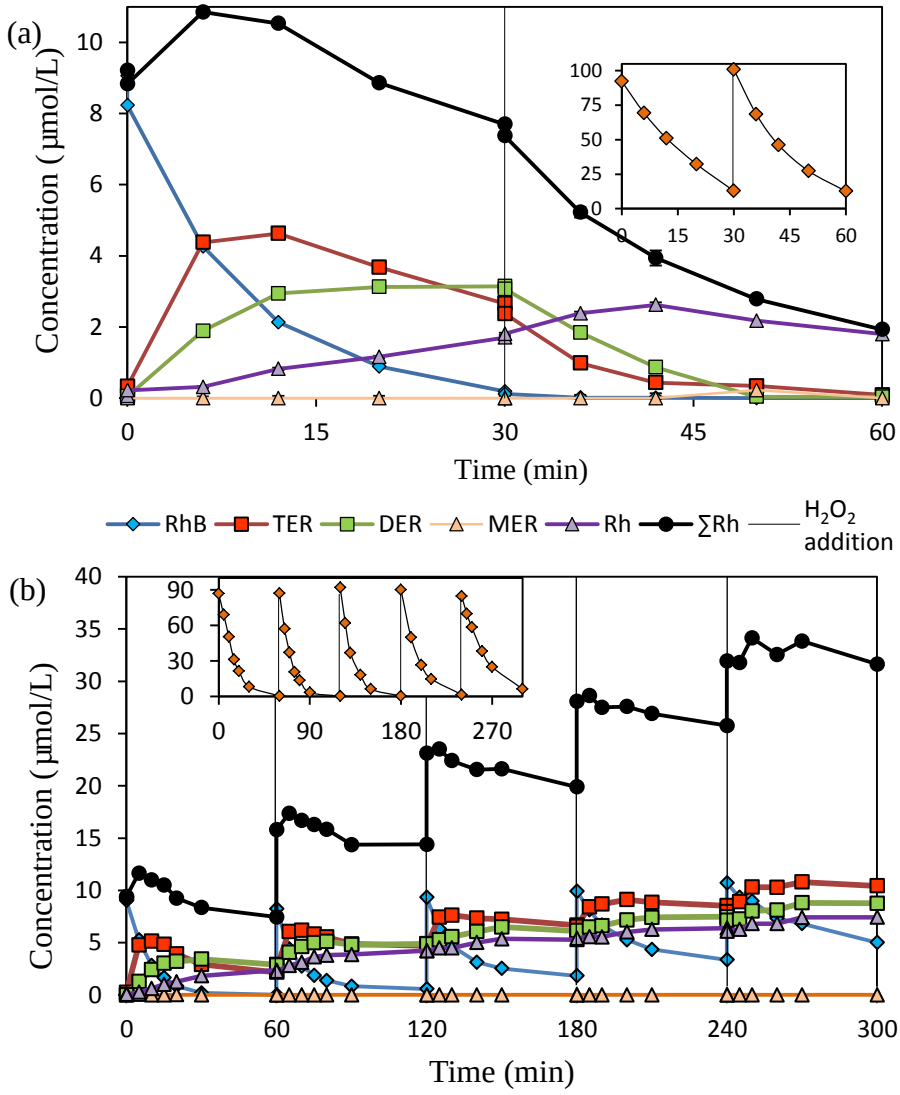

Figure 2-1. RhB removal by dissolved Fe-TAML and sequential addition of H_2O_2 (a) without and (b) with sequential addition of RhB at pH 9.0. Initial RhB, 10 μmol/L; H_2O_2 dosage in each addition, 100 μM; Fe-TAML dosage: ~3.1 μmol/L added at 0 min. Insert figures are the corresponding H_2O_2 concentration.

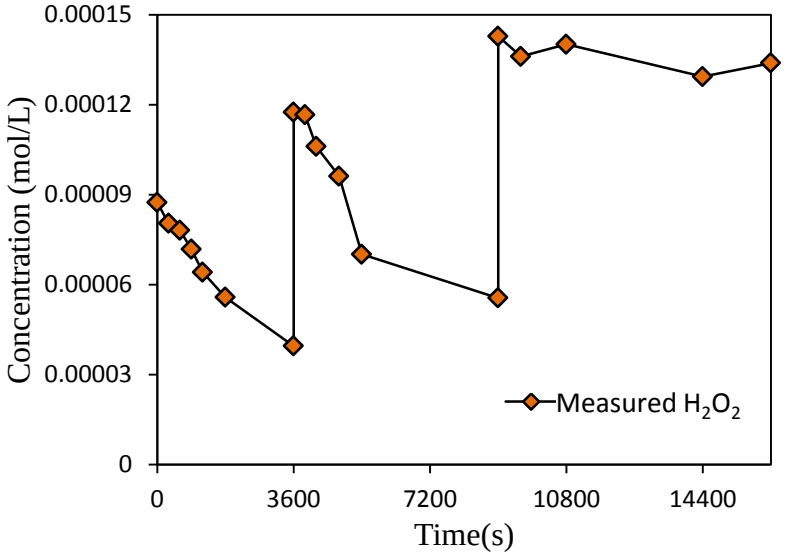

Figure 2-2 H_2O_2 consumption by Fe-TAML without RhB . H_2O_2 dosage in each addition, 100 μmol/L; Fe-TAML dosage: ~3.1 μmol/L.

2.3.2 RhB degradation by H_2O_2 activated Fe-TAML/Graphite

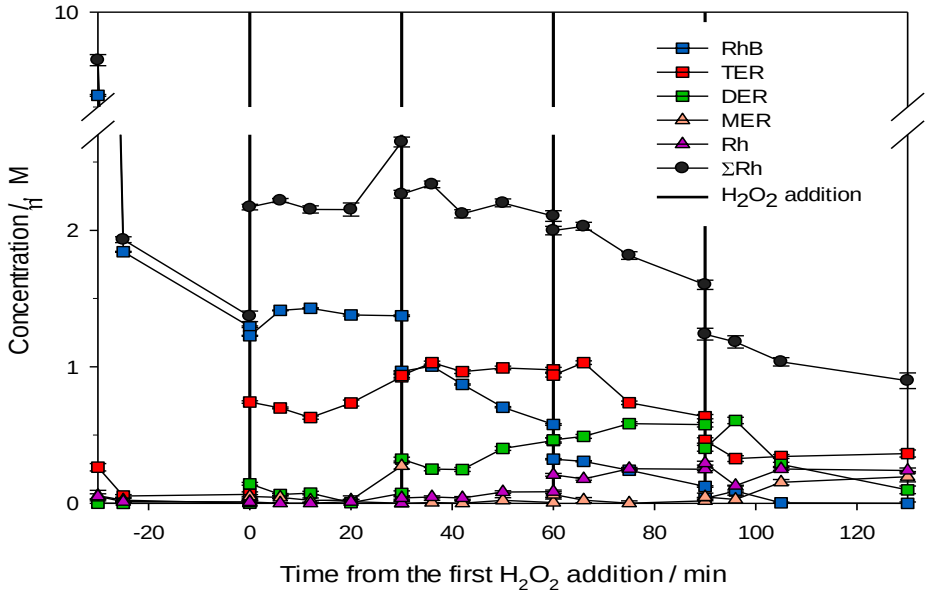

Figure 2-3. RhB removal by graphite-supported Fe-TAML (FeTG) at pH 9.0. Initial RhB, 10 μM; H_2O_2 dosage in each addition, 100 μmol/L; FeTG dosage: 1.25 g/L (containing Fe-TAML 2.5 μmol/g, added at -30 min).

Following investigation of the homogeneous degradation of RhB by Fe-TAML/H_2O_2, Fe-TAML was fixed to graphite and the rate and extent of RhB degradation in this heterogeneous system investigated. As shown in Figure 2-3, 10 μM RhB is reduced to undetectable levels by FeTG (Fe-TAML/Graphite) at a loading equivalent to that of Fe-TAML in the homogeneous study and with four additions of H_2O_2. As can be seen from the extent of RhB removal prior to addition of H_2O_2, more than 80% of RhB immediately adsorbed to the graphite support. At the end of this 2 hour study, less than 1 μM of total rhodamine, mainly composed of TER and Rh, remains in the liquid phase, with undetectable concentrations of Fe-TAML in solution. A rapid initial "burst" of degradation can be observed with each addition of H_2O_2, followed by slow ongoing degradation. The slightly increased concentration of RhB apparent in the first time interval could be attributed to the desorption of loosely-attached RhB. In summary, FeTG can significantly reduce the amount of Fe-TAML leakage in liquid phase, but required two more aliquots of H_2O_2 to remove ~10 μM RhB compared with that in the homogeneous case.

The different behaviour of the heterogeneous and homogeneous systems with regard to RhB degradation can be attributed to the different degradation efficiencies of the high-valent iron species generated in each case. Compared with dissolved Fe-TAML, attached Fe-TAML shows high degradative efficiency immediately on H_2O_2 addition, but degradative efficiency slows down over time. The rapid initial "burst" of degradation was presumably associated with the high localised concentrations of RhB and activated TAML at the graphite surface with resultant high initial rates of degradation. The subsequent slower rate of degradation may relate to transport limitations in regeneration of the TAML catalyst and/or excessive deactivation of the catalyst given the relatively high concentration of H_2O_2 used. Utilisation of different methods of introducing H_2O_2 may result in higher rates of ongoing RhB degradation without compromising Fe^{IV} generation.

Similar with the reaction pathway proposed for the homogeneous case, RhB degradation by graphite-supported Fe-TAML and H_2O_2 involves reactions including, but not limited to: 1) activation and deactivation of attached Fe-TAML, 2) free rhodamine species degradation by attached Fe-TAML, and 3) adsorption-desorption

processes between rhodamine species and graphite. Compared to the homogeneous case, rhodamine species are more likely to be bleached by attached Fe^{IV} species due to pre-concentration on the surface in the heterogeneous case and attached Fe^{IV} species inactivation significantly reduced, with intermolecular inactivation non-existent because of low mobility and the rate of intramolecular inactivation reduced.

2.3.3 Effects of reaction conditions on the performance of H_2O_2 activated Fe-TAML/Graphite

2.3.3.1 Effects of pH

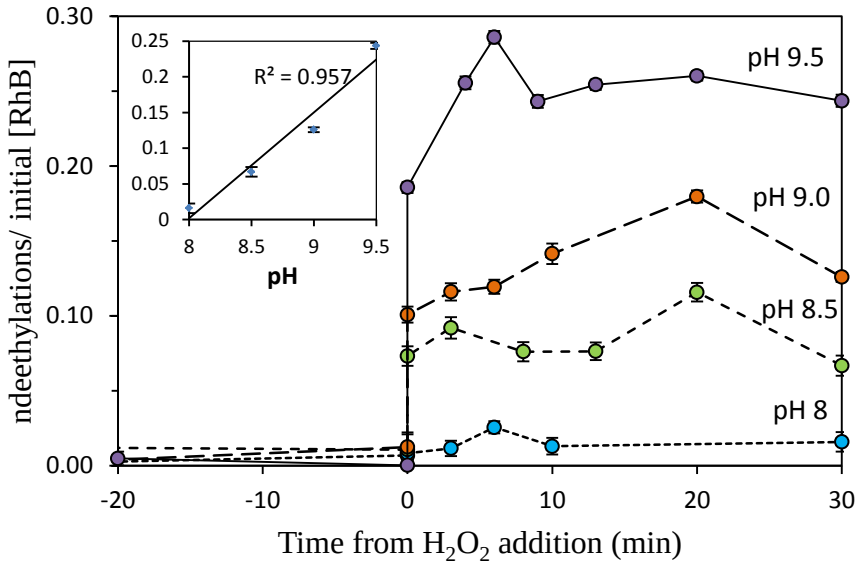

Figure 2-4. Deethylation ratio of initial [RhB] at different pHs. Initial RhB, ~10 μM; FeTG dosage, 1.25 g/L (containing Fe-TAML3.6 μmol/g); H_2O_2 dosage, 100 μmol/L, added at 0 min; ndeethylations = [TER] + 2[DER] + 3[MER] + 4[Rh]. Insert figure is the deethylation ratio at 30 min as a function of pH.

With one addition of H_2O_2, the main RhB degradation process in the presence of FeTG is just deethylation where the concentration of total rhodamine species (∑Rh) is barely changed as shown in Figure 2-3 (0-30 min). This provides a means of simplifying the results as the extent of RhB degradation can be expressed as the deethylation ratio of initial RhB (*ndeethylations*/initial[RhB], *where ndeethyations* = [TER] + 2[DER] +

3[MER] + 4[Rh]). The pH dependence of the deethylation ratio of initial RhB is shown in Figure 2-4 with these results demonstrating that FeTG is more effective in basic conditions. Although the non-chromophoric products and attached de-ethylated rhodamine species caused an underestimation of the extent of *deethylation*, FeTG activity still exhibited an obvious positive correlation with pH in the range of 8.0 ~ 9.5 (insert figure in Figure 2-4). As a compromise in need for base addition to raise the pH to a value where FeTG is effective, the effect of other factors that have an influence on RhB removal performance will be examined at pH 9.

2.3.3.2 Effects of Fe-TAML Loading

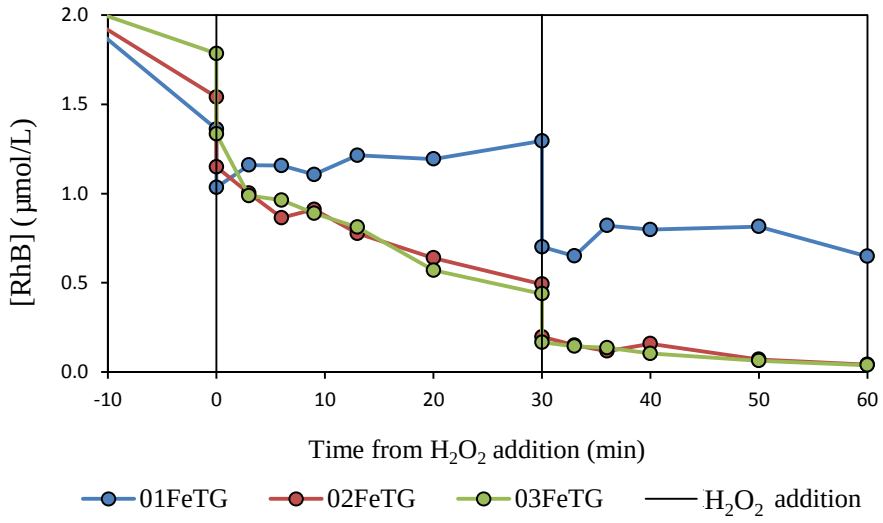

Figure 2-5. RhB concentration variation with time when 1.25g/L FeTG with different Fe-TAML loadings (01FeTG, 2.2 μmol/g; 02FeTG, 4.1 μmol/g; 03FeTG, 6.6 μmol/g) and two addition (0min and 30 min) of 100 μM H_2O_2 are employed at pH 9. Initial RhB, ~10 μmol/L.

Three batches of FeTGs with different Fe-TAML loadings – 01FeTG (2.2 μmol Fe-TAML /g, similar to the FeTG used obove), 02FeTG (4.1 μmol Fe-TAML /g) and 03FeTG (6.6 μmol Fe-TAML /g) – were prepared and used to catalyse RhB (10 μmol/L) removal with H_2O_2 (100 μmol/L). RhB can be reduced to a concentration of less than 0.05 μM by 1.25 g/L 02FeTG and 03FeTG with two additions of H_2O_2, while 01FeTG can only achieve a 0.65 μM RhB residual under the same conditions (Figure 2-5)

despite the fact that 01FeTG had adsorbed the most RhB. As a result, increasing the loading of Fe-TAML on graphite can significantly increase the catalytic activity of the material. However, at a relatively high Fe-TAML loading (4.1 μmol/g), higher Fe-TAML loading did not result in further reduction of RhB in the liquid phase.

To investigate the extent of rhodamine species remaining in the solid phase, a low RhB concentration (~5 μmol/L) was employed to ensure that a colourless supernatant could be achieved after adsorption by different FeTGs (1.25 g/L). Before H_2O_2 addition, the concentration of RhB in the liquid phase was less then 0.02 μmol/L (data not shown) with more than 99.5% of the RhB in the solid phase. The speciation of RhB and products was measured by UV spectral analysis of the methanol extractions of different FeTGs as shown in Figure 2-6.

For 01 FeTG, up to 75% of the RhB in the solid phase remains unchanged because immobilized Fe-TMAL and RhB cannot react with each other. The small extent of degradation that is observed most likely occurs as a result of the interaction of attached Fe-TAML with the dissolved rhodamine that is in equilibrium with the RhB that is present on the surface of the graphite particles. As Fe-TAML loading increases, the chance of oxidation increases, resulting in higher proportion of de-ethylated rhodamine species in the solid phase. For 03FeTG, at an Fe-TAML loading 3 times as high as 01FeTG, the deethylation ratio increases by approximately 20 times. The deethylation ratio of ~1.2 for 03FeTG indicates that one RhB molecule had reacted with high-valent-iron species at least 1.2 times on average with this value much higher than that for 01FeTG and 02FeTG. This value possibly includes contributions from an undetectable amount of leached Fe-TAML considering the high loading.

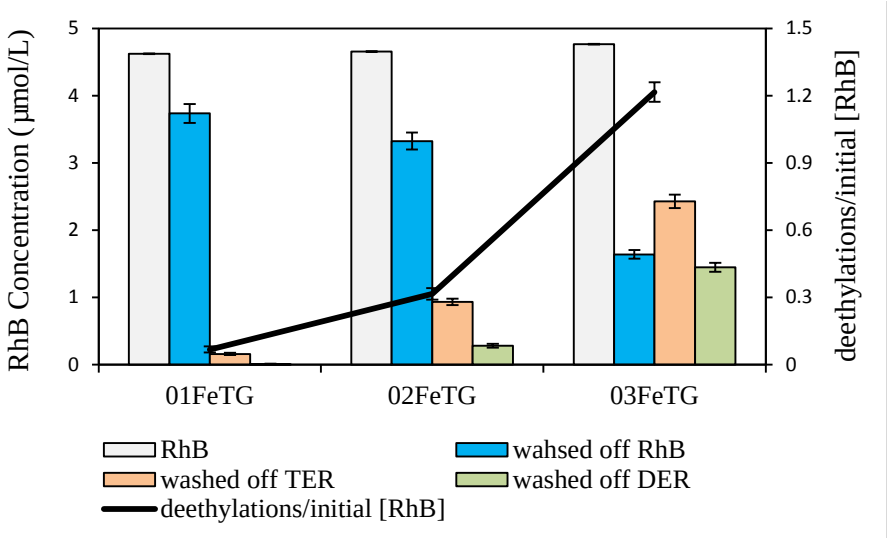

Figure 2-6. Rhodamine speciation (coloured columns) and deethylation ratio (lines) in the solid phase when ~5 μmol/L RhB (light grey columns) was treated with 1.25 g/L FeTGs and 100 μmol/L H_2O_2. H_2O_2 were added after 10-min adsorption by FeTG when little RhB can be detected.

2.3.3.3 Effects of H_2O_2 Dosage

H_2O_2 dosage is an important determinant of extent of RhB removal since it directly affects high-valent-iron species' formation. Within the 30-min reaction time (Figure 2-7a), higher H_2O_2 dosage always resulted in higher extent of RhB removal and deethylation ratios. To slightly change the method of introducing 200 μM H_2O_2, another spike of 100 μM H_2O_2 was added at 30 min in the 100 μM-H_2O_2 batch (Figure 2-7b).

With rapid degradation obtained at the second H_2O_2 spike, a better RhB removal performance was obtained with less than 0.05 μM RhB remaining at 60 min. Further more, the deethylation ratio increased even faster after the second addition of H_2O_2, indicating an efficient further degradation of the de-ethylated rhodamine species. In short, although employing a higher H_2O_2 dosage can lead to a better RhB removal performance in the presence of FeTG, a better approach is to split the high dosage into parts and add sequentially. This also provides confirmation for our previous speculation that a different way of introducing H_2O_2 could further improve the catalytic performance of FeTGs.

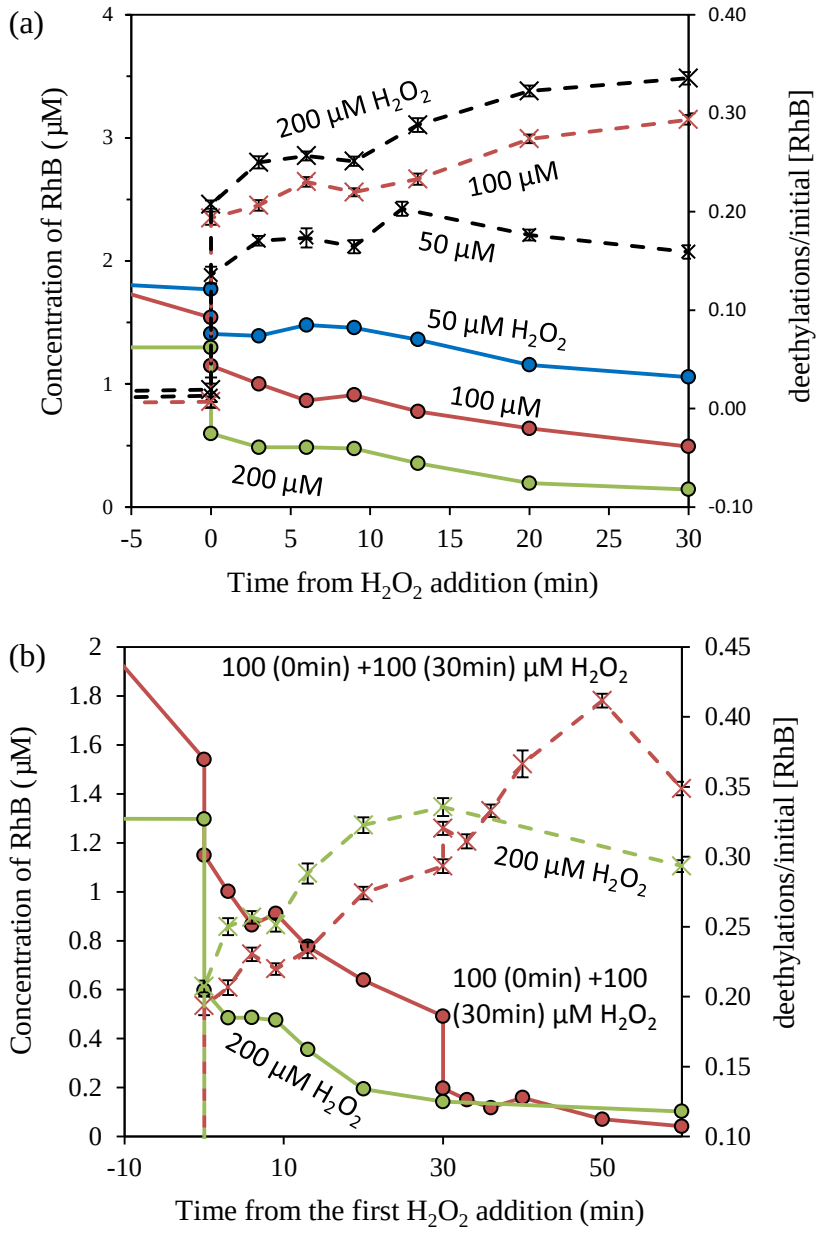

Figure 2-7. RhB concentration variation with time (solid lines) and the deethylation ratio of initial [RhB] (dash lines) when different H_2O_2-addition strategies are applied for 10 μmol/L RhB removal by 1.25 g/L FeTG (Fe-TAML, μmol/g) and different concentration of H_2O_2.

2.3.3.4 Effects of Initial RhB Concentration

Three different initial RhB concentrations (10, 15 and 20 μmol/L) were employed for RhB removal by H_2O_2 activated 01 FeTG and 03 FeTG (Figure 2-8). The reduction percentage does not show obvious dependence on the concentration of RhB, as long as

the same FeTG is used. Up to 20 μmol/L of RhB can still be removed efficiently when catalysed by FeTGs providing an appropriate process is used. The deethylation ratio of RhB in liquid phase after adsorption showed similar variation with time regardless of the RhB loading as shown in each group in Figure 2-8 when the same amount of H_2O_2 was added in the presence of the same amount of FeTG. This indicates the pseudo-first order nature of the RhB degradation process in the liquid phase, where the rate constant depended on the generation of Fe^{IV} species:

$$\frac{d[RhB]}{[RhB]dt} = -k_a[Fe^{IV}]$$

It can be concluded that with generation of enough high valence state iron species, RhB can be degraded efficiently regardless of the initial concentration in a reasonable range.

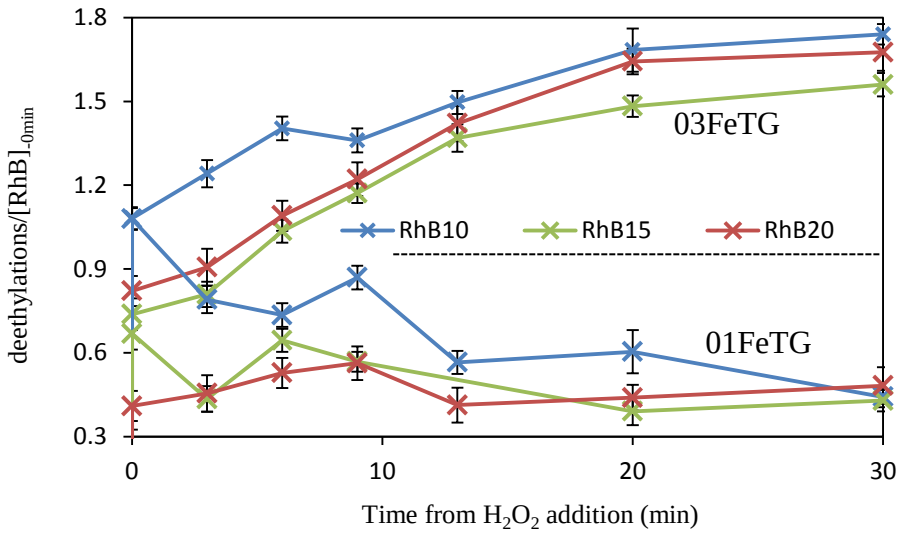

Figure 2-8. Deethylation ratio of dissolved RhB in liquid phase by H_2O_2-activated FeTGs (1.25 g/L) with different Fe-TAML loadings after 30-min adsorption. H_2O_2 dosage: 100 μmol/L.

2.3.4 RhB degradation by electro-activated Fe-TAML/Graphite system

Cyclic voltametric analysis of dissolved Fe-TAML did not show apparent peaks at our experimental condition (details in Appendix 1) with this result consistent with other

published work (Popescu et al., 2010, Demeter et al., 2014). As such, in published studies, Fe-TAML is usually attached to the working electrode. In terms of Fe-TAML/graphite materials, graphite particles could facilitate electron transfer. When using carbon felt as working electrode, it can trap some graphite particles as a result of its adsorption ability and thus pass on electrons directly to Fe-TAML molecules. Regarding CV studies where glassy carbon electrodes are used, Fe-TAML/graphite is typically coated on the surface of the electrodes in order to obtain proper voltammograms.

2.3.4.1 Cyclic voltammetry of Fe-TAML/Graphite

Compared to blank graphite modified glassy carbon (GC) (dashed line in Figure 2-9a), CVs of FeTG modified GC obtained at different scan rates (υ) exhibit two pairs of redox peaks that can be assigned to Fe-TAML (solid lines in Figure 2-9a). This is consistent with a previously published differential pulse voltammogram obtained for the same type of Fe-TAML on GC under basic conditions (Popescu et al., 2010) but the second peak could not be properly assigned at that time. Another CV study of Fe-TAML on GC in 0.1 M HNO_3 gives one redox couple with the anodic peak (0.93 V *vs.* NHE) very close to our anodic peak **2** (1.0 V *vs.* NHE when υ = 100 mV/s) but the cathodic peak (0.61 V *vs.* NHE) close to our cathodic peak **1** (~0.6 V *vs.* NHE when υ = 100 mV/s). This particular redox couple was assigned previously to $Fe^{III}/Fe^{IV}Fe^{IV}$ (Demeter et al., 2014) but the CV spectrum reported by those investigators was quite noisy compared to that presented here. Recently, a study published by Collins' group revealed the existence of a $Fe^{III}Fe^{IV}$ dimer in aqueous solution (Tang et al., 2015) with the existence of this species providing a reasonable explanation of the two redox couples.

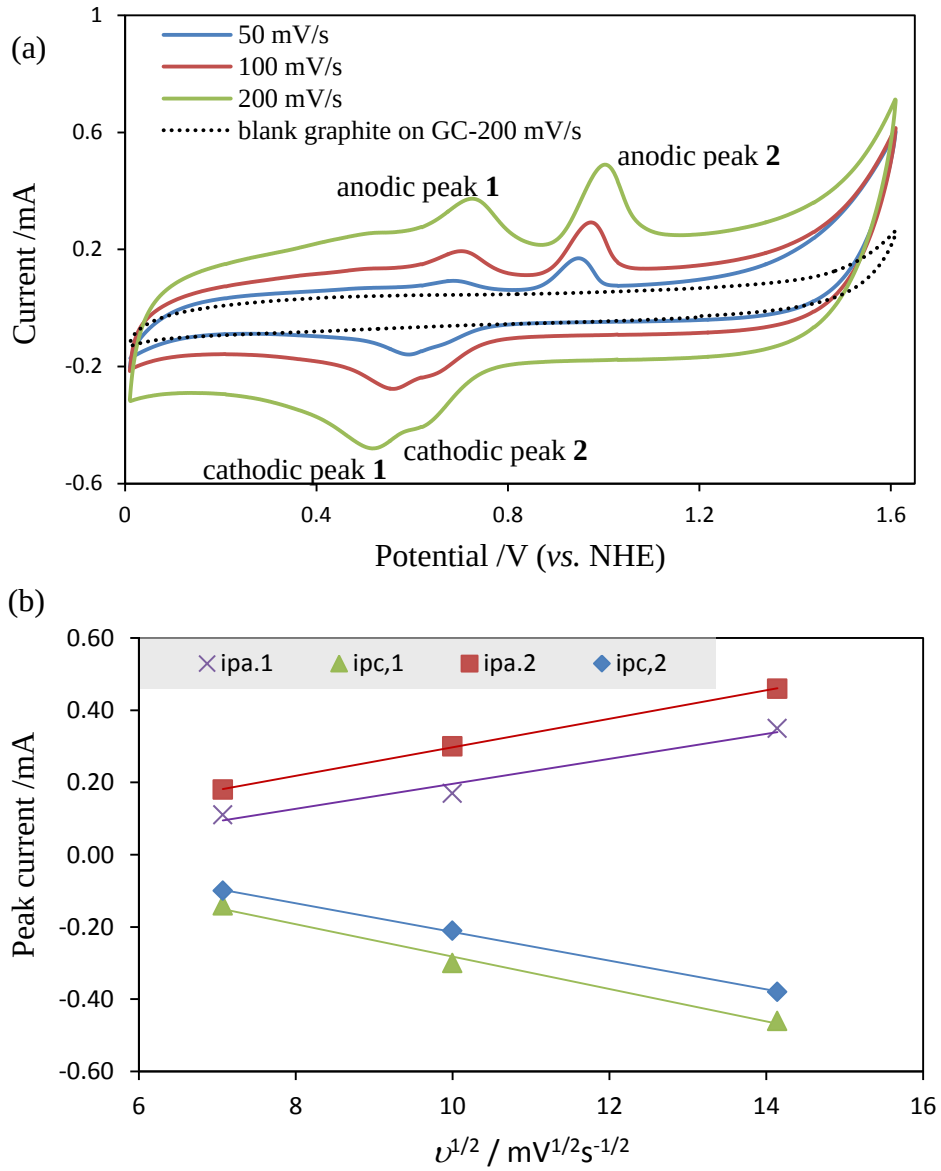

Figure 2-9. (a) CVs of Fe-TAML/Graphite (with Fe-TAML loading of 3.3 μmol/g) and blank graphite modified glass carbon(GC) electrode at different scan rates (υ) in 0.1 M $NaClO_4$ without pH control. (b) Plot of peak currents from (a) as a function of the square root of υ parameters refer to Table 2-1.

Table 2-1 Parameters of the linear fitting of peak currents vs. the square root of scan rate (i_{peak} = a + b $\upsilon^{1/2}$) as shown in Figure 2-9b

	a /10^{-5} A		**b /10^{-5} A $s^{1/2}$ $mV^{-1/2}$**		**R^2**
	Value	S.E.	Value	S.E.	
i_{pa}.2	-9.8	0.7	3.95	0.07	0.9997
i_{pc}.2	20	1	−4.0	0.1	0.9994
i_{pa}.1	−10	7	3.5	0.6	0.9671
i_{pc},1	20	5	−4.5	0.4	0.9903

Based on the speciation of Fe-TAML in aqueous solution (Collins and Ryabov, 2017), the first redox coupe (ΔEp1 = 0.1 V when υ = 50 mV/s) can be assigned to $Fe^{III}OH_2/Fe^{III}Fe^{IV}$ and the second redox couple (ΔEp2 = 0.3 V when υ = 50 mV/s) to $Fe^{III}Fe^{IV}/Fe^{IV}Fe^{IV}$. Since Fe^{V} species are not easily formed (Mills et al., 2015), it is reasonable that these peaks are not observed under our experimental conditions (room temperature, neural pH and potentials not higher than water oxidation). For the $Fe^{III}Fe^{IV}/Fe^{IV}Fe^{IV}$ couple, the anodic peak current is larger than the cathodic current ($i_{pa,2}/i_{pc,2} > 1$), suggesting decay of the $Fe^{IV}Fe^{IV}$ species. In comparison, the cathodic peak current is larger than the anodic current ($i_{pc,1}/i_{pa,1} > 1$) for the $Fe^{III}OH_2/Fe^{III}Fe^{IV}$ couple, with this result supporting the conclusion that the generation of $Fe^{III}Fe^{IV}$ species is due to $Fe^{IV}Fe^{IV}$ decay. Also, the four peak currents are all proportional to the square root of υ (Figure 2-9b, Table 2-1), suggesting a fast electron transfer and diffusion controlled process. This is quite common for heterogeneous catalysts, because electron transfer is usually facilitated by the solid support, in this case graphite.

2.3.4.2 RhB degradation

The FeTG used for the electrochemical studies described here has an Fe-TAML loading of 3.3 μmol/g and is denoted as 04 FeTG here after. RhB speciation in the liquid phase and solid phase were both monitored.

In the liquid phase (Figure 2-10a), 10 μM RhB can be efficiently removed from the liquid phase by electro-activated FeTG at 950 mV (*vs* NHE) with only 0.3 μM RhB remaining (i.e., 97% removal) and no other rhodamine species detected. However, without Fe-TAML, suspended graphite can also improve RhB removal in liquid phase from around 30% (measured in clear solution with blank carbon felt electrodes) up to 90%. Both degradation and adsorption may be involved in RhB removal with speciation in the solid phase needed to be taken into account in order to determine the precise mechanism of RhB removal in these cases.

In order to examine solid phase rhodamine speciation, both carbon felt electrodes and graphite were washed using methanol and the methanol subsequently analysed for rhodamine species. The amount of rhodamine can be washed off by methanol was

corrected by particular recovery factors that accounted for incomplete desorption measured in the RhB adsorption-desorption experiment (details in Appendix 2), which is 83±1% for carbon felt, 72±2% for graphite particles, and 93±5% for the FeTG (with an Fe-TAML loading of 3.3 µmol/g).

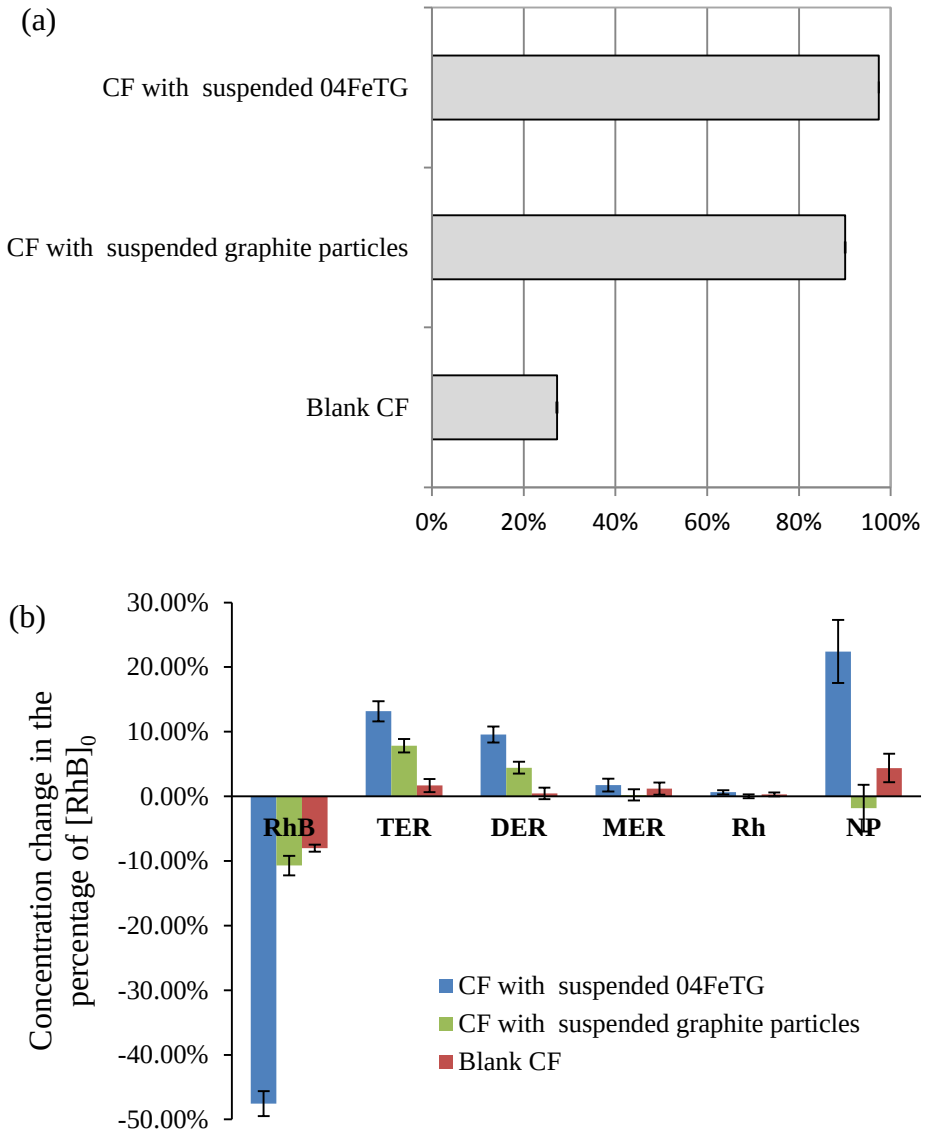

Figure 2-10. (a) RhB reduction in the liquid phase and (b) summary of speciation including washed-off species after electrolysis at 950 mV (vs. NHE) using carbon felt (CF) electrodes in the presence of different suspensions (NP represents non-chromophoric products).

The actual performance was measured by summing up the concentration of species in both liquid and solid phases and dividing by the initial RhB loading (see results in Figure 2-10b). Fe-TAML is actually making a significant difference in terms of degradation. With blank carbon felt electrodes, only about 8% of the RhB was degraded at the anode, mostly to non-chromophoric products, leaving about 20% of the initial RhB adsorbed in the electrodes (mainly in the cathode). Adding graphite particles can only push this to ~10% degradation with this change of minimal significance because the de-ethylated rhodamine species are actually protected by graphite particles enabling RhB to escape further degradation, leaving up to 80% RhB and 10% TER and DER remaining in the solid phase and the other 10% RhB remaining in the liquid phase. Fe-TAML, however, converts the protection to attack and gives a roughly overall 47% RhB degradation which end up at ~22% to non-chromophoric products, ~13% TER, ~10% DER and ~2% MER detected in the solid phase. In short, being activated at 950 mV vs. NHE, Fe-TAML/graphite effectively degrades RhB through an Fe^{IV} species compared to sole electrolysis of RhB which results in 50:50 deethylation and decolorization.

According to the CV results, $Fe^{III}Fe^{IV}$ may not have been fully oxidized to $Fe^{IV}Fe^{IV}$ at 950 mV vs. NHE since this conversion peaks at ~1000 mV. Increasing the potential by 100 mV can increase the degradation up to 75% with this degradation occurring mainly by decolorization (Figure 2-11). This result indicates that the 25% remaining RhB (that is present mainly in the solid phase) is probably unreachable by Fe^{IV} species due to the strong adsorption by uncovered graphite and the cathode. This can be further improved by using FeTG with higher Fe-TAML loading and employing a non-adsorbent cathode. Nevertheless, 1050 mV (*vs.* NHE) activated FeTG leaves a clear solution with no rhodamine species detected.

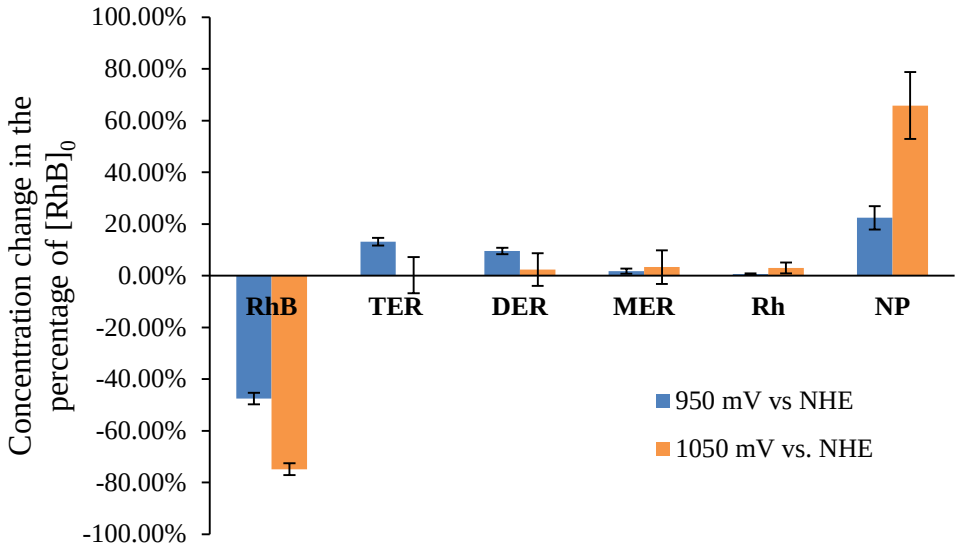

Figure 2-11. Summary of speciation including washed-off species after electrolysis at different potential (vs. NHE) using carbon felt (CF) electrodes with the presence of FeTG/graphite suspension. (NP represents non-chromophoric products)

2.4 Conclusion

Both H_2O_2 and a potential of >950 mV vs NHE can activate graphite supported Fe-TAML to an Fe^{IV} species with this high valent species further oxidizing RhB.

In the presence of H_2O_2, FeTG can efficiently remove RhB to undetectable levels at pH 9, though the average efficiency is a little lower than the equivalent concentration of dissolved Fe-TAML because the low mobility and limited accessibility of the attached Fe-TAML. Graphite as a heterogeneous support can not only enable Fe-TAML recycling but also protect activated Fe-TAML species from fast inactivation. Further, binding of RhB to the graphite resulted in high localised concentrations of RhB and thus an immediate "burst" of degradation with the extent of this "burst" however, expected to vary with hydrophobicity of the contaminant. As rhodamine species on the surface are degraded, the reactions slow down because the migration of rhodamine species is relatively slow compared with the degradation reaction.

When activated electrochemically, Fe^{IV} inactivation is largely reduced (without catalase-like activity) and thus, firstly, results in a more complete degradation despite the fact that there is still some unreachable RhB present in the solid phase and, secondly,

enables RhB degradation at around neutral pH. Moreover, electron transfer is probably enhanced by the presence of graphite particles with this effect enabling the activation of Fe-TAML that was not observed for dissolved Fe-TAML.

In short, graphite support of this biomimetic assemblage is a feasible way to use Fe-TAML with electro-chemical activation of Fe-TAML/graphite better at RhB degradation and more suitable for application in an actual water environment than is the case for H_2O_2 activation.

Chapter 3.
Electrochemically generated iron(IV)-*tpena* as oxidants

Some figures in this chapter have been published in collaboration with Dr. David de Sousa and Prof. Christine McKenzie in Inorg. Chem. 56, 24, 14936-14947.

3.1 Introduction

Direct electrochemical oxidation is a useful tool for biomimetic iron systems (such as Fe-prophrin) as it can both establish the generation of high-valence state iron species and provide basic information on the redox potentials of these species (Groves and Gilbert, 1986, Jeon and Bruice, 1992). For example, by activating homogeneous iron porphyrin at an indium-tin oxide (ITO) electrode, Lei et al. (2004) studied the catalytic mechanism of nitric oxide and nitrite oxidation by Fe^{IV}-porphyrin.

At variance with Fe-TAML, which has been extensively studied since 1998 (Collins and Ryabov, 2017), Fe-*tpena* only appears in papers from 2012 (Lennartson and McKenzie, 2012, Vad et al., 2012) and its activation to high-valent state in aqueous solution needs to be investigated from scratch. Without introducing chemicals which inevitably complicate the system, electrochemical activation could provide a simple means of activating a Fe-*tpena* solution that subsequently allows explicit kinetic analysis including background decay of the activated Fe-*tpena* and its activity toward certain chemicals. Homogeneous electrochemical activation may also be beneficial with regard to practical application provided due consideration is given to choice of electrodes and, ideally, retention of the Fe-tpena complex in the reaction vessel, possibly by attachment to the electrode.

Carbon materials are widely used as electrodes for environmental applications because of their stability, electrical conductivity and cost efficiency with graphite, carbon felt and carbon paper particularly popular. Among these materials, carbon felt stands out as it is light-weight, easy to be modified for application purposes (Huong Le et al., 2017) and has high specific surface area (Minke et al., 2017). For activating Fe-*tpena*, it is also well suited to trapping these molecules and thus facilitating direct electron transfer.

In this chapter, Fe-*tpena* will be activated electrochemically at a carbon felt electrode. By monitoring the decay of Fe^{IV}-*tpena*, the second-order rate constants for its reaction with selected target species will be extracted. Particular attention in this work will be given to the oxidative degradation of the two chemicals formate and Rhodamine B. Formate is considered an ideal probe for use in the Fe-*tpena* systems both i) because its oxidation pathway is simple and should provide information on the nature of the active oxidants and ii) because its C-H bonds are strong (with the bond dissociation energy $\geq$ 96 $\pm$ 1 kcal mol^{-1} (Blanksby and Ellison, 2003)) and if they can be broken in this compound then the Fe-tpena system is likely to be effective in degrading other compounds with weaker or similar C-H bonds.

3.2 Materials and methods

3.2.1 Reagents and materials

Fe-*tpena* was provided by Prof. C.J. McKenzie and her group from the University of Southern Denmark and was prepared as described by Lennartson and McKenzie (2012). All commercially available reagents were used without further purification. All solutions were prepared in 18 MΩ cm Milli-Q water obtained from a Millipore Milli-Q system. Electrode preparation was as described in Chapter 2.

3.2.2 Electro-activation of Fe-*tpena*

Fe-*tpena* activation was performed by bulk (potentiostatic) electrolysis of aqueous solutions of 0.1 M $NaClO_4$ containing dissolved Fe^{III}-*tpena* (0.8 mM per Fe, native pH ~3.6) using a CH Instruments 650D electrochemical work station with stirring

throughout the electrolysis process. A graphite felt working electrode (1.5 × 1.5 × 0.4 cm^3 unless specified) pierced with a titanium wire as the connector was used. A platinum coil electrode (custom made) was used as the counter electrode. The counter electrode was housed in a separate fritted glass chamber filled with ~400 μL of electrolyte (to the level of the bulk electrolyte surface) and submerged in the bulk electrolysis cell. The reference electrode for all electrolysis experiments was a micro Ag/AgCl electrode (3 M KCl). All potentials have been given versus the normal hydrogen electrode (NHE) as described in 2.2.5.

3.2.3 Kinetic analysis

Fe-*tpena* in either unbuffered (0.1 M $NaClO_4$, native pH ~3) or in pH 4 buffered electrolyte (0.05 M acetate and 0.1 M $NaClO_4$) was electrolyzed at a constant potential (1.42 V vs NHE) using the setup described above for 30−40 mins. The resulting pale-green solutions were immediately filtered and 3.00 mL transferred to a cuvette where reaction with selected target species were initiated (This step needs to be done as quickly as possible so Fe^{IV}-*tpena* decay would be minimal before any substrate addition). The kinetics of the subsequent reaction was determined by monitoring the loss of Fe^{IV}-*tpena* at its near-IR absorbance peak at 730 nm.

For examination of water-oxidation at different pHs, unbuffered media were used with the pH adjusted manually with dilute NaOH/$HClO_4$ prior to starting the UV-vis measurements.The pH adjustment process needs to be undertaken as quickly as possible to minimize Fe^{IV}-*tpena* decay, so any pH obtained was recorded immediately before the UV-vis scans. Such experiments were performed ~30 times to cover most pHs of interest.

For the oxidation of particular organic compounds, the UV-vis spectrum was first monitored for 120−200 s to determine the background decay rate, after which an aliquot of substrate (3−400 equiv) from a concentrated aqueous stock solution was added and the reaction rate measured. The background decay rate (k_{decay}) and the substrate reaction rate (k_{obs}) were determined by a least-squares fitting of the absorbance at 730 nm to an expression appropriate for (pseudo)-first-order exponential decay; i.e.

$Abs_t = Abs_f + (Abs_0 - Abs_f) \exp(-k_{ob}st)$

Second-order rate constants (k_2) were extracted from linear regressions of plots of $k_{obs}' = k_{obs} - k_{decay}$ against the substrate concentrations. The pH-dependent formate/formic acid reactivity studies was carried out in unbuffered media where both the formate/fomic stock solution and Fe^{IV}-*tpena* solution were adjusted to the desired pH before starting the UV-vis measurements. The degradation of rhodamine B by Fe^{IV}-*tpena* was monitored by the same technique as described in Chapter 1 with pH effects considered.

3.2.4 Formate degradation monitoring

Formate degradation was examined by monitoring the loss of radiolabelled target species. Specifically, ^{14}C-labeled sodium formate was spiked at 40 nM to experimental solutions with the remaining desired formate concentration made up with unlabeled sodium formate. Experiments were performed in an enclosed apparatus with the exhaust gas passing through a 1 M NaOH trap (details below) to recover $^{14}CO_2$ as $Na_2{}^{14}CO_3$. The concentrations of $Na_2{}^{14}CO_3$ and ^{14}C-formate remaining in the reactor (measured after $^{14}CO_2$ had been liberated from acidified samples by aeration) were determined by scintillation counting using an Ultima Gold scintillation cocktail (PerkinElmer) and a PerkinElmer Tri-Carb 2910TR liquid scintillation analyzer.

NaOH trap solution preparation

A NaOH trap solution was prepared using the oil-lye method (Allen and Low, 1933) to minimize the presence of carbonate. The oil-lye solution was prepared by dissolving 10.0 g NaOH in 10.0 mL of CO_2-free mQ water in a vessel immersed in an ice-water slurry which was then dispersed thoroughly by heating over a water bath and shaking until no more solid dissolves. After cooling to room temperature, clear supernatant (~19 M NaOH) obtained by centrifuging was decanted in to a HDPE storage container and diluted to 1 M NaOH to be used as the trap solution with this solution expected to contain ~0.1% carbonate (molar basis relative to hydroxide) (Han and Chao, 1932).

3.3 Results and discussion

3.3.1 Electrochemical activation of Fe-*tpena*

Fe^{IV}-*tpena* generation is evident from the presence of a peak at 730 nm (Vad et al., 2012) when an unbuffered Fe-*tpena* solution (native pH ~3.5) in an appropriate electrolyte (0.1 M $NaClO_4$) is electrolysed at a potential higher than 1.3 V vs NHE (see Figure 3-1). A colour change from brownish yellow to pale bluish green and gas evolution on the cathode (platinum wire) can be observed during this process. Fe^{IV}-*tpena* yield tends to be higher with larger working electrode as shown in the insert in Figure 3-1 though it can vary from time to time (as electrode condition changes).

The gas generated from the cathode should be hydrogen as a result of the following reaction at the cathode:

$$2H^+ + 2e^- = H_2.$$

Despite the H^+ consumption at the cathode, however, a pH drop from ~3.5 to ~2.8 is observed on electrolysis in the main anodic compartment. This is likely partly attributable to some diffusion of H^+ across the glass frit from the cathodic to the anodic chamber, as well as to H^+ generation at the anode during the Fe-*tpena* oxidation, as the dominant protonation state changes during oxidation; i.e.

$$[Fe^{III}(OH)(tpenaH)]^{2+} - e^- = [Fe^{IV}(O)(tpenaH)]^{2+} + H^+ \quad (eq.3\text{-}1)$$

The detailed Pourbaix diagram of the Fe-*tpena* system (Figure 3-2) was determined in collaboration with Prof. McKenzie's group at Southern Denmark University as described in *Inorg. Chem. 56, 24, 14936-14947*.

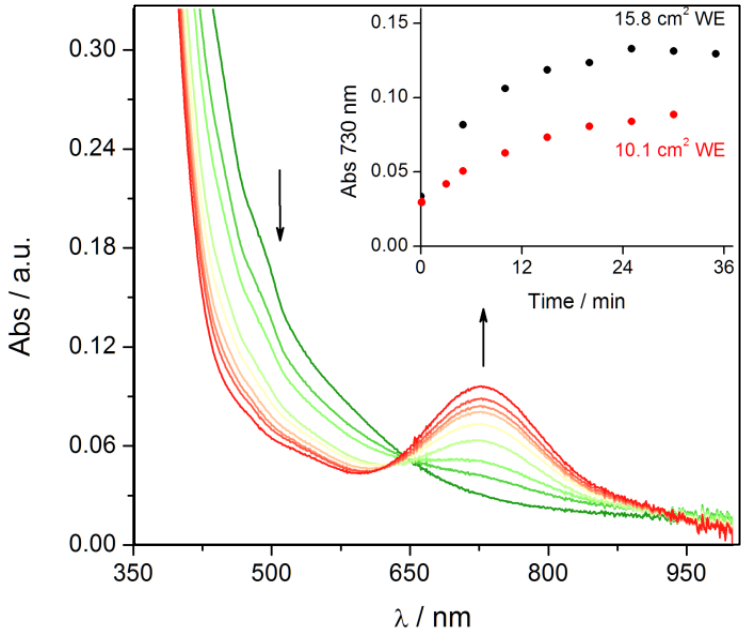

Figure 3-1. UV-Vis spectra of 0.8 mM (per Fe) Fe-*tpena* in 0.1 M $NaClO_4$ when electrolyzed at 1.42 V over a 10.1 cm^2 or 15.8 cm^2 carbon felt working electrode (WE). Spectra recorded every ~5 min. Insert: Time-traces for λ = 730 nm, showing the effect of the working electrode's size.

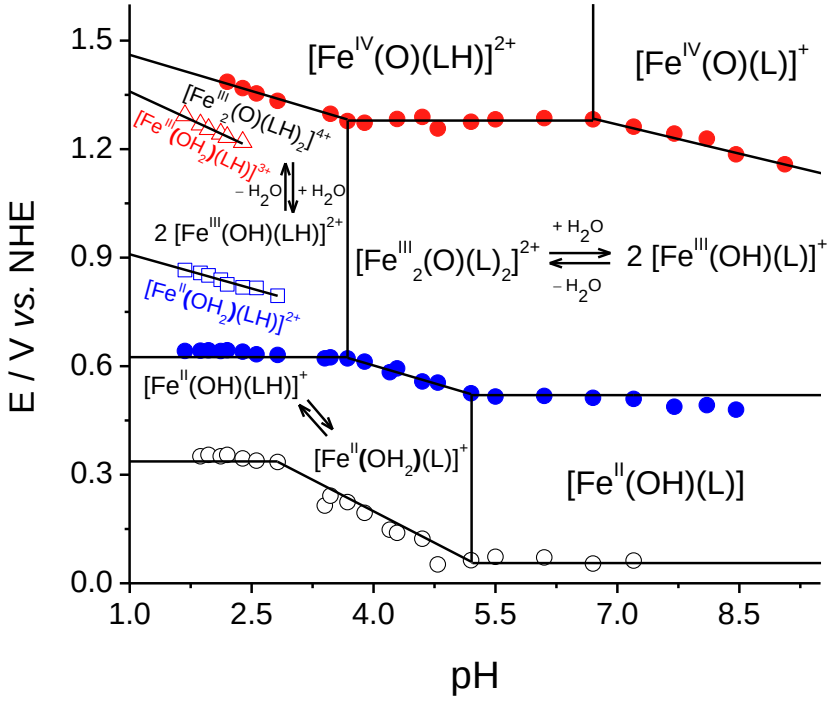

Figure 3-2 Pourbaix (potential–pH) diagram for the $Fe^{II/III/IV}$-*tpena* system (L = *tpena*).(de Sousa et al., 2017)

The presence of observable Fe^{IV} concentrations in acidic aqueous solution demonstrates that Fe^{IV}-*tpena* is relatively stable with respect to reduction by water and, as such, could be well suited to oxidation of selected contaminants. The optimal pH range for generation and application of Fe^{IV}-*tpen*a is further investigated in the following section.

3.3.2 Decay of Fe^{IV}-*tpena* in water at different pHs

As shown in Figure 3-3a, decay of Fe^{IV}-*tpena* following the cessation of electrolysis may continue for some hours. To study the decay of Fe^{IV}-*tpena* in substrate-free water, NaOH/$HClO_4$ solution was used to adjust the pH to the desired value as soon as electrolysis had stopped with the observed rate constants for Fe^{IV}-*tpena* absorbance decay plotted in Figure 3-3b (grey points). These results show that the pH affects Fe^{IV} species' longevity significantly with its half life dropping from 30 min (at pH 3-4) to 5 min (at pH 6-7) and even more significant decreases at pH > 7. This pH dependence in reactivity cannot be explained by the acid-base reactions of Fe^{IV}-*tpena* if only water oxidation is considered as shown by the dashed line (k'_{H_2O}) which deviates significantly from the actual k_{obs} when pH > 7. In this case, including the oxidation of hydroxide (OH^-) (dotted straight line) seems to provide a good fit for the overall k_{obs} in water (noted as k_{decay} hereafter, as studies with other substrates is always carried out in aqueous conditions) as shown by the solid curve associated with the following expression:

$$k_{decay} = k'_{H_2O} + k'_{OH^-} = (k_{HA}[H_2O]\,\alpha_{HA} + k_{A^-}[H_2O]\,\alpha_{A^-}) + k_{OH^-}[OH^-]$$

where,

$\alpha_{HA} = \frac{10^{-pH}}{10^{-pH} + 10^{-pk_a}}$, p$K_a$=6.7;

$\alpha_{A^-} = 1 - \alpha_{HA}$;

$[OH^-] = 10^{pH-14}$;

k_{HA} is the second-order rate constant for water oxidation by the Fe^{IV}-*tpena* acid congener ($[Fe^{IV}(O)(tpenaH)]^{2+}$) and k_{A^-} is the second-order rate constant for water oxidation by the Fe^{IV}-*tpena* base congener ($[Fe^{IV}(O)(tpena)]^{+}$).

This is further confirmed by fitting formate oxidation data at high pH as the observed decrease of the Fe^{IV} absorbance (k_{obs}) is as a result of the self-decay rate (k_{decay})

expected at that pH plus the expected formate oxidation rate ($k_{HCOO^-}[HCOO^-]$) as shown in Figure 3-3 (detailed formate oxidation study can be found in 3.3.3).

Based on these findings, the background decay of Fe^{IV}-*tpena* in aqueous solutions can be determined at any particular pH using best-fit values for k_{HA} and k_{OH^-} of 4×10^{-4} and 3×10^{2} $M^{-1}s^{-1}$, respectively. It should be noted however that, because of the much more rapid oxidation of OH^- than H_2O under basic conditions and a pK_a of Fe^{IV}-*tpena* that is close to the pH of water, the rate constant for water oxidation by the Fe^{IV}-*tpena* base congener ($[Fe^{IV}(O)(tpena)]^+$) (k_{A^-}) is difficult to assign (the best fit shown in figure 3-3 used a k_{A^-} value of 1.2×10^{-3} $M^{-1}s^{-1}$); for the same reasons, k_{A^-} is not particularly important.

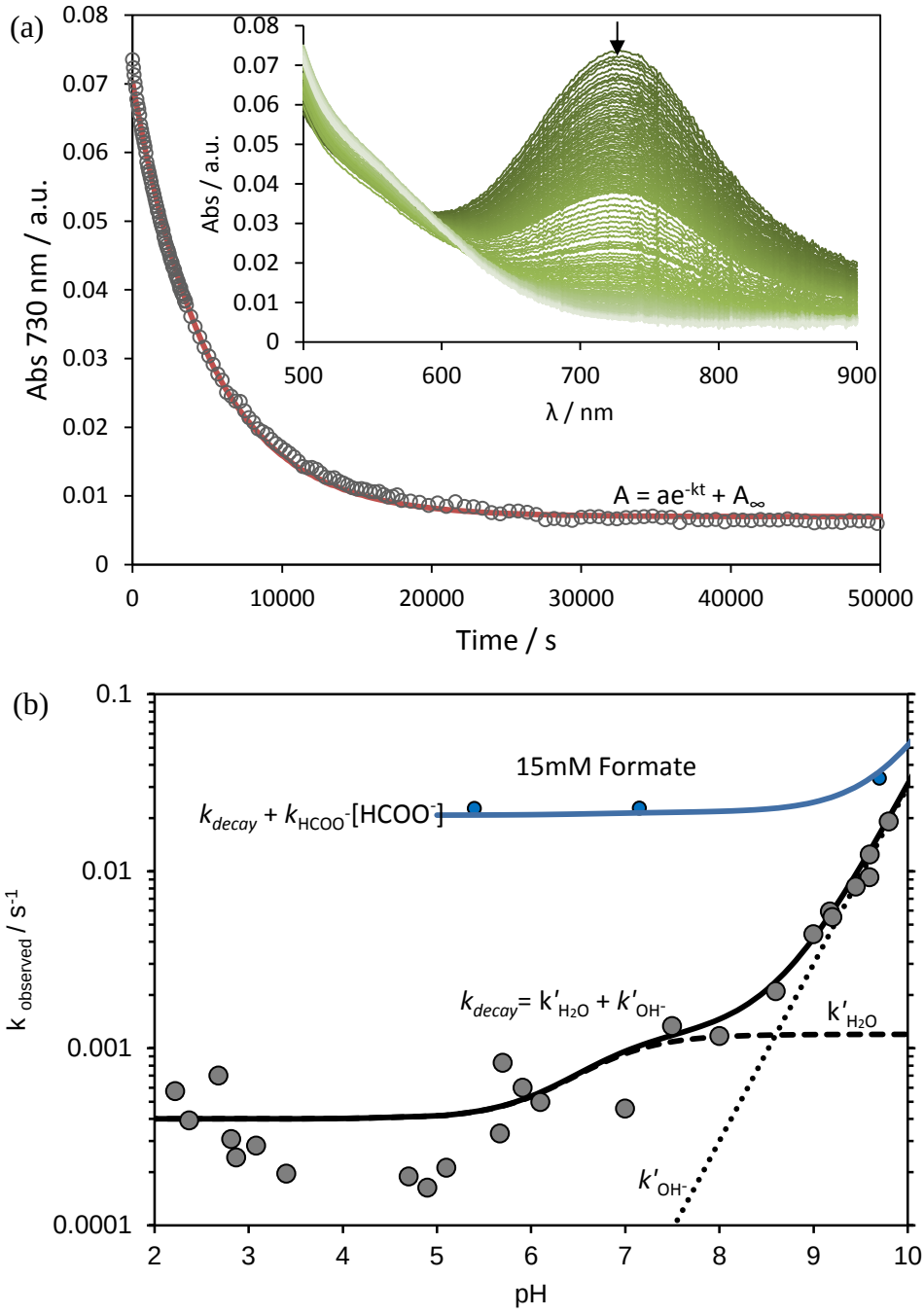

Figure 3-3 (a) Time-traces for λ = 730 nm of 0.8 mM Fe-*tpena* in 0.1 M $NaClO_4$ showing Fe^{IV}-*tpena* decay after 30 min-electrolysis has been stopped and pH has been adjusted to pH 5.1 and its exponential fit (red line) Insert: corresponding UV-Vis spectra. (b) Observed rate constants (k_{obs}) for the oxidation of H_2O and OH^- (grey spots) and formate (blue spots) by Fe^{IV}-*tpena* as a function of pH.

3.3.3 Formate degradation by electrochemically generated Fe^{IV}-*tpena*

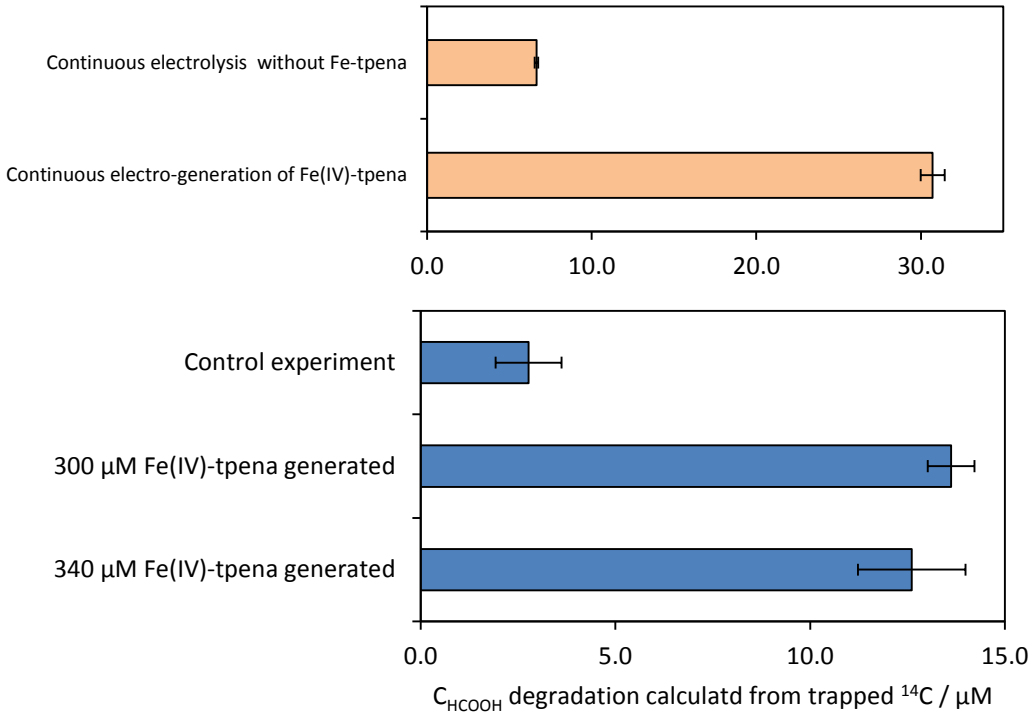

Figure 3-4 Comparison of total formate (C_{HCOOH}) degradation (calculated from 1 M NaOH trapped ^{14}C) with/without electo-generated Fe^{IV}-*tpena*. Initial C_{HCOOH} = 1 mM.

To confirm formate/formic acid oxidation by Fe^{IV}-*tpena*, formate/fomic acid solution containing ^{14}C labelled molecules was added to electro-generated Fe^{IV} solution either with continuous electrolysis or after the electrolysis had ceased (without altering the pH at ~3). ^{14}C associated with CO_2 resulting from the oxidation of formate can be measured by scintillation counting in a NaOH trap solution with an approximately four fold increase in extent of CO_2 generation compared to that observed in control experiments in which Fe-*tpena* was absent (Figure 3-4). This result indicates that generation of most of the $^{14}CO_2$ observed that can be attributed to the oxidation of formate/fomic acid by Fe^{IV}-*tpena*. It should be noted however that the amount of ^{14}C detected in this way is lower than that expected given the measured decrease in ^{14}C in the reactor (data not shown) with the discreapancy possibly due to the presence of a gas leak in the system.

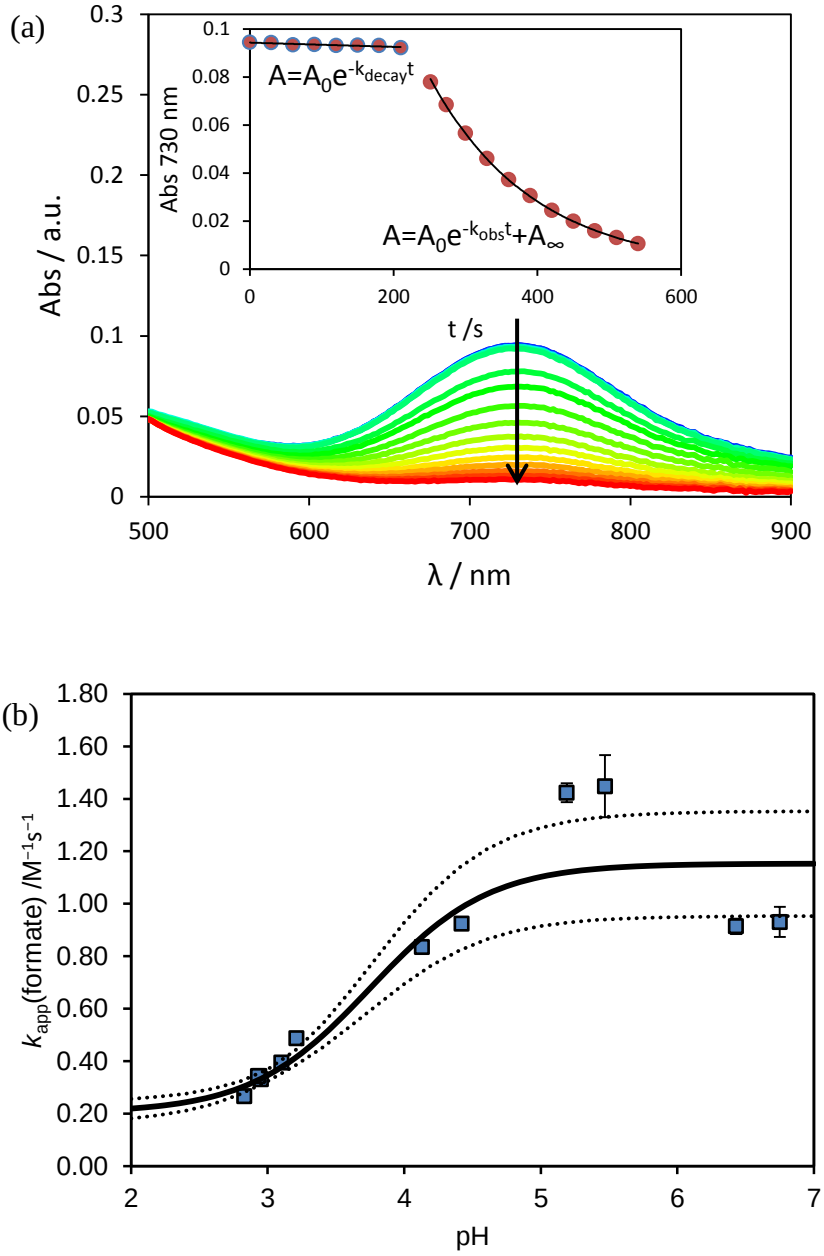

Figure 3-5 (a) UV-Vis spectra of the reaction of Fe^{IV}-*tpena* (0.8 mM per Fe, 0.1 M $NaClO_4$) with formate/formic acid at pH 3 (25 equiv). Insert: Time trace for λ = 730 nm before and after the addition of formate/formic acid solution and exponential fits to extract the observed rate constants. (b) Plot of the apparent rate constants for the pH-dependent formate/formic acid oxidation ($k_{app} = (k_{obs} - k_{decay})/C_{HCOOH}$) with fitted curve for k_{HCOOH} = 0.20 ± 0.02 $M^{-1}s^{-1}$, k_{HCOO^-} = 1.2 ± 0.1 $M^{-1}s^{-1}$, pK_a(HCOOH) = 3.75; dashed line shows 95% confidence interval.

To study the kinetics of formate/fomic acid oxidation by Fe^{IV}-*tpena*, a range of much higher total formate loadings (2~100 equivalents of Fe) was employed to give pseudo-

first order reactions. Fe^{IV}-*tpena* decay was monitored by UV-vis spectra before/after formate addition into an electro-generated Fe^{IV}-*tpena* solution after both were adjusted to the desired pH. As expected, a faster decay of Fe^{IV}-*tpena* can be observed upon introducing formate solution. This allows the extraction of observed rate constants k_{obs} and k_{decay} (an example is shown in Figure 3-5a) at different pHs. The apparent rate constants k_{app} can then be plotted as a function of pH where $k_{app} = (k_{obs} - k_{decay})/C_{HCOOH}$ (C_{HCOOH} is the total concentration of $HCOO^-$ and HCOOH) and thus enables fitting for the second rate constants k_{HCOOH} and k_{HCOO^-} based on:

$$k_{app} = k_{HCOOH}\,\alpha_{HCOOH} + k_{HCOO^-}\,\alpha_{HCOO^-}$$

where,

$\alpha_{HCOOH} = \frac{10^{-pH}}{10^{-pH} + 10^{-pk_a}}$, p$K_a$ = 3.75;

$\alpha_{HCOO^-} = 1 - \alpha_{HCOOH}$.

The best fit values are k_{HCOOH} = 0.20 ± 0.02 $M^{-1}s^{-1}$ and k_{HCOO^-} = 1.2 ± 0.1 $M^{-1}s^{-1}$ as shown in Figure 3-5b. The enhanced activity of Fe^{IV}-*tpena* toward formate anion than neutral formic acid can be attributed to the positive charge of Fe^{IV}-*tpena* and the hydrogen-bonding potential.

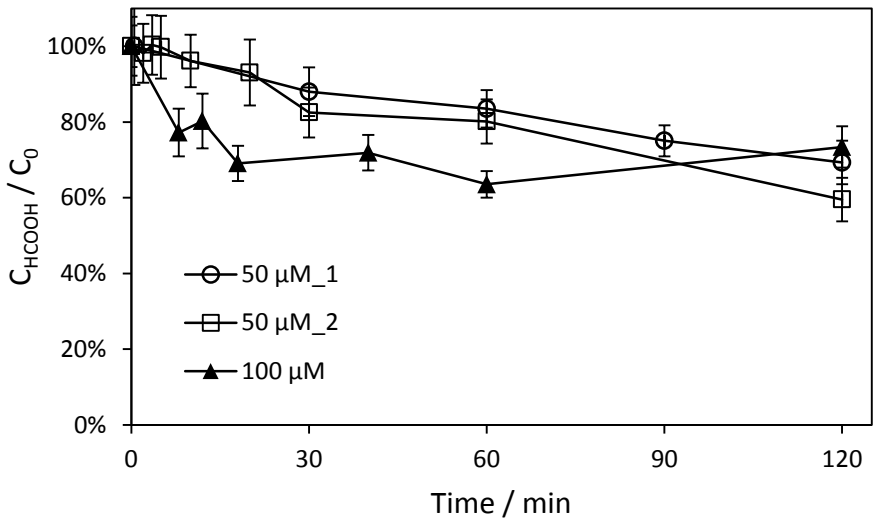

Figure 3-6 Time traces of formate degradation percentage when added to electro-generated Fe^{IV}-*tpena* (0.8 mM per Fe, 0.1 M $NaClO_4$) at pH 5

C_{HCOOH} decrease was also monitored at low C_{HCOOH} loadings (50 and 100 μM) by measuring the decay of ^{14}C-formate in the reactor when formate was added to electro-generated Fe^{IV}-*tpena* solution after both had been adjusted to pH 5. The one-off electro-generated Fe^{IV}-*tpena* solution is hard to control in terms of Fe^{IV} concentration which ranges from 200 to 400 μM. Despite this complication, C_{HCOOH} decrease is always roughly around 30% of that initially present as shown in Figure 3-6. At pH 5, $HCOO^-$ is dominant at ~95%, so Fe^{IV} is mainly consumed by $HCOO^-$ ($k_{HCOOH}\,\alpha_{HCOOH} = 0.01$, $k_{HCOO^-}\,\alpha_{HCOO^-} = 1.14$) and background decay ($k_{decay} \approx 4 \times 10^{-4}$) according to the above kinetic study.

$$\frac{d[\mathrm{Fe^{IV}}]}{dt} = k_{decay} + k_{HCOO^-}[\mathrm{HCOO^-}]$$

3.3.4 RhB degradation by electrochemically generated Fe^{IV}-*tpena*

Fe^{IV}-*tpena*'s activity toward rhodamine B in acidic conditions was also examined by adding different concentrations of RhB into electro-generated Fe^{IV}-*tpena* solution (0.8 mM per Fe, 0.1 M $NaClO_4$, pH ~3). An instant consumption of Fe^{IV} and RhB degradation can be observed from the UV-vis spectra shown in Figure 3-7. Higher initial RhB concentration results in faster Fe^{IV} decay as expected. Since the Fe^{IV} decay rate is complicated by the degradation of other rhodamine species, RhB concentration and its degradation rate need to be considered in order to determine the second-order rate constant for RhB oxidation by Fe^{IV}-*tpena* from $\frac{d[RhB]}{dt} = k[\mathrm{Fe^{IV}}tpena][RhB]$. With these values either given or calculable from Figure 3-7, k_2 for RhB oxidation by Fe^{IV}-*tpena* can be plotted as shown in Figure 3-8 with these results revealing a value for k_2 of 60 ± 24 $M^{-1}s^{-1}$.

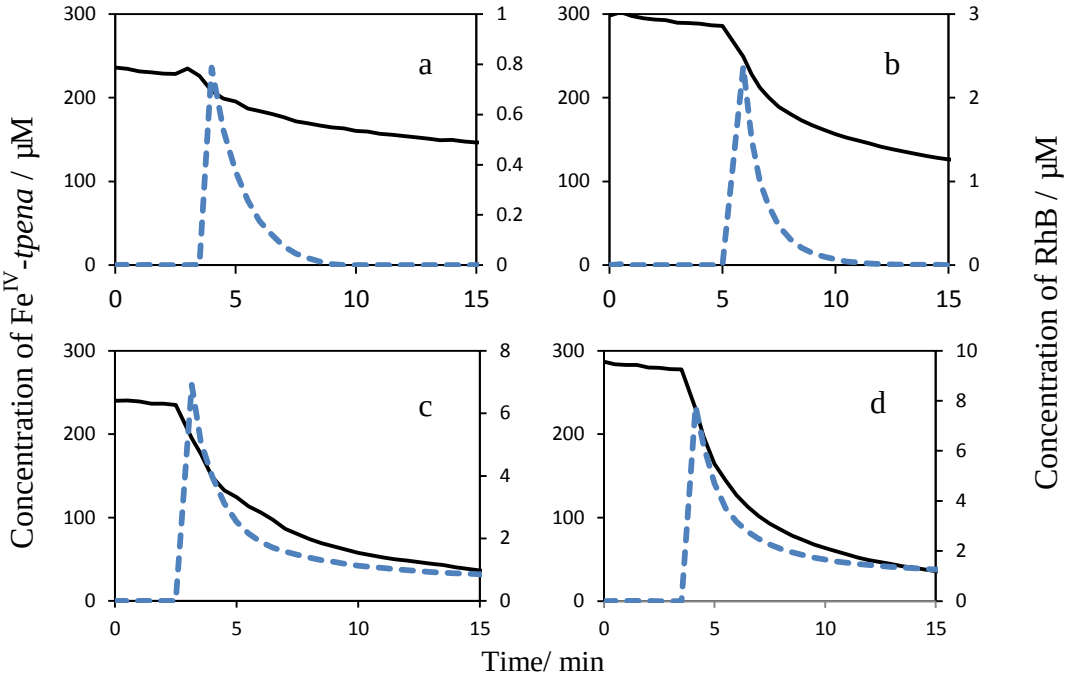

Figure 3-7 Time trace for Fe^{IV}-*tpena* and RhB when different concentrations of RhB (dashed lines) was added to ~250 μM Fe^{IV}*tpena* (solid lines) solution. Initial RhB concentrations are 2 μM (a), 5 μM (b), 8 μM (c) and 10 μM (d).

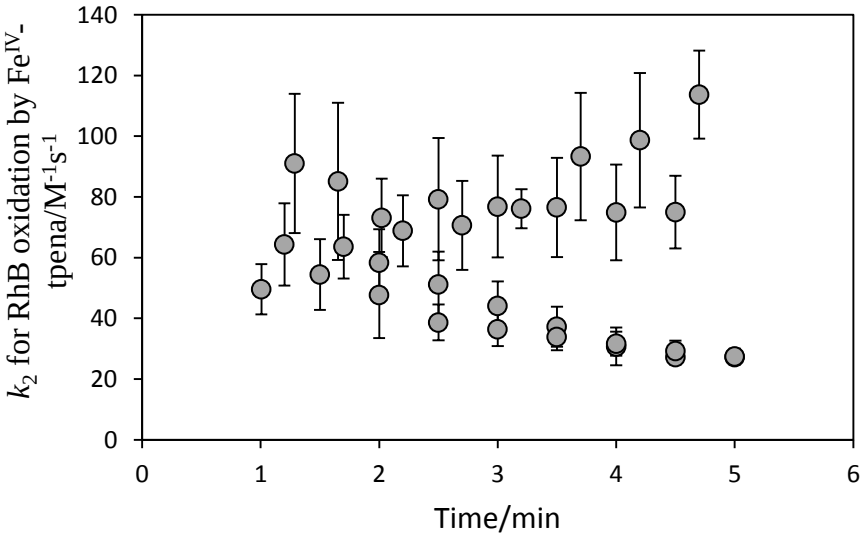

Figure 3-8 Plot of second-order rate constant for RhB oxidation by Fe^{IV}-*tpena* when both RhB and Fe^{IV} concentrations vary significantly with time.

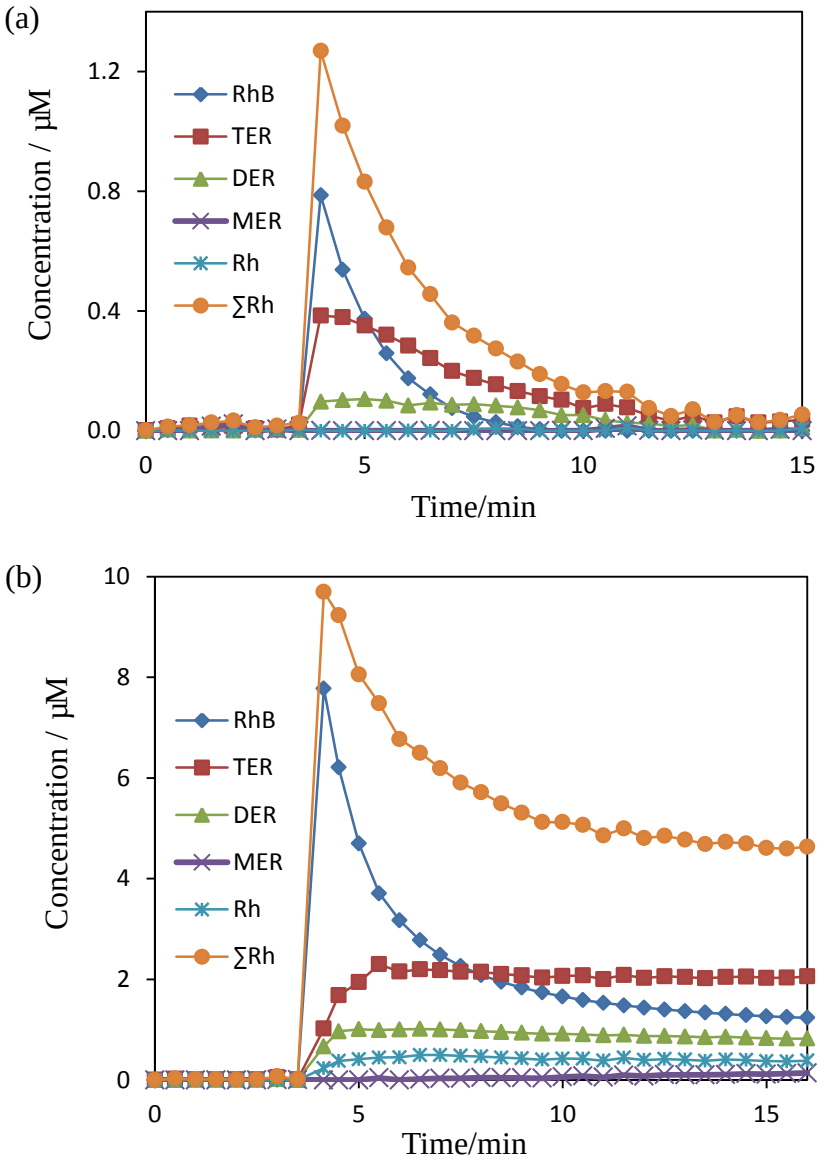

Figure 3-9 Time traces of all the rhodamine species when (a) 2 μM or (b) 10 μM RhB is added to electro-generated Fe^{IV}-*tpena* solution (0.8 mM per Fe, 0.1 M $NaClO_4$, pH ~3)

Figure 3-9 shows detailed rhodamine species' change along with accompanying degradation. Generation and degradation of TER and DER can be observed in the 2-μM-RhB case with eventual complete decolourization without the presence of any detectable rhodamine species. At higher RhB loading (10 μM), Rh is also detectable. The generation and subsequent degradation of these de-ethylated rhodamine species is balanced after 6 minutes with a slow decrease in RhB concentration which also levels off at ~15 minute. For the 10 μM initial RhB case, the total rhodamine species

concentration is on the order of ~4.5 μM with TER dominant at 2 μM and RhB at 1.2 μM.

Overall, RhB degradation by unbuffered one-off Fe^{IV}-*tpena* addition is quite significant with this degradation occurring through a deethylation pathway. It should also be noted that its decolourization is quite impressive compared to that achieved with peroxide-activated-Fe^{IV}-TAML (as described in Chapter Two). Comparison with Fe-TAML under similar conditions should be of interest and will be examined in Chapter Four.

3.3.5 Other substrates oxidation by electrochemically generated Fe^{IV}-*tpena*

Fe^{IV}-*tpena*'s activity toward other substrates including tetrahydrofuran (THF), isopropyl alcohol (*i*-PrOH), ethanol (EtOH), methonal (MeOH), phthalhydrazide (Phth) and Orange II have also been examined under acidic conditions. Following the same procedures as for the kinetic study of formate oxidation described in Section 3.3.2, the observed rate constants k_{obs} and k_{decay} can be extracted for each substrate. The corrected observed rate constants can then be calculated as $k'_{obs} = k_{obs} - k_{decay}$ and are plotted in Figure 3-10. This also allows the extraction of the second-order rate constants from linear fitting since $k'_{obs} = k_2$[substrate] (Table 3-1). All these substrates are degradable by Fe^{IV}-*tpena* with the second-order rate constant roughly correlated with that for $HO^{\bullet}$ oxidation, though with much lower values.

Of the substrates examined, Fe^{IV}-*tpena* shows the highest activity toward Orange II (1.1×10^3 $M^{-1}s^{-1}$) with this value similar to that achieved with Fe^{IV}-TAML considering the pH differential as Chahbane et al. (2007b) reported a value of $(3.8 \pm 0.3) \times 10^4$ $M^{-1}s^{-1}$ for the reaction between Orange II and chemically activated Fe-TAML at pH 9.

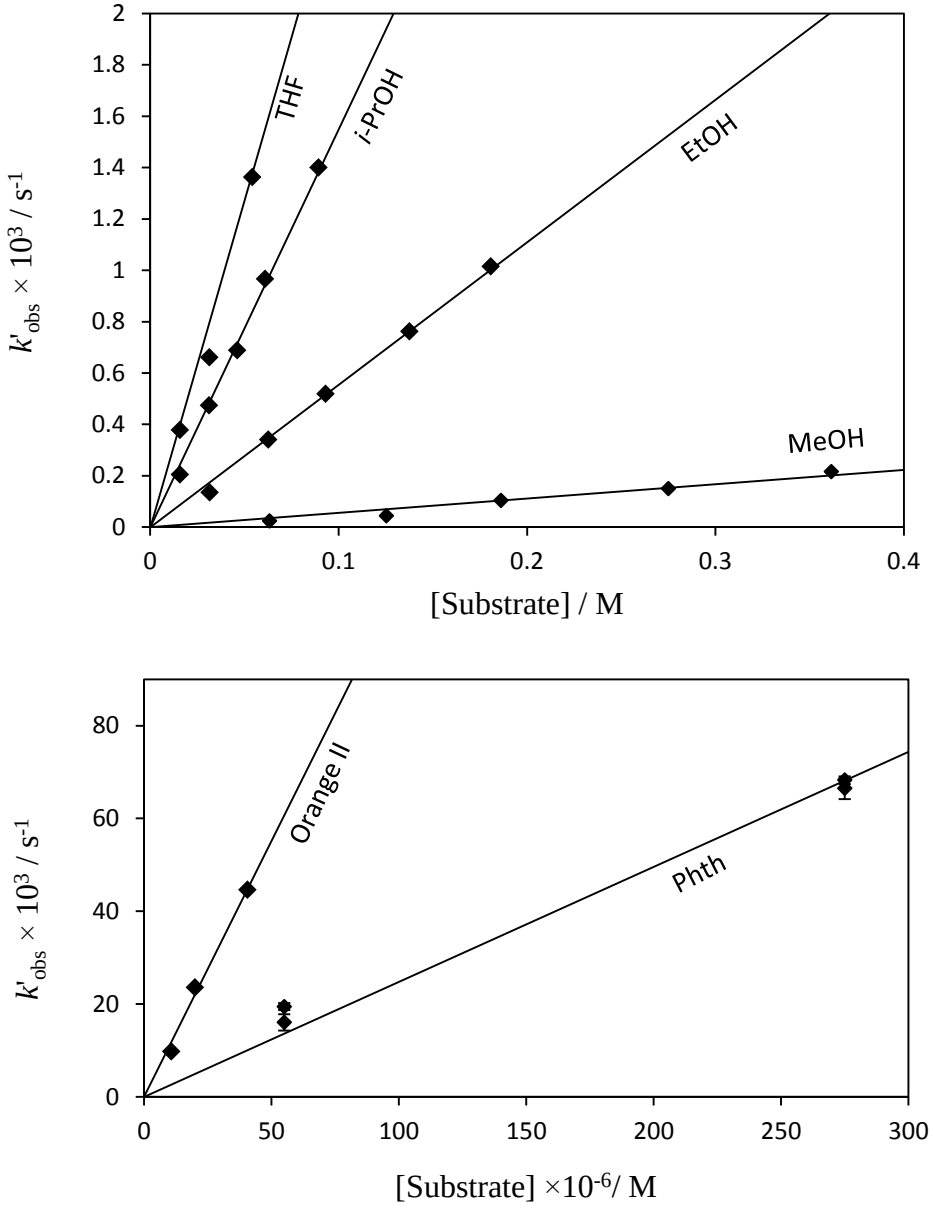

Figure 3-10 Plot of observed rate constants corrected for self-decay ($k'_{obs} = k_{obs} - k_{decay}$) against the substrate concentrations enabling extraction of the second-order rate constants (k_2).

Table 3-1 Second-Order Rate Constants for Substrate Oxidations by Fe^{IV}-*tpena*

CH_3OH	methanol	6.0×10^{-4}	9.7×10^{8} [a]
CH_3CH_2OH	ethanol	5.6×10^{-3}	1.9×10^{9} [a]
$(CH_3)_2CHOH$	isopropyl alcohol	1.6×10^{-2}	1.9×10^{9} [a]
$(CH_2)_4O$	tetrahydrofuran	2.6×10^{-2}	4.0×10^{9} [a]
$C_8H_6N_2O_2$	Phthalhydrazide	2.5×10^{2}	5.3×10^{9} [b]
$C_{16}H_{11}N_2NaO_4S$	Orange II	1.1×10^{3}	6.0×10^{9} [c]

[a] Buxton et al. (1988); [b] Schiller et al. (1999); [c] Kiwi et al. (2000).

3.3.6 Chloride − Fe^{IV}-*tpena* interaction

Adding different amounts of sodium chloride does not obviously affect the Fe^{IV}-*tpena* decay (Figure 3-10). The observed rate constants extracted from the exponential fitting of absorbance change at 730 nm ($Abs_t = Abs_0 e^{-k_{obs}t}$) range from 6×10^{-5} to 1×10^{-4} at all NaCl concentrations used (from 0.25 M to 1.00 M) as shown in Table 3-2. Comparing to the rate constant for Fe^{IV}-*tpena* self decay at ~pH 3 (Figure 3-3) of $1\sim4\times10^{-4}$ s^{-1}, Cl^- does not accelerate Fe^{IV}-*tpena* decay. On the other hand, high ionic strength of 0.50 M^+ actually slows down Fe^{IV}-*tpena* decay because of its decreased ion activity. As a result, Cl^- levels of lower than 0.25 M would not be expected to significantly affect Fe^{IV}-*tpena* behaviour. As such, NaCl will be used as background electrolyte in further study of Fe-*tpena* system in order to maintain a constant ionic strength.

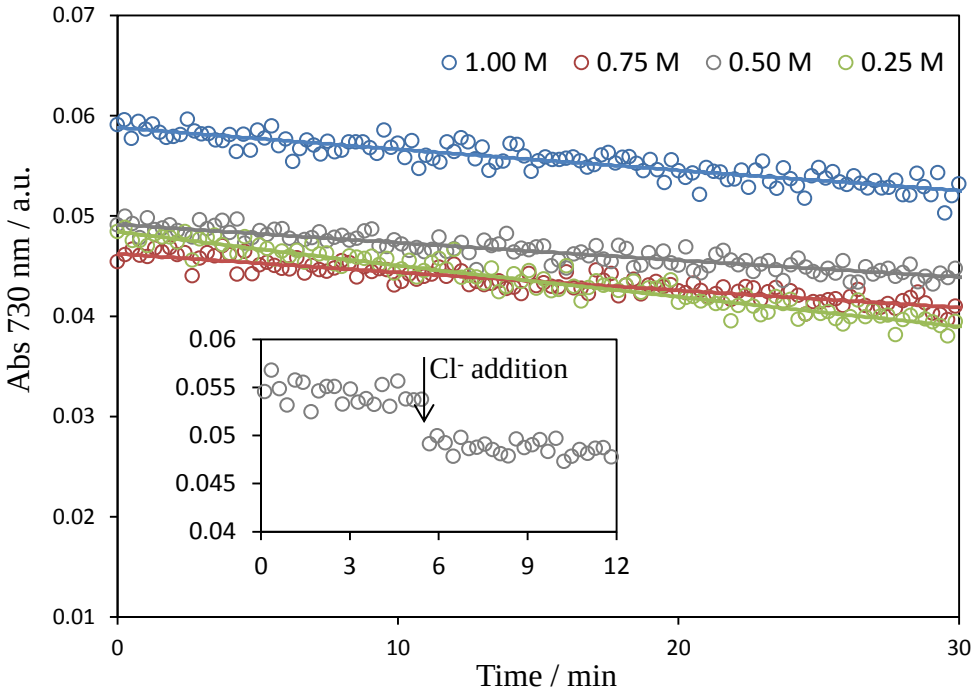

Figure 3-11 Time-traces for λ = 730 nm of 0.8 mM Fe-*tpena* in 0.1 M $NaClO_4$ showing Fe^{IV}-*tpena* decay after 30 min-electrolysis has been stopped and different amount of sodium chloride has been added to the Fe^{IV}-*tpena* solution (coloured circles: blue, 1.00 M NaCl; red: 0.75 M NaCl, grey, 0.50 M NaCl; green 0.25 M NaCl) and its exponential fit (straight line) Insert: the UV absorbance at 730 nm before and after 0.50 M NaCl addition .

Table 3-2 Obvious Rate Constants for Fe^{IV}-*tpena* decay at different NaCl levels

NaCl concentration/M	1.00	0.75	0.50	0.25
k'_{obs} / s^{-1}	6.3×10^{-5}	6.9×10^{-5}	6.3×10^{-5}	1.0×10^{-4}
Standard Error / s^{-1}	2.5×10^{-6}	1.8×10^{-6}	1.7×10^{-6}	2.1×10^{-6}

3.4 Conclusion

Fe^{IV}-*tpena* can be generated electrochemically at potentials higher than 1.3 V *vs* NHE with the concentration of Fe^{IV}-*tpena* formed readily quantifiable using UV-vis spectroscopy. Fe^{IV}-*tpena* is relatively stable in acidic solutions and decays more rapidly at higher pH due to a faster rate of hydroxide oxidation than that of water oxidation. The positive charge and the hydrogen-bonding potential of Fe^{IV}-*tpena* presumably renders

this species more active toward anions (such as OH^-) than uncharged species (such as H_2O). This is also true for formic acid and formate anion oxidation, where the reaction rate constants are k_{HCOOH} = 0.20 ± 0.02 $M^{-1}s^{-1}$ and k_{HCOO^-} =1.2 ± 0.1 $M^{-1}s^{-1}$, respectively. In studies of RhB degradation, Fe^{IV} exhibited powerful decolourisation ability along with deethylation.

Overall, Fe^{IV}-*tpena* has been demonstrated to be relatively stable in aqueous solution and to exhibit the ability to oxidize a range of substrates that contain C-H or O-H bonds, especially in acidic conditions, yet is not reactive toward chloride, a common constituent of natural waters. The "pulse" electro-chemically generated Fe^{IV}-*tpena* studies described here have provided considerable insight into the fundamental kinetics behaviour of Fe^{IV}-*tpena* where this species is the only active oxidant. With regard to practical applications of electrochemically activated Fe-*tpena*, future studies should focus on Fe-*tpena* immobilisation and ongoing electrolysis in the presence of both Fe-*tpena* and substrates at circumneutral pH.

Chapter 4.
Chemical activation of Fe-*tpena* by hydrogen peroxide

4.1 Introduction

Hydrogen peroxide (H_2O_2) is a common oxidant employed in water and wastewater treatment processes which, although of minimal reactivity on its own despite its high formal oxidation potential of 1.80 V (Kurniawan and Lo, 2009), when used both in combination with other oxidants (e.g., combined with ozone in the peroxone process (Paillard et al., 1988)) or as a means to activate elements such as iron and copper to more reactive entities, has found widespread application in oxidation technologies. In the typical Fenton reaction with ferrous iron (Fe(II)) at low pH, Fe(II) reduces H_2O_2 to $HO^{\bullet}$ with concomitant production of ferric iron (Fe(III)). As well as being an effective oxidant, H_2O_2 is also able to act as a reductant to reduce Fe(III) back to the desired Fe(II) through the intermediacy of an iron-peroxo complex (De Laat and Gallard, 1999). Under circumneutral conditions, the Fe(III)-EDTA complex is also known to form a peroxo- species (Brausam and van Eldik, 2004) that has been demonstrated to possess oxidative abilities (Walling et al., 1975).

As a relatively clean oxidant in water treatment, hydrogen peroxide is capable of oxidising Fe^{III}-TAML species to Fe^{IV}-TAML at ambient temperature, though at a lower rate than m-chloroperoxybenzoic acid and other organic peroxides (Collins and Ryabov, 2017). In comparison, the reaction between hydrogen peroxide and iron(II) phthalocyanine has been shown to produce hydroxyl radicals (Hu et al., 2016, Yuan et al., 2015). The end product of the interaction of hydrogen peroxide with Fe-*tpena* remains unclear with investigation of this system expected to provide a useful.

comparison of how these high-valent iron-oxo species compare to existing hydroxyl radical-based systems.

Although the interaction of Fe-*tpena* with H_2O_2 is expected to occur, it is unclear whether or not the well-characterised high-valent Fe^{IV}-*tpena* complex will be formed. This chapter aims to explore the nature of the oxidants formed in this system, with the potential role of Fe^{IV}-*tpena* deduced by comparing the results observed in the Fe^{III}-*tpena* + H_2O_2 system to those where, instead, Fe^{IV}-*tpena* was generated electrochemically and reacted with both the substrates under investigation and with H_2O_2. For application in ambient aqueous environments, a matrix with similar ionic strength to circumneutral natural water (pH ~8) has been used as Fe-*tpena* has shown good stability at pH < 9 (Chapter 3). The oxidative ability of the system and the nature of the active oxidant (Fe^{IV}-*tpena* or hydroxyl radicals) is examined through oxidation of formate, rhodamine B and phthalhydrazide for a range of reactant loadings. H_2O_2 consumption is also monitored where possible.

4.2 Experimental methods

4.2.1 Solution preparations

All solutions were prepared in 18 MΩ cm Milli-Q water (mQ) obtained from a Millipore Milli-Q system.

The experiments were all conducted in 10 mM NaCl with 2 mM $NaHCO_3$ equilibrated with ambient air (pH ~ 8).

An Fe^{IV}-*tpena* solution (0.8 mM per iron, native pH ~3, in 0.1 M $NaClO_4$) was prepared as described in §3.3.2 in order to investigate the reaction between Fe^{IV}-*tpena* and both phthalhydrazide and H_2O_2.

A titanium^{IV} oxysulfate reagent for H_2O_2 quantification was prepared by dissolving $TiOSO_4$ (25 g) in a 2 M sulfuric acid solution (1 L) under constant stirring with this compound reportedly stable for up to 4 months when stored in a cool, dark place.

4.2.2 Hydroxyl radicals detection

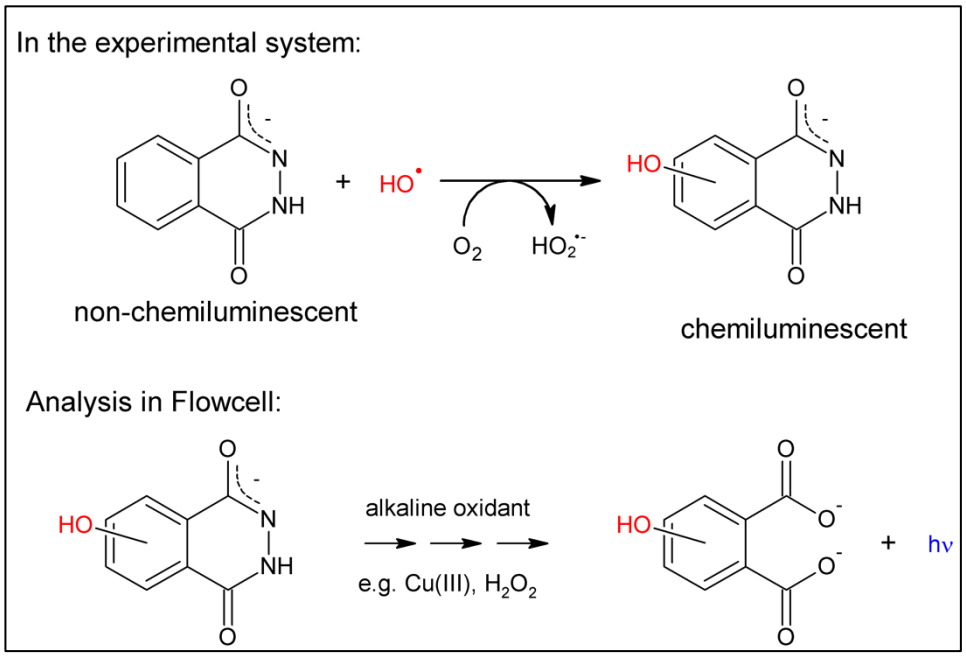

Figure 4-1 Mechanism of the phthalhydrazide (Phth) chemiluminescence method

Hydroxyl radicals ($HO^{\bullet}$) are measured using a chemiluminescence method based upon the hydroxylation of phthalhydrazide (Phth) to a chemiluminescent hydroxylated form (Phth-OH) as outlined in Figure 4-1. The term "Phth-OH" refers to the total concentration of Phth that is oxidized by $HO^{\bullet}$ with the chemiluminescent analyte 5-hydroxy-phthalazine-1,4-dione(5-HO-Phth) formed in approximately 20% yield. The Phth-OH concentration was calibrated using a Fenton secondary calibration system.

4.2.2.1 Preparation of calibration standard

The calibration standard was prepared by generating a previously calibrated amount of Phth-OH through Fenton chemistry by adopting the following procedure: 1) pipette 9.92 mL of pH 3, 10 mM NaCl/0.55 mM phthalhydrazide into a brown glass vessel; 2) add 50 µL 10 mM H_2O_2 and then commence a timer upon addition of 25 µL 4 mM Fe(II) solution (prepared daily by dissloving $Fe(II)SO_4 \cdot 7H_2O$ into 10^{-4} M HCl) under stirring; and 3) quench the reaction after precisely one hour by addition of 50 µL of 10 mM

diethylenetriaminepentaacetic acid (DTPA). The solution thus formed will contain "Phth-OH" at a concentration of 20.6 μM and is to be used within one week.

4.2.2.2 Preparation of samples

For $HO^{\bullet}$ measurement in the Fe-*tpena*/H_2O_2 system, Fe^{III}-*tpena* (100 μM per Fe) was added to a Phth (0.55 mM in the pH 8 matrix) solution and a timer conmmenced upon H_2O_2 addition (1 to 5 mM) with samples taken at certain time points for Phth-OH or Phth measurement. Phth concentration was determined spectrophotometrically using $\varepsilon_{310} = 5640\ M^{-1}cm^{-1}$.

4.2.2.3 Investigation of Fe^{IV}-tpena reaction with phthalhydrazide

To test whether Fe^{IV}-*tpena* could hydroxylate Phth to form 5-HO-Phth, an electro-generated Fe^{IV}-*tpena* solution was used instead of the Fe-*tpena*/H_2O_2 mixture. Phth solution (0.55 mM in the pH 8 matrix) was mixed with the Fe^{IV}-*tpena* solution 1:1 by volume and sampling commenced immediateley with samples taken at particular time intervals. For calibration purposes, a corresponding sample matrix was prepared by mixing (in equal proportions) the Phth solution (0.55 mM in the pH 8 matrix) with a 0.1 M $NaClO_4$ solution whose pH had been adjusted to 3 using $HClO_4$.

4.2.2.4 Phth-OH measurement

Chemiluminescence (CL) quantification of Phth-OH was performed by continuously pumping two solution streams (A and B) through a Waterville Analytical FeLume system. Stream A contained v/v 40% sample, 58% 1 M Na_2CO_3 (adjusted to pH 11) and 2% 200 mM H_2O_2 while stream B contained v/v 42% 1 M Na_2CO_3 (adjusted to pH 11), 56% mQ water and 2% 10 mM diperiodatocuprate(III) (DPC). H_2O_2 and DPC was added immediately prior to the measurement as they are the least stable components. When calibrating (performed daily with sample tests), the sample was replaced with a calibration standard diluted in the sample matrix containing ~55 mM Phth with multiple dilution used to minimize any matrix effects.

It was verified that 100 μM Fe^{III}-*tpena* did not interfere with the detection method through addition to known calibration standards (Figure 4-2).

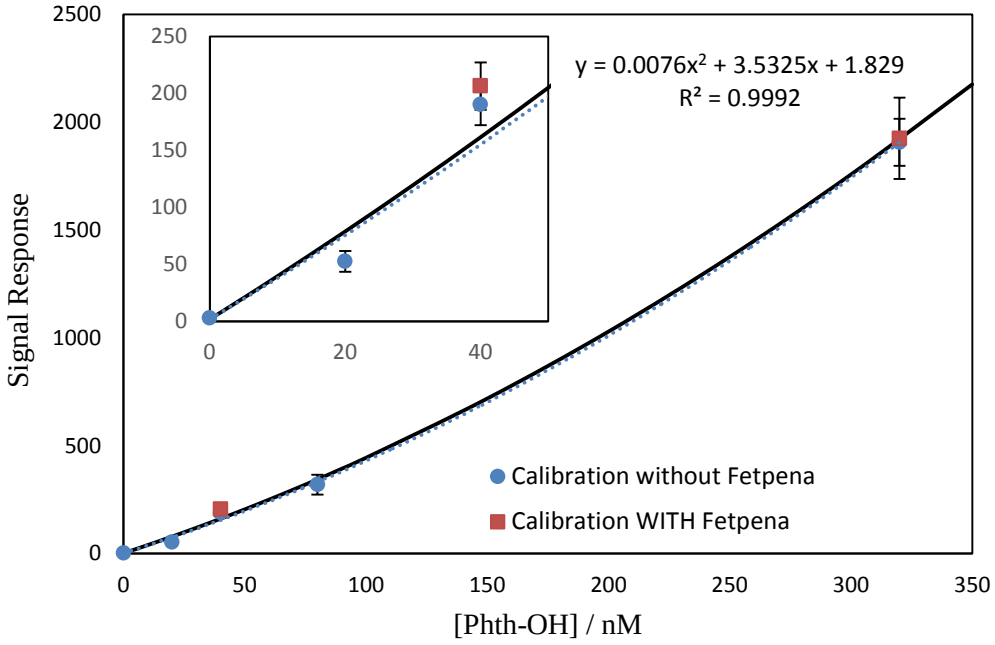

Figure 4-2 Control experiment calibrations of Phth-OH with/without Fe-*tpena*. Insert: enlarged figure.

4.2.3 Substrate degradation experiments

For formate degradation, HCOONa (from a 200 mM HCOONa stock solution) and $H^{14}COONa$ (45 nM from a 10 μM stock solution) was mixed with Fe^{III}-*tpena* (from a 2 mM per Fe mQ stock solution) in the pH 8 matrix with reaction time commenced upon H_2O_2 addition. Samples (0.2 mL) were taken at desired time points (with one taken prior to H_2O_2 addition) and quenched with 1M formic acid (1.8 mL). ^{14}C-labelled formate in the sample was then measured using an Ultima Gold scintillation cocktail (PerkinElmer) and a PerkinElmer Tri-Carb 2910TR liquid scintillation analyzer after $^{14}CO_2$ was liberated from the acidified sample by aeration (10 min) with the measured ^{14}C-labelled formate remaining then scaled to enable quantification of change in total formate concentration in the reactor. In some cases, H_2O_2 addition was repeated after the previous reaction had finished in order to examine the recyclability of the Fe^{III}-tpena.

For RhB degradation, RhB (from a 10 mM stock solution in mQ) and Fe-*tpena* (from a 2 mM per Fe mQ stock solution) were mixed in the pH 8 matrix in a 1 cm quartz

cuvette. Upon the addition of H_2O_2, UV-vis spectra recording was started immediately in kinetic scan mode using an Agilent 8453 spectrophotometer. The spectra were analyzed as decribed in §2.2.5.

4.2.4 Hydrogen peroxide measurement

Hydrogen peroxide consumption was monitored in parallel experiments to the formate oxidation studies in experiments that were identical except for the absence of ^{14}C-formate. Samples were taken at desired time points commencing from H_2O_2 addition. H_2O_2 concentration in a pure Fe^{III}-*tpena* solution was also measured to confirm Fe^{III}-*tpena* did not lead to artefactual measurements.

H_2O_2 concentration in the samples was quantified by a colorimetric method (Eisenberg, 1943) where 1 mL of the titanium^{IV} oxysulfate reagent was added to 2 mL of the sample (diluted to fall in the calibration range where necessary) to react with H_2O_2 and produce a yellow-colored pertitanate complex which was then quantified by its absorbance at 407 nm (ε = 475.1 $M^{-1}cm^{-1}$) (Saherfield and Bonnell, 1955) using an Agilent Cary 60 spectrophotometer using 1 cm quartz cuvettes. An example calibration standard curve is shown in Figure 4-3.

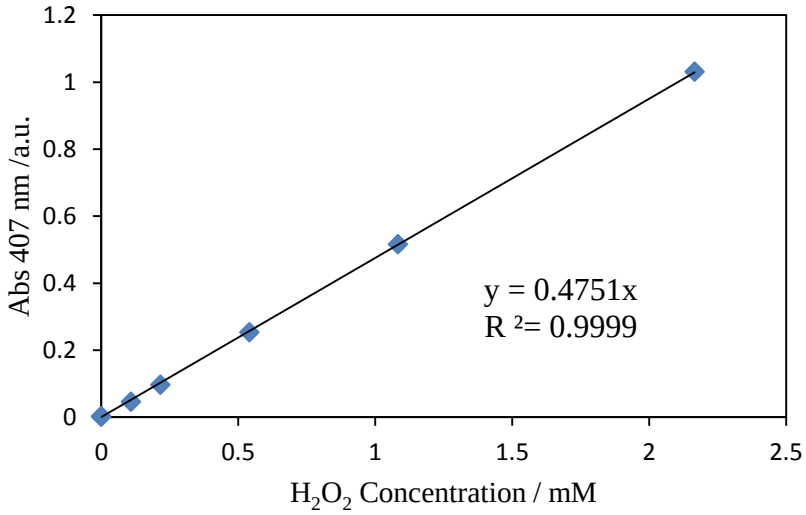

Figure 4-3 H_2O_2 calibration standard curve

4.2.5 Kinetic modelling

Numerical kinetic modelling of reaction schemes was implemented using Kintecus v. 5.20 (Ianni, 2014) with the main reactions chosen based on experimental results and trial-and-error fitting.

Modelling details and other basic kinetic analyses are described in the following section, together with experimental results.

4.3 Results and discussion

4.3.1 Reactivity of Fe^{III}-*tpena* and Fe^{IV}-*tpena* with H_2O_2

When H_2O_2 was added to Fe^{III}-*tpena*, no characteristic absorbance was observed at its absorbance maximum at 730 nm. However, there was a clear decrease in the UV region associated with H_2O_2 absorbance suggesting that reaction was occurring. By consideration of the approximate molar absorptivity of Fe^{IV}-*tpena* of $\varepsilon_{730} \approx 260$ $M^{-1}cm^{-1}$, this would suggest that either Fe^{IV}-*tpena* does not form, or that it's concentration is below that observable by spectrophotometry. Taking a minimum observable absorbance of 0.001, this would suggest that the Fe^{IV}-*tpena* concentration must be less than ~ 5 μM. As will be discussed below, evidence suggests that Fe^{IV}-*tpena* does form in this system, but its concentration is below the observable limit of the equipment used.

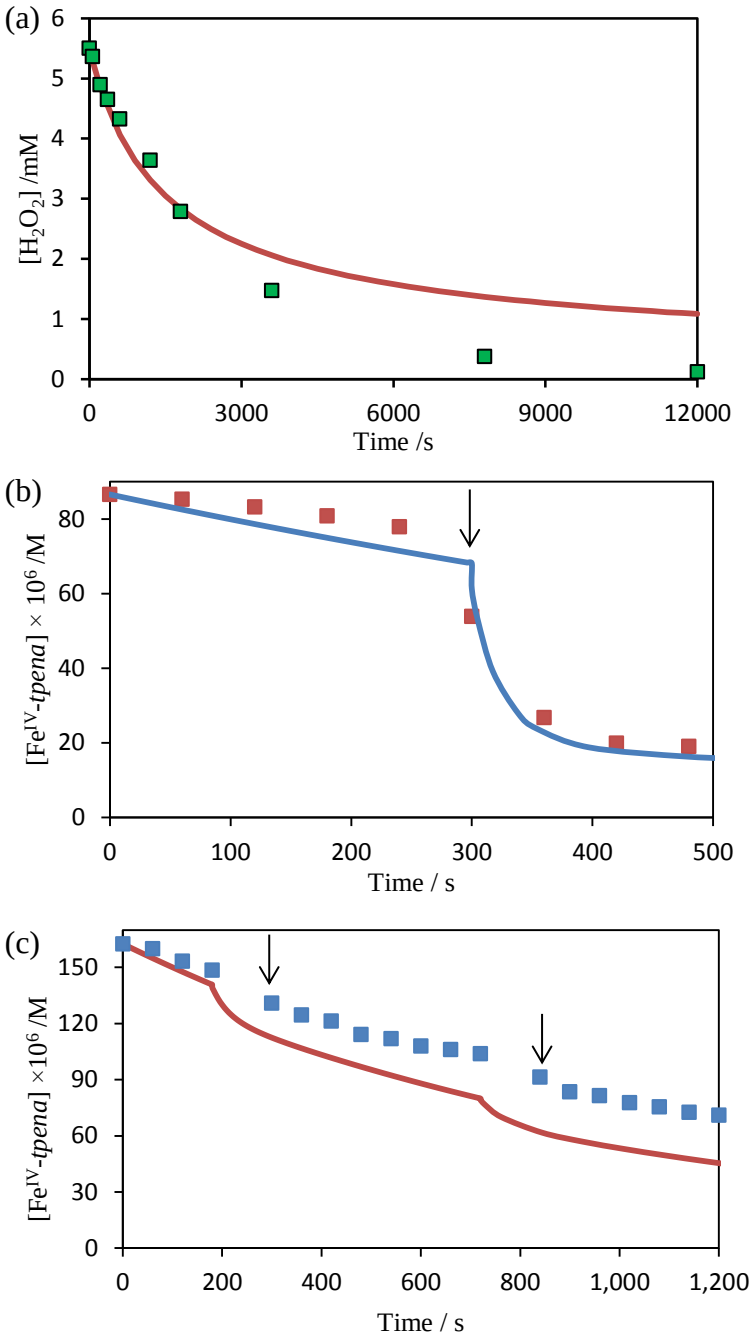

Figure 4-4 Experimental (squares) and modelled (lines) data of (a) H_2O_2 consumption in the presence of 100 µM (per Fe) Fe^{III}-*tpena* at pH 8, (b) electro-generated Fe^{IV}-*tpena* decay with one addition (vertical arrow) of 100 µM H_2O_2 at pH 3,.and (c) electro-generated Fe^{IV} decay with two additions of 10 µM H_2O_2 at pH 3.

Measurements of H_2O_2 concentrations confirmed the spectroscopic observation that reaction with Fe^{III}-*tpena* was occurring (Figure 4-4 a) with 5 mM H_2O_2 completely

consumed by 100 µM Fe^{III}-*tpena*. It is noteworthy that all the H_2O_2 was removed, despite it being present in 50× excess relative to the Fe^{III}-*tpena*, suggesting that the Fe^{III}-*tpena* acts catalytically to remove H_2O_2. If H_2O_2 can indeed oxidize Fe^{III}-*tpena* to Fe^{IV}-*tpena*, this suggests that Fe^{IV}-*tpena* must also be reactive with H_2O_2, or it would presumably increase to observable concentrations and the H_2O_2 consumption would cease when all the Fe^{III}-*tpena* was oxidized to Fe^{IV}-*tpena*. The reaction of electrochemically-generated Fe^{IV}-*tpena* with H_2O_2 was investigated and it was found that Fe^{IV}-*tpena* was indeed reactive with H_2O_2 (Figure 4-4 b), presumably generating Fe^{III}-*tpena* and superoxide ($O_2^{\bullet-}$). The reactivity of both Fe^{III}-*tpena* and Fe^{IV}-*tpena* with H_2O_2 explains both why Fe^{IV}-*tpena* could not be directly observed and how the Fe^{III}-*tpena* may act catalytically. The simplest interpretation of these results is a competing sequence of reactions of the form shown below (reaction 1 and 2). The stoichiometry as well as the products of H_2O_2 interaction (i.e., whether radical or diamagnetic) could not be assessed at this stage.

$$Fe^{III}\text{-}tpena + H_2O_2 \rightarrow Fe^{IV}\text{-}tpena \quad (1)$$

$$Fe^{IV}\text{-}tpena + H_2O_2 \rightarrow Fe^{III}\text{-}tpena \quad (2)$$

A detailed reaction scheme is developed later as described in Section 4.3.5 where a peroxo complex (Fe^{III}-*tpena*-H_2O_2) has been taken into consideration. Its formation in organic solution (acetonitrile) has also been studied by our collaborating colleagues at the University of Southern Denmark (Wegeberg et al., 2018). Solid lines in Figure 4.4 show how well the model (Table 4-2) represents the interactions between $Fe^{III/IV}$-*tpena* and H_2O_2 with good agreement between model and experimental results providing support for the proposed reaction scheme (which is entirely consistent with the earlier work in acetonitrile).

4.3.2 Oxidation of formate

The oxidation of formate was examined to determine whether a strong oxidant was formed during the reaction of Fe^{III}-*tpena* with H_2O_2. As can be seen in Figure 4-5,

significant formate oxidation accompanied this reaction, confirming that a strong oxidant did indeed form. Initially, as proposed in the previous section, this strong oxidant was presumed to be Fe^{IV}-*tpena* with the veracity of this assumption readily tested as the rate constant of this reaction has been determined in Chapter 3. From Figure 4-5, the pseudo first-order decay rate for formate was found to be 2.6×10^{-4} s^{-1}; using the known rate constant for the Fe^{IV}-*tpena* + formate reaction of 1.2 $M^{-1}s^{-1}$ therefore requires a steady-state Fe^{IV}-*tpena* concentration of ~200 μM in order to explain the observed decay rate. This very high, readily observable, Fe^{IV}-*tpena* concentration is in stark contrast to the lack of any observable absorbance peaks attributable to Fe^{IV}-*tpena*, a well as being greater than the total added Fe^{III}-*tpena*, and is strong evidence that Fe^{IV}-*tpena*, although likely to be present, cannot be the sole oxidant formed in this system. The most obvious candidate for this missing strong oxidant would be the hydroxyl radical ($HO^{\bullet}$) presumably formed through a reaction such as:

$$Fe^{III}\text{-}tpena + H_2O_2 \rightarrow Fe^{IV}\text{-}tpena + HO^{\bullet} \quad (3)$$

The possibility of $HO^{\bullet}$ formation was assessed using phthalhydrazide and will be discussed in the next section.

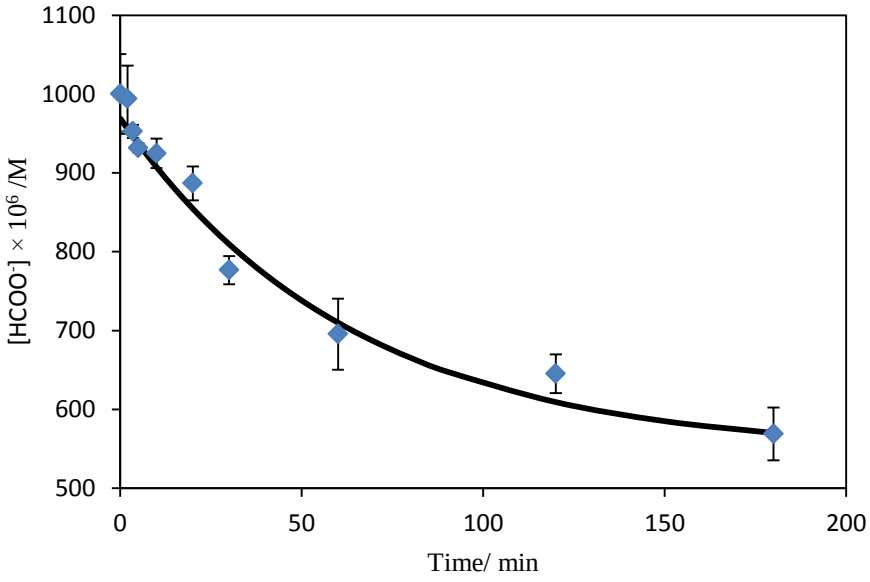

Figure 4-5. Oxidation of 1 mM formate by 100 μM Fe-*tpena* and 20 mM H_2O_2 at pH 8. Solid line is a pseudo first-order decay fit (k' = (2.6 ± 0.5) × 10^{-4} s^{-1})

4.3.3 Hydroxyl radical formation

The formation of $HO^{\bullet}$ in the Fe-*tpena*/H_2O_2 system was examined using phthalhydrazide, which forms chemiluminescent 5-hydroxy phthalazine-1,4-dione upon oxidation by $HO^{\bullet}$. First of all, it was important to determine whether or not Fe^{IV}-*tpena* could hydroxylate Phth to generate [Phth-OH]. This was examined using electrochemically activated Fe^{IV}-*tpena* (in 0.1 M $NaClO_4$), which was mixed equally with 550 μM Phth (in the default matrix) and sampled at 0 min and 3 min (where Fe^{IV}-*tpena* has been consumed by Phth as shown in the insert in Figure 4-6) for Phth-OH measurement. Calibration with the mixed matrix of half 0.1 M $NaClO_4$ and half default matrix resulted in typical calibrations (curve in Figure 4-6), yet no Phth-OH was observed (square symbols in Figure 4-6) indicating that Fe^{IV}-*tpena* does not hydroxylate Phth. As a result, any detection of Phth-OH can be specifically attributed to $HO^{\bullet}$.

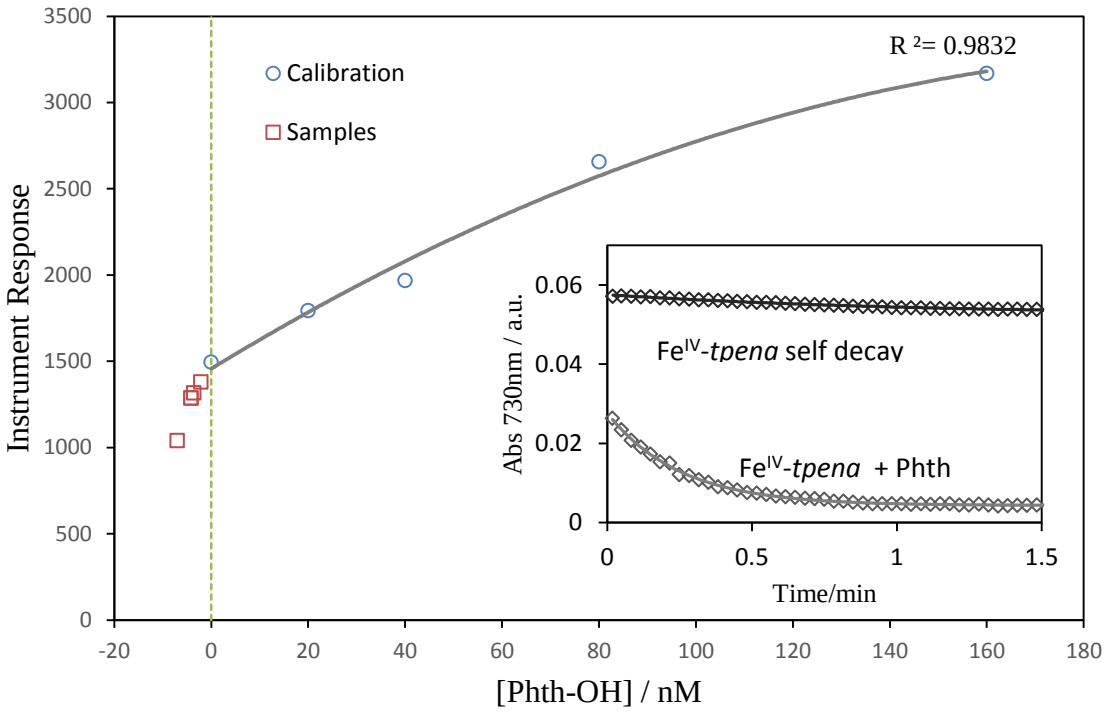

Figure 4-6 Reaction of Fe^{IV}-*tpena* with Phth. The inset shows absorbance traces of Fe^{IV}-*tpena* decay in the presence and absence of Phth, where the Fe^{IV}-*tpena* was electrochemically generated in 0.1 M $NaClO_4$ by the usual procedure, and then mixed 50:50 with 0.55 mM Phth in the default pH 8 buffer (pH ends up at 4). The main figure shows calibration of [Phth-OH] in a matrix of 50% 0.1 M $NaClO_4$ and 50% default buffer with 0.55 mM Phth (circles) at pH 4 and also the samples taken during oxidation experiment in the insert (squares) during the reaction between electrochemically generated Fe^{IV}-*tpena* and Phth. The reaction was sampled at 0 min and 3 min (where Fe^{IV}-*tpena* has been consumed by Phth as shown in the insert, with no detectable Phth-OH observed (detection limit ~ 20 nM)

When Phth is oxidized by the Fe-*tpena*/H_2O_2 system, significant Phth-OH production is observed (Figure 4-7 A), confirming the formation of $HO^{\bullet}$ in this system. Although Phth appears to decay completely following pseudo first-order kinetics (Figure 4-7 B), the concentration of Phth-OH peaks at only about 10% of the total Phth concentration, suggesting that Phth is oxidized by both $HO^{\bullet}$ (to Phth-OH) and Fe^{IV}-*tpena* (to other products).

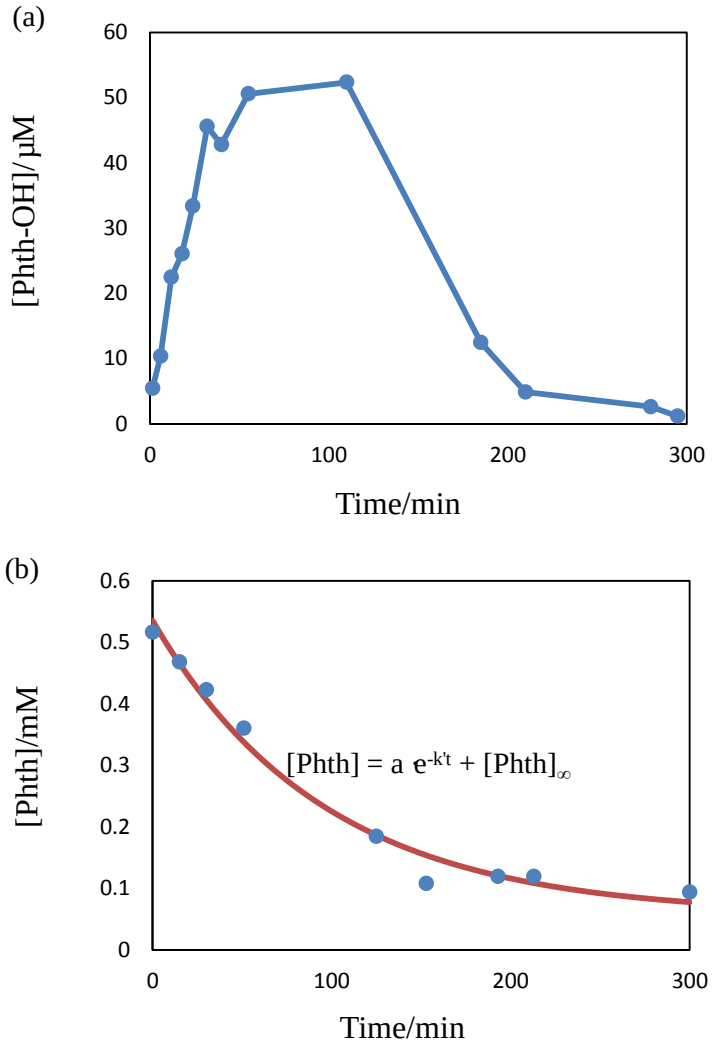

Figure 4-7 (a) The formation and degradation of Phth-OH and (b) the degradation of Phth and its exponential fit when 5 mM of H_2O_2 is added to 100 μM Fe-*tpena* /0.55 mM Phth at pH8.

A simplified scheme of Phth decay is presented in Figure 4-8. As the rate constant for both $HO^{\bullet}$ and Fe^{IV}-*tpena* with Phth are known (§3.3.5), and as it is likely that the rate constant for oxidation of Phth-OH by $HO^{\bullet}$ and Fe^{IV}-*tpena* is probably similar to that for Phth, this simple reaction scheme can be solved numerically.

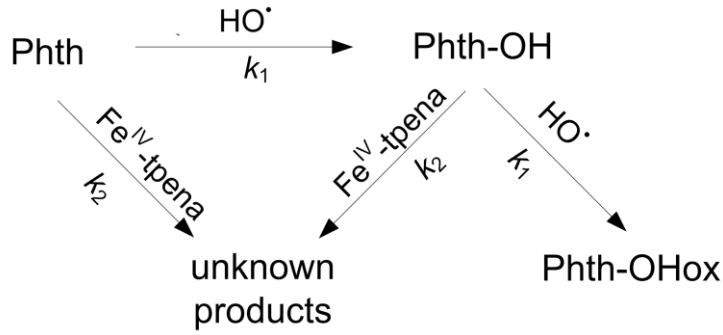

$$\frac{d[Phth]}{dt} = -(k_1[HO^{\bullet}] + k_2[Fe^{IV}])[Phth] = -k'_{obs}[Phth]$$

(Eq. 4-1)

$$\frac{d[Phth-OH]}{dt} = k_1[HO^{\bullet}][Phth] - k_1[HO^{\bullet}][Phth-OH] - k_2[Fe^{IV}][Phth-OH] = k_1[HO^{\bullet}][Phth] - k'_{obs}[Phth-OH]$$

(Eq. 4-2)

Figure 4-8 Pathways of Phth degradation in the H_2O_2/Fe-*tpena* system

At the plateau of Phth-OH concentration, its rate of change is 0, according to Eq.4-2:

$$\frac{d[\text{Phth-OH}]}{dt} = 0$$

$$\Rightarrow k_1[\text{HO}^{\bullet}][\text{Phth}]_{\text{peak}} = k'_{obs}[\text{Phth-OH}]_{\text{peak}}$$

$$[\text{HO}^{\bullet}] = \frac{k'_{obs}[\text{Phth-OH}]_{\text{peak}}}{k_1[\text{Phth}]_{\text{peak}}}$$

(Eq.4-3)

This allows for the $HO^{\bullet}$ concentration to be estimated. Feeding back to Eq.4-1, the Fe^{IV}-*tpena* concentration can be estimated as well.

$$k'_{obs} = k_1[\text{HO}^{\bullet}] + k_2[\text{Fe}^{\text{IV}}] \Rightarrow [Fe^{IV}] = \frac{k'_{obs} - k_1[\text{HO}^{\bullet}]}{k_2}$$

(Eq. 4-4)

Concentrations of hydroxyl radicals and Fe^{IV}-*tpena* at the [Phth-OH] plateau estimated using the above approach are listed in Table 4-1 when different amounts of H_2O_2 (1, 2 and 5 mM) were used for Fe-*tpena* (100 μM per Fe) activation (up to three points at the [Phth-OH] plateau were selected for calculation). k'_{obs} and its distribution (as $k_1[HO^{\bullet}]$ and $k_2[Fe^{IV}\text{-}tpena]$) are illustrated in Figure 4-9a.

Table 4-1 Estimated hydroxyl radicals and Fe^{IV}-*tpena* concentrations at different time points during [Phth-OH] plateau

$[H_2O_2]_0$ and k'_{obs}	[Phth-OH] $\times 10^6$ /M	[Phth] $\times 10^6$ /M	$[HO^{\bullet}] \times 10^{16}$ /M	$[Fe^{IV}\text{-}tpena] \times 10^7$ /M
$[H_2O_2]_0$ =1mM $k'_{obs} = 1.3\times10^{-4}\ s^{-1}$	8.81	420	5.0	5.0
$[H_2O_2]_0$ =2mM $k'_{obs} = 1.0\times10^{-4}\ s^{-1}$	15.7	340	9.1	3.9
$[H_2O_2]_0$ =5mM $k'_{obs} = 1.7\times10^{-4}\ s^{-1}$	51.5	270	66	5.5

As shown in Table 4-1, the predicted [Fe^{IV}-*tpena*] is rather stable at 0.5 μM ($[H_2O_2]_0$ = 1mM), 0.39 μM ($[H_2O_2]_0$ = 2mM) and 0.55 μM ($[H_2O_2]_0$ = 5mM) and does not show obvious correlation with $[H_2O_2]_0$. [$HO^{\bullet}$], on the other hand, though on average present at concentrations 10^8 times lower than [Fe^{IV}-*tpena*], increases exponentially with initial peroxide loading as shown in Figure 4-9b. This means that excessive H_2O_2 leads to the generation of significantly more $HO^{\bullet}$ and suggests that the mechanism resulting in this behaviour may be complex.

This basic modelling also allows for an estimate of the contribution of each oxidant to the observed degradation of Phth, which is given by $k_1[HO^{\bullet}]$ and $k_2[Fe(IV)]$ shown in Figure 4-9a. As can be noted, hydroxyl radicals contribute less than 5% of the overall Phth oxidation at lower H_2O_2 loading (≤ 2mM) with this ratio rising to 20% at a high H_2O_2 loading of 5 mM.

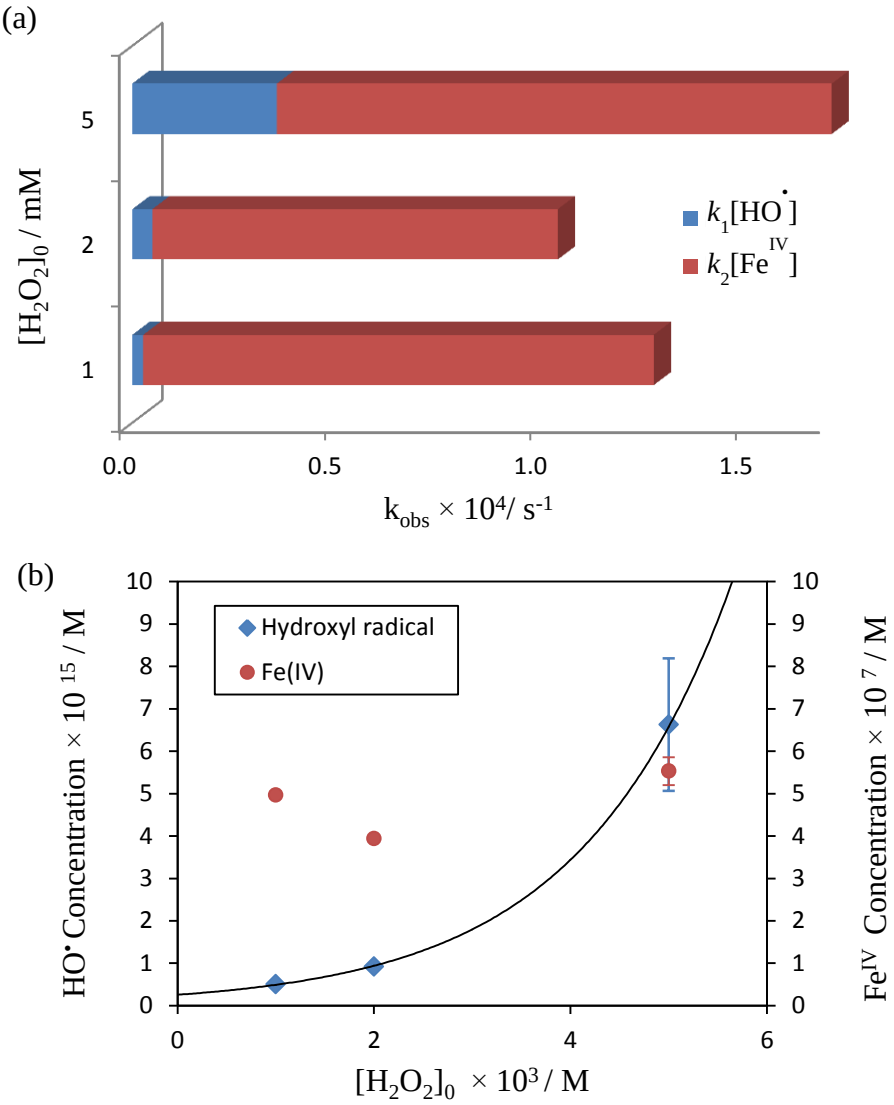

Figure 4-9 (a) Contribution of $HO^{\bullet}$ (blue, $k_1[HO^{\bullet}]$) and Fe^{IV}-*tpena* (red, $k_2[Fe^{IV}$-*tpena*]) to the observed pseudo first-order degradation rate constant for Phth at 100 μM (per Fe) Fe*tpena* and varied H_2O_2 in the pH 8 buffer. (b) Estimated [$HO^{\bullet}$] and [Fe^{IV}-*tpena*] at Phth-OH plateau when varied $[H_2O_2]_0$ was used at pH 8.

As a very active and non-selective oxidising agent, as well as inducing substrate degradation, $HO^{\bullet}$ may also potentially lead to undesired reactions such as destruction of the *tpena* ligand. Alternatively, it may also be possible that $HO^{\bullet}$ acts benignly to oxidize Fe^{III}-*tpena* to Fe^{IV}-*tpena*. These possibilities will be explored in later sections.

It should also be noted that generation of free Fe^{III} (which induces Fenton-like reaction to give •OH) can be readily ruled out. At low pH, this reaction proceeds through an

observable Fe^{III}-peroxo intermediate in equilibrium with Fe^{III} and H_2O_2 (Gallard et al., 1999), with no reason to assume this mechanism is any different at higher pH not readily accessible to experimentation. High concentrations of both Fe^{III} and H_2O_2 are required for any significant formation of the peroxo complex with this issue exacerbated by the exceedingly low solubility of inorganic Fe^{III} at pH 8. Using a speciation model developed from a combination of formation constants from Pham et al. (2006) and Gallard et al. (1999), under the conditions of this study (pH 8, 100 μM Fe^{III}, 5 mM H_2O_2), it is seen that the solubility of Fe(III) is approximately 0.1 nM, with peroxo complexes accounting for only 0.2 pM. The formation rate of Fe^{II} from these peroxo complexes obeys first order kinetics ($k' = 2.7 \times 10^{-3}$ s^{-1}) (De Laat and Gallard, 1999), which would suggest an Fe^{II} formation rate of 5.4×10^{-17} M s^{-1}. Considering the rate of reaction of inorganic Fe^{II} with H_2O_2 at pH 8 is ~ 10^5 $M^{-1}s^{-1}$ (Miller et al., 2009), this gives a steady state Fe^{II} concentration of ~10^{-18} M, equivalent to a $HO^{\bullet}$ production rate of ~5×10^{-16} M s^{-1}; i.e., a potential for formation of ~10 pM of $HO^{\bullet}$ over a five hour experiment. However, as others in the Waite group have previously demonstrated, as the inorganic Fe^{II} + H_2O_2 reaction does not form an oxidant capable of hydroxylating phthalhydrazide at pH 8 anyway (Miller et al., 2016), it can be concluded that this process would be incapable of explaining the observed data even if it did not occur at an exceedingly slow rate.

4.3.4 Repeated addition of H_2O_2

The catalytic removal of H_2O_2 by Fe-*tpena*, although undesirable as this leads to inefficient generation of oxidants by H_2O_2, does suggest that the Fe-*tpena* should at least, in principle, be able to be reused many times simply through addition of further H_2O_2. To study the longevity of Fe-*tpena* in the system, a three-day formate degradation test with a one-off addition of Fe-*tpena* and repeated additions of H_2O_2 was conducted. Although initially quite effective at degrading formate, by the third spike of H_2O_2 there was no further change in [$HCOO^-$] (Figure 4-10a). There are two possibilities for this decreased efficacy; first, that the Fe-*tpena* complex has been damaged and rendered ineffective through the course of the oxidation reaction or, secondly, that the Fe-*tpena*

complex is not stable at the pH of the experiment and the Fe has simply de-coordinated and hydrolysed. To test which hypothesis was operative, a pH 8 Fe-*tpena* solution was prepared and allowed to age for 5 days without addition of H_2O_2 or formate, before then performing an oxidation experiment in the usual manner. This five day aged Fe-*tpena* was found to be similarly effective to freshly diluted Fe-*tpena* (Figure 4-10b), suggesting that that Fe-*tpena* (100 μM) is oxidatively destroyed during the course of the reaction with H_2O_2. It was found that 100 μM Fe-*tpena* was effective for only two additions of 5 mM H_2O_2 in the presence of 1 mM formate.

As will be discussed in later sections, this behaviour was accounted for in the modelling, with the model able to reproduce this complex degradation behaviour (see model result in Figure 4-10a). This degradation appears mostly attributable to oxidation of the complex by $HO^{\bullet}$.

Another important conclusion from the 5-day-aged Fe-tpena experiment is that Fe-*tpena* is quite stable (at least for five days) in the matrix used to mimic ambient aqueous conditions (10 mM NaCl, 2 mM $NaHCO_3$). This has been used as the default matrix in all later sections unless otherwise stated.

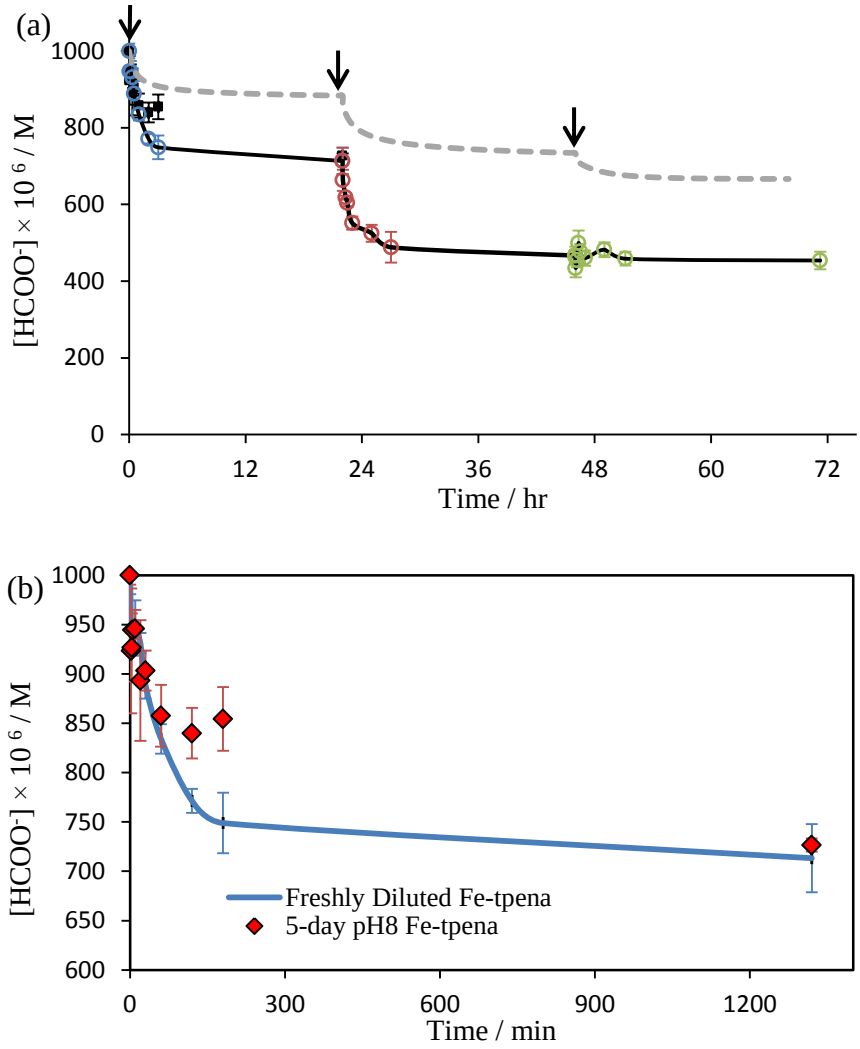

Figure 4-10 (a) Experimental data (circles) and model data (dash line) of formate degradation with repeat additions of 5 mM H_2O_2 in 100 μM (per Fe) Fe-*tpena* at pH 8. (b) Formate degradation by 5mM H_2O_2 added to a 5-day-aged pH 8 Fe-*tpena* (100 μM per Fe) solution

4.3.5 Detailed investigation of formate and Phth oxidation by Fe-*tpena*/H_2O_2 system

The key features of this system have been identified in the previous sections; namely that 1) Fe^{III}-*tpena* is oxidized by H_2O_2, 2) Fe^{IV}-*tpena* is reduced by H_2O_2, and 3) $HO^{\bullet}$ is also formed in this process, presumably during the Fe^{III}-*tpena* + H_2O_2 reaction. However, the details of these interactions are not clear with many outstanding and important questions remaining. Experiments have been performed at a range of Fe-

tpena, H_2O_2 and formate concentrations to allow for development of a mechanistic kinetic model in order to refine the details of the conceptual model advanced thus far. Formate provides the ideal substrate for this investigation as its oxidation proceeds directly to only two simple products, $CO_2^{\bullet-}$ and $O_2^{\bullet-}$, with the chemistry of these species well known (Buxton et al., 1988, Bielski et al., 1985). That the rate constants for formate oxidation by both $HO^{\bullet}$ and Fe^{IV}-*tpena* are well-constrained and unambiguously determined means that the modelling process can be focused on H_2O_2 and Fe-*tpena* interactions.

The most critical factor for development of a mechanistic model is to define the nature of the interaction of Fe^{III}-*tpena* and H_2O_2. The simplest reaction consistent with the behaviour outlined so far is reaction 3:

$$Fe^{III}\text{-}tpena + H_2O_2 \rightarrow Fe^{IV}\text{-}tpena + HO^{\bullet}$$

However, attempts to model the data assuming this simple 1:1 interaction did not succeed, indicating that the interaction must proceed by a different mechanism (the failure of the "direct reaction" model is presented in detail in Appendix 3).The next most logical model for the interaction between Fe-*tpena* and H_2O_2 would require formation of a peroxo complex with Fe^{III}-*tpena* (reaction 4), which may then react with other species, or undergo homolysis to yield Fe^{IV}-*tpena*, $HO^{\bullet}$, or other products, e.g.:

$$Fe^{III}\text{-}tpena + H_2O_2 \rightleftharpoons Fe^{III}\text{-}tpena\text{-}H_2O_2 \quad (4\&5)$$

$$Fe^{III}\text{-}tpena\text{-}H_2O_2 \rightarrow Fe^{IV}\text{-}tpena + HO^{\bullet} \quad (6)$$

$$Fe^{III}\text{-}tpena\text{-}H_2O_2 + H_2O_2 \rightarrow Fe^{IV}\text{-}tpena + O_2^{\bullet-} \quad (7)$$

$$Fe^{III}\text{-}tpena\text{-}H_2O_2 + H_2O_2 \rightarrow Fe^{III}\text{-}tpena + HO^{\bullet} + O_2^{\bullet-} \quad (8)$$

$$Fe^{III}\text{-}tpena\text{-}H_2O_2 + Fe^{III}\text{-}tpena \rightarrow 2\ Fe^{IV}\text{-}tpena + H_2O \quad (9)$$

Such Fe^{III}-peroxo compounds are well-established to form for similar ligands like bztpen (Nebe et al., 2010) (same structure as *tpena*, but the acetate arm is replaced with a benzyl moity) and EDTA (Brausam and van Eldik, 2004). The Fe^{III}-EDTA + H_2O_2

system has also been shown to be able to oxidize substrates, with intermediacy of an Fe^{III}-EDTA-H_2O_2 moiety presumed (Walling et al., 1975). Note that no claims are made about the protonation state of this complex or of the nature of the Fe-peroxide bond (e.g., whether it is an η_1-OOH or η_2-O_2 binding motif) as the current study was conducted at only one pH and without any spectroscopic characterization of the complex. However, that such a complex does form (whatever its protonation or structure) is strongly supported by the precedence of such complexes with other similar ligands and also the inability of other likely reaction paths to account for the experimental observations.

The homolytic breakdown of the peroxo-complex to Fe^{IV}-*tpena* and $HO^{\bullet}$ (reaction 6) is proposed as a key reaction of the peroxo species, as is its reaction with an additional Fe^{III}-*tpena* leading to a simple stoichiometric oxidation without the need for oxygen radical intervention (reaction 9). It is also proposed that the reaction of the peroxo complex with H_2O_2 occurs through two competing pathways. In the dominant pathway, the transition state has Fe^{IV}=O-*tpena*$\cdots^{\bullet}$OH character, reacting similarly to $HO^{\bullet}$ with H_2O_2 and resulting in formation of Fe^{IV}-*tpena* and $O_2^{\bullet-}$ as the reactive products (reaction 7). In the minor pathway, the transition state is considered to have $Fe^{III}(OH)\cdots O(^3P)$ character, reacting with H_2O_2 similarly to $O(^3P)$ (Sauer et al., 1984) to yield Fe^{III}-*tpena*, $HO^{\bullet}$ and $O_2^{\bullet-}$ (reaction 8).

As described above, repeated additions of H_2O_2 result in decreased effectiveness of the complex, presumably due to degradation of the complex. Two pathways have been considered in the model for this degradation. Firstly, the peroxo complex itself may break down directly following the reaction:

$$Fe^{III}\text{-}tpena\text{-}H_2O_2 \rightarrow Fe^{III}\text{-}tpena_{ox} + OH^- \qquad (10)$$

The second possibility is the reaction of $HO^{\bullet}$ with the complex. In this case, there are two possible products; $HO^{\bullet}$ may oxidize the metal centre from Fe^{III} to Fe^{IV} (reaction 11), leaving the ligand intact, or, alternatively, it may oxidize the ligand leading to its alteration and eventual breakdown. The overall rate of the reaction has been estimated from published rates of reaction of $HO^{\bullet}$ with a similar complex, Fe^{III}-DTPA (Cabelli et al., 1989), with $k = 5.0 \times 10^9\ M^{-1}s^{-1}$, with the relative contribution of either metal-centre oxidation or ligand oxidation treated as a fitting parameter in the model. Superoxide is

considered as a product of the ligand oxidation (reaction 12), as it is assumed that the initial ligand radical would rapidly react with O_2 to form the diamagnetic oxidized form (reaction 16&17 in Table 4-2).

$$Fe^{III}\text{-}tpena + HO^{\bullet} \rightarrow Fe^{IV}\text{-}tpena + OH^{-} \quad (11)$$

$$Fe^{III}\text{-}tpena + HO^{\bullet} \rightarrow Fe^{III}\text{-}tpena_{ox} + OH^{-} + O_2^{\bullet -} \quad (12)$$

The kinetic model resulting from this conceputalisation was able to fit the experimental data quite well, including electro-Fe^{IV} decay data (Figure 4-4b/c), H_2O_2 consumption (Figure 4-4a and 4-11), formate degradation (Figure 4-12) and Phth degradation (Figure 4-13) at varied reactant concentrations. Although modelled data do not always exactly reproduce experimental data (such as in Figure 4-4 and 4-11), this model well predicts the trends of substrate degradation, oxidant consumption and even Fe^{IV} decay in all the experiments with Fe-*tpena* and H_2O_2.

Table 4-2 Proposed model for the degradation of formate and Phth by H_2O_2 activated Fe-*tpena* in homogeneous conditions at room temperature

Reaction	k ($M^{-1}\cdot s^{-1}$)	Comment
$\boldsymbol{Fe^{III}tpena + H_2O_2 \rightarrow Fe^{III}tpenaH_2O_2}$ **(4)**	1×10^{5}	Fe-*tpena* activation and deactivation by peroxide along with hydroxyl radicals generation, fitted by experimental data in this work
$\boldsymbol{Fe^{III}tpenaH_2O_2 \rightarrow Fe^{III}tpena + H_2O_2}$ **(5)**	1×10^{5}	
$\boldsymbol{Fe^{III}tpenaH_2O_2 + Fe^{III}tpena \rightarrow 2Fe^{IV}tpena + 2OH^{-}}$ **(9)**	6.5×10^{3}	
$\boldsymbol{Fe^{III}tpenaH_2O_2 + H_2O_2 \rightarrow Fe^{IV}tpena + H^{+} + {}^{\bullet}O_2^{-}}$ **(7)**	4.5×10^{2}	
$\boldsymbol{Fe^{III}tpenaH_2O_2 + H_2O_2 \rightarrow Fe^{III}tpena + H^{+} + {}^{\bullet}O_2^{-} + HO^{\bullet}}$ **(8)**	20	
$\boldsymbol{Fe^{III}tpenaH_2O_2 \rightarrow Fe^{IV}tpena + OH^{\bullet}}$ **(6)**	3×10^{-2}	
$\boldsymbol{Fe^{III}tpenaH_2O_2 \rightarrow Fetpena_{OX} + OH^{-}}$ **(10)**	2×10^{-2}	
$\boldsymbol{Fe^{IV}tpena + H_2O_2 \rightarrow Fe^{III}tpena + {}^{\bullet}O_2^{-}}$ **(13)**	2×10^{2}	
$\boldsymbol{Fe^{IV}tpena + {}^{\bullet}O_2^{-} \rightarrow Fe^{III}tpena + O_2}$ **(14)**	1×10^{6}	

(Continue to next page)

Table 4-2 *(continued)*

Reaction	k ($M^{-1}\cdot s^{-1}$)	Comment
$Fe^{IV}tpena \rightarrow Fe^{III}tpena$ **(15)**	8×10^{-4}	Water oxidation (determined in 3.3.2)
$HO^{\bullet} + Fe^{III}tpena \rightarrow Fe^{IV}tpena + OH^-$ **(11)**	2.5×10^{9}	Fe^{III}-*tpena* activation and activated Fe-*tpena* scavenging by radicals, fitted by experimental data in this work
$HO^{\bullet} + Fe^{III}tpena \rightarrow FetpenaRAD + H_2O$ **(16)**	2.5×10^{9}	
$FetpenaRAD + O_2 \rightarrow FetpenaOX + {}^{\bullet}O_2^-$ **(17)**	2×10^{9}	
$HCOO^- + HO^{\bullet} \rightarrow {}^{\bullet}CO_2^- + H_2O$ **(18)**	3.2×10^{9} [a]	Formate oxidation and reactions triggered; values from references
$Fe^{IV}tpena + HCOO^- \rightarrow Fe^{III}tpena + CO_2 + {}^{\bullet}O_2^-$ **(19)**	1.2 [b]	
${}^{\bullet}CO_2^- + O_2 \rightarrow CO_2 + {}^{\bullet}O_2^-$ **(20)**	2×10^{9} [c]	
${}^{\bullet}CO_2^- + H_2O_2 \rightarrow CO_2 + HO^{\bullet} + OH^-$ **(21)**	7.3×10^{5} [d]	
${}^{\bullet}O_2^- + {}^{\bullet}O_2^- \rightarrow H_2O_2$ **(22)**	3.06×10^{4} [e]	Radicals / H_2O_2 reactions
$HO^{\bullet} + H_2O_2 \rightarrow HO_2^{\bullet}$ **(23)**	2.7×10^{7} [f]	
$Phth + Fe^{IV}tpena \rightarrow Fe^{III}tpena + PhthOx + {}^{\bullet}O_2^-$ **(24)**	225	Phth/Phth-OH oxidations; k values for reactions with Fe-*tpena* are fitted from experimental data
$PhthOH + Fe^{IV}tpena \rightarrow Fe^{III}tpena + PhthOx + {}^{\bullet}O_2^-$ **(25)**	750	
$HO^{\bullet} + Phth \rightarrow PhthOH + {}^{\bullet}O_2^-$ **(26)**	5.3×10^{9} [g]	
$HO^{\bullet} + PhthOH \rightarrow PhthOx + {}^{\bullet}O_2^-$ **(27)**	5.3×10^{9} [h]	

[a] Kwan and Voelker (2002) [b] de Sousa et al (2017); [c] Neta et al. (1988) review, value for pH 8; [d] Unknown products, from Neta et al (1988) review [e] Overall rate at pH 8.3 from Bielski et al. (1985); [f] Buxton et al. (1988); [g] Schiller et al. (1999); [h] assumed value from Miller et al. (2011).

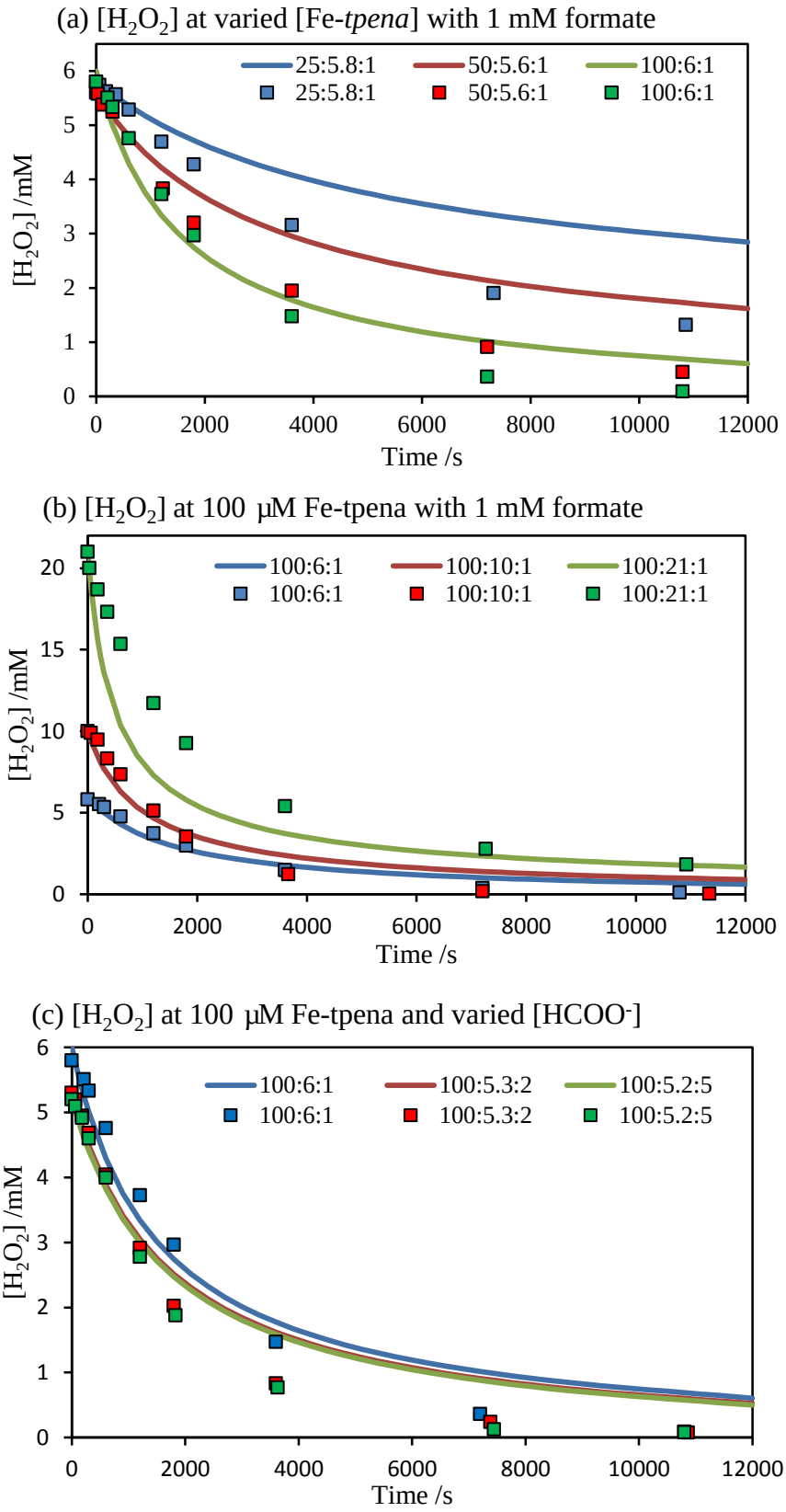

Figure 4-11 Experimental (squares) and modelled (lines) time-trace data of hydrogen peroxide concentration at different *Fe-tpena (*µM per Fe*) : peroxide(mM) : formate* (mM) ratios at pH 8

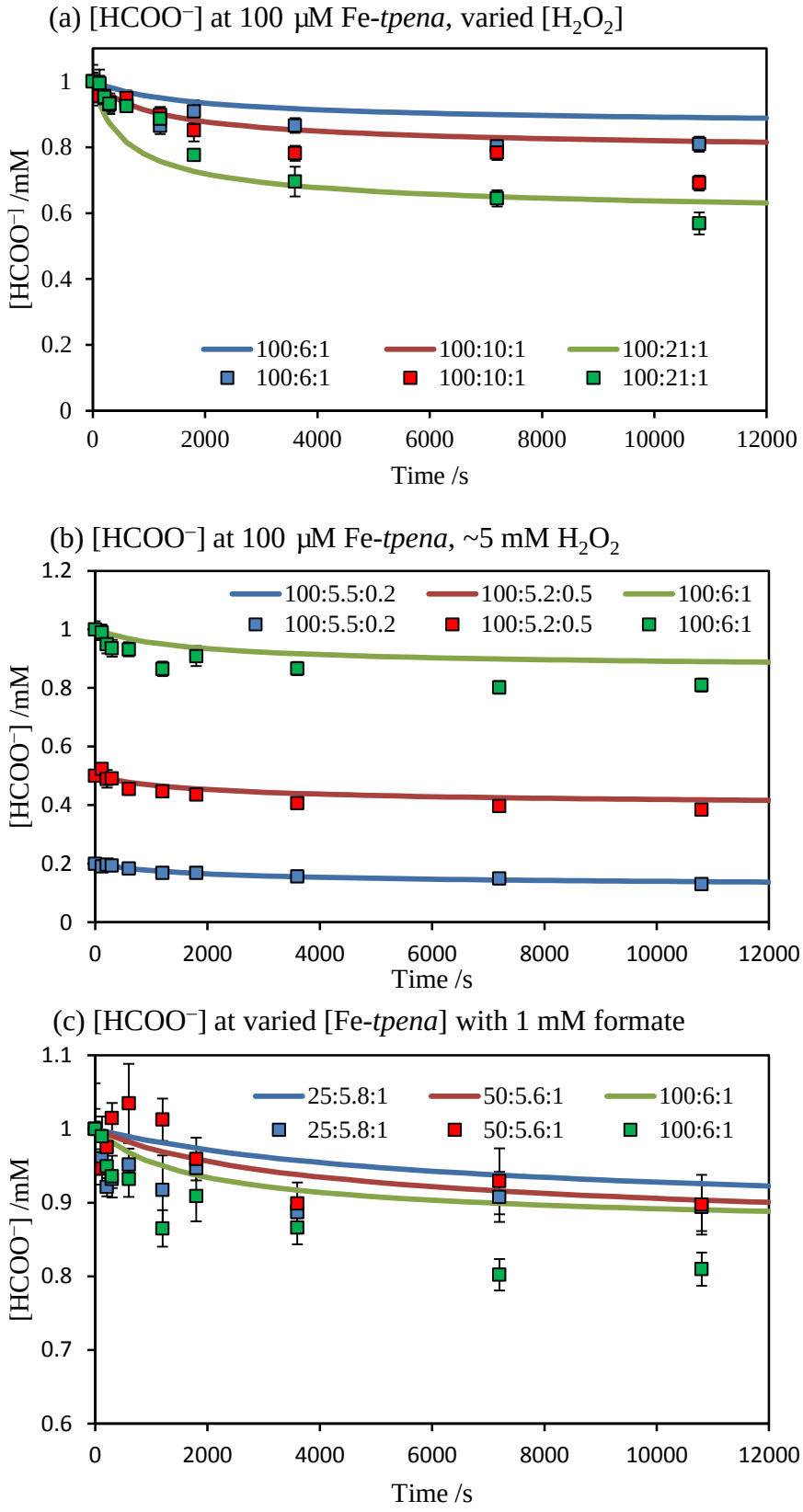

Figure 4-12 Experimental (squares) and modelled (lines) time-trace data of formate concentration at different *Fe-tpena (*µM per Fe*) : peroxide(mM) : formate* (mM) ratios at pH 8

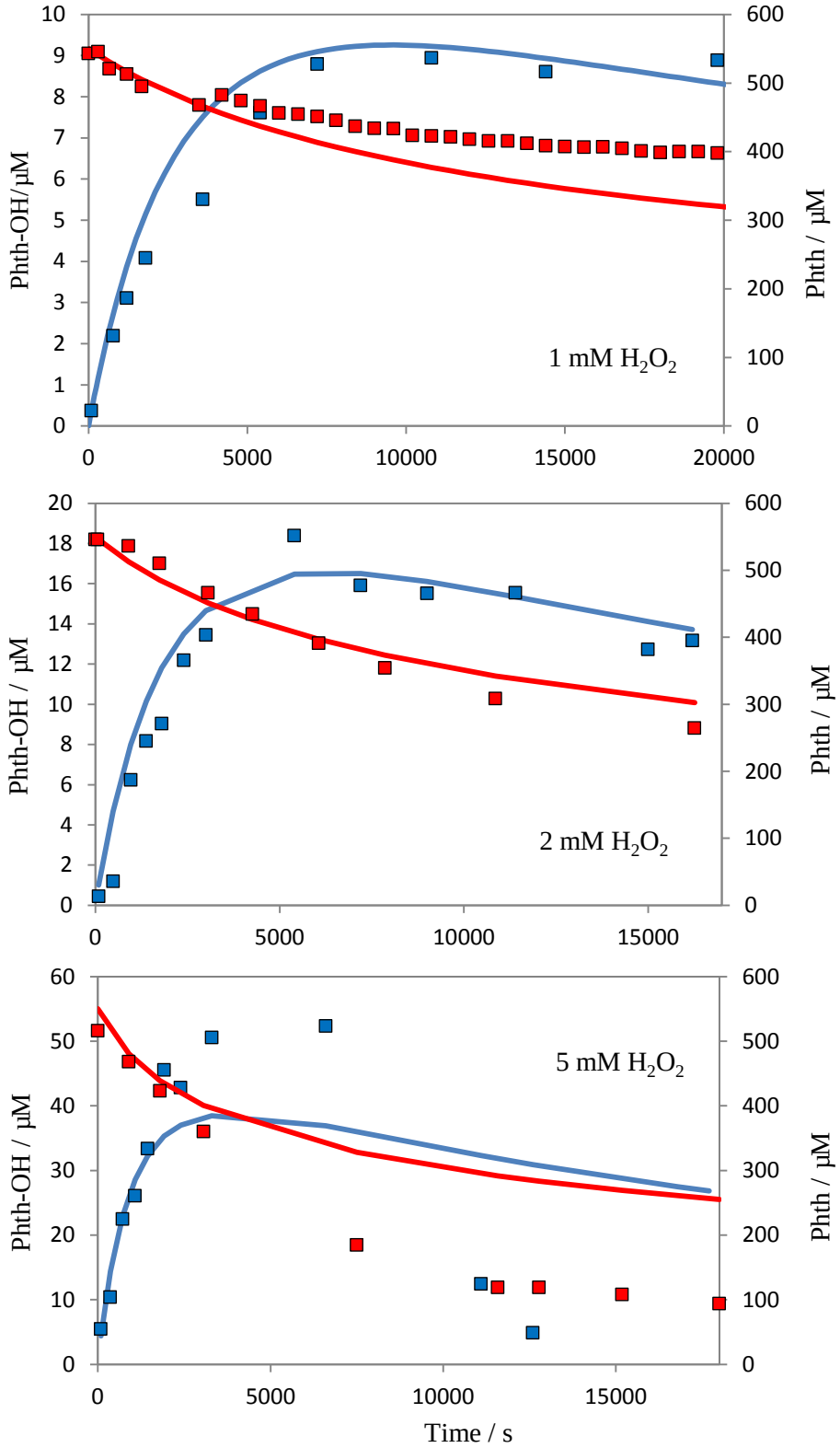

Figure 4-13 Experimental (squares) and modelled (lines) time-trace of Phth (red) and Phth-OH (blue) concentrations when different amount of H_2O_2 is added to 100 µM Fe-*tpena* (per Fe) and 550 µM Phth at pH 8.

In order to obtain a better understanding of active oxidants in Fe-*tpena*/H_2O_2 system, a system with 100 μM (per Fe) Fe-*tpena*, 5mM H_2O_2 and 1mM (or 0 mM) formate was modelled enabling examination of the change in $Fe^{III/IV}$-*tpena* and $HO^{\bullet}$ concentrations as shown in Figure 4-14.

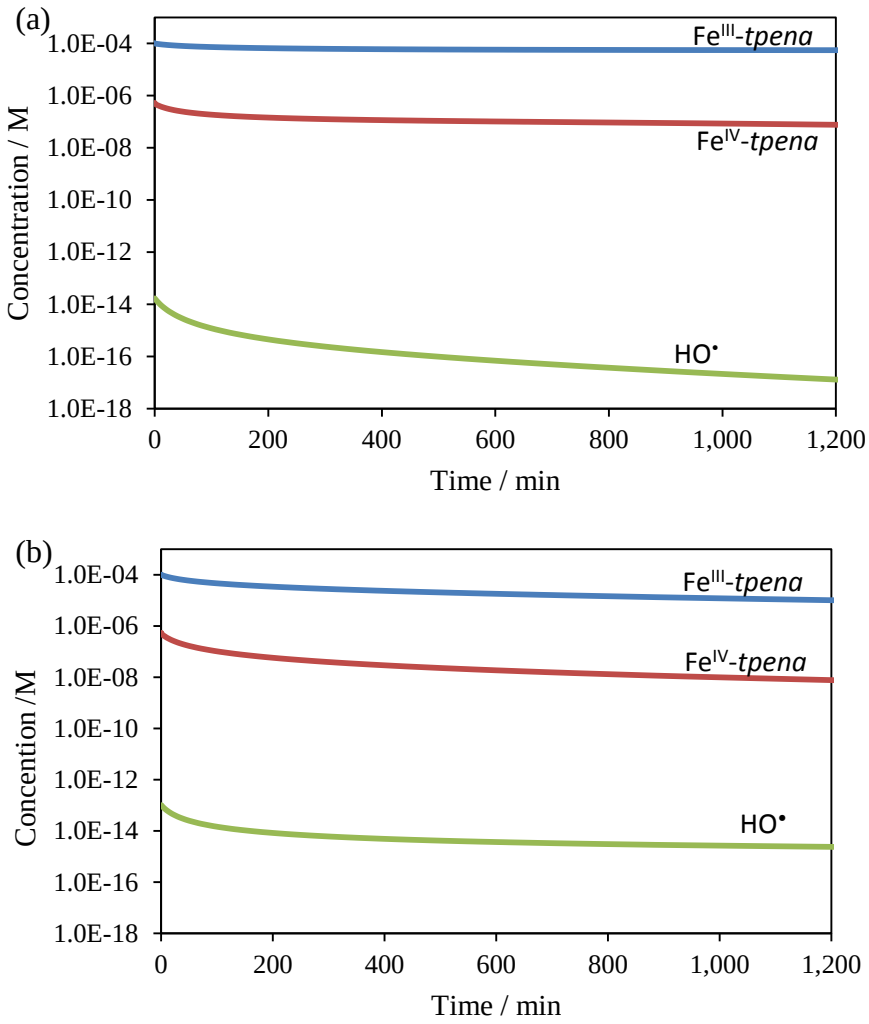

Figure 4-14 Modelled $Fe^{III/IV}$-*tpena* and $HO^{\bullet}$ concentrations varying with time in a system starting at 100 μM Fe^{III} –*tpena* and 5 mM H_2O_2 (a) with 1 mM formate, and (b) with no substrate at pH 8.

In the modelled data, the hydroxyl radical concentration is initially ~10^7 times lower than that of Fe^{IV}-*tpena* and is consumed more rapidly than Fe^{IV}-*tpena* in the presence of

formate. Fe^{IV}-*tpena* of 10^{-6} M is undetectable through UV-vis, which is consist with observations in the experiment. The presence of formate in the system can help protect Fe-*tpena* by consuming $HO^{\bullet}$, otherwise, Fe-*tpena* will be consumed as twice. Taking the second order rate constants for formate oxidation by hydroxyl radicals (3.2×10^9 $M^{-1}s^{-1}$) and Fe^{IV}-*tpena* (1.2 $M^{-1}s^{-1}$) into account, formate degradation by hydroxyl radicals is contributing a lot, especially in the first 3 hours before $HO^{\bullet}$ concentration drops to less than 10^{-9} of [Fe^{IV}-*tpena*]. This behaviour differs from that of Phth because the rate constant for Phth oxidation by Fe^{IV}-*tpena* and $HO^{\bullet}$ is 250 $M^{-1}s^{-1}$ (~2×10^2 higher than formate) and 5.3×10^9 $M^{-1}s^{-1}$ (similar with formate) relatively, and thus the contribution of Fe^{IV}-*tpena* to Phth oxidation is likely to be greater than that of $HO^{\bullet}$, particularly in view of the relatively stable concentration of Fe^{IV}-*tpena*.

Although $HO^{\bullet}$ generation is typically considered a positive result for an oxidant generating system, under the conditions of this study it also led to significant destruction of the Fe-*tpena* complex and was thus an undesirable outcome. However, if the concentration of the substrate is high enough, and the Fe-*tpena* concentration low enough, this issue would not manifest as severely and the $HO^{\bullet}$ may serve mostly to oxidize the substrate.

4.3.6 RhB degradation by peroxide/iron-*tpena* system

The degradation of RhB by the Fe-*tpena* + H_2O_2 system was examined as an example application of complex organic compound degradation. As the ligand is found to be stable in the NaCl (10 mM) $NaHCO_3$ (2 mM) matrix (as discussed in 4.3.2), it is used throughout this section to mimic ambient aqueous conditions. Due to its complexity, the detailed kinetics of rhodamine degradation are not amenable to detailed kinetic analysis, and none has been attempted. However, qualitative interpretation is possible due to the ability to readily estimate concentrations of several of the chromophoric degradation by-products of rhodamine. The impact of different RhB (2~10 μM), Fe-*tpena* (50~200 μM), and hydrogen peroxide (1~5 mM) concentrations was examined. The peroxide and Fe compound loadings used for Fe-*tpena* are much higher compared to the Fe-TAML homogeneous study in section 2.2.3, because Fe-*tpena*/H_2O_2 at the same Fe-*tpena*/ H_2O_2

loading and H_2O_2 addition method yield less than 30% RhB decrease after 4 hours (data not shown). This is probably due to ligand decomposition by $HO^{\bullet}$.

RhB addition to a buffer solution containing a high loading of Fe-*tpena*/H_2O_2 shows an instant spectra change lasting over 3 hours with decreasing absorbance at 554 nm (vertical line) and a slight peak shift to lower wavelength, indicating generation of other rhodamine species (an example is shown in Figure 4-15a). Deconvolution of the spectra gives information of Rhodamine speciation as show in Figure 4-15b.

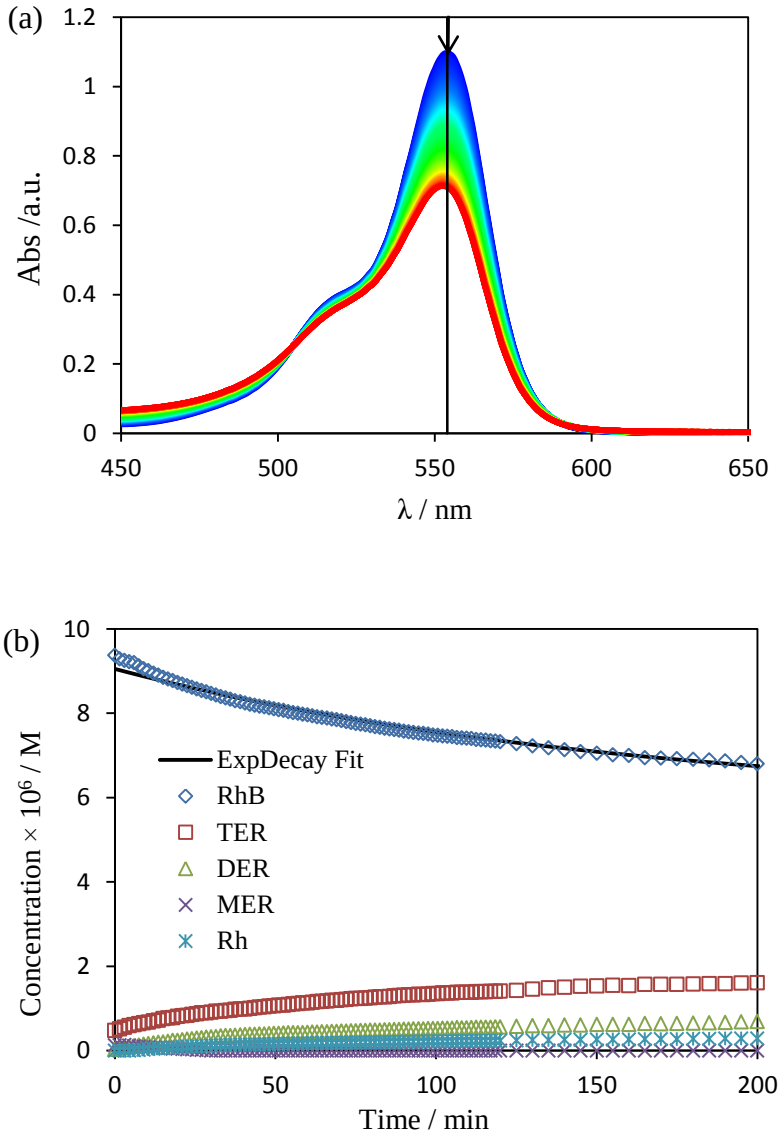

Figure 4-15. (a) UV-vis spectra and (b) time trace for rhodamine species of the RhB degradation by 1 mM H_2O_2 and 50 μM Fe-*tpena* at pH 8 and the exponential fit to extract the obvious rate constant for RhB decrease. Initial RhB: 10 μM.

An exponential decay function can be fitted to the time trace of RhB concentration (see the solid line in Figure 4-15b) enabling extraction of a pseudo-first order rate constant (k') where $k' = \sum k_i[(\text{active oxidant})_i]$ (k_i is the second rate constant for active oxidant ***i*** which could be Fe^{IV}-*tpena* or $HO^{\bullet}$). Since the second-order rate constant for rhodamine B degradation by hydroxyl radicals (9×10^9 $M^{-1}s^{-1}$ (Buxton et al., 1988)) and Fe^{IV}-*tpena* (60 ± 24 $M^{-1}s^{-1}$ from Section 3.3.4) are both known, assuming an extreme condition where only one oxidant is contributing to RhB oxidation allows the calculation of the maximum potential concentration of the oxidant. Table 4-3 shows the k', $[Fe^{IV}\text{-}tpena]_{max}$ and $[HO^{\bullet}]_{max}$ for different initial RhB loadings, H_2O_2 loadings and Fe-*tpena* loadings. The calculated $[Fe^{IV}\text{-}tpena]_{max}$ and $[HO^{\bullet}]_{max}$ are generally consistent with the above modelling results. Looking at the observed rate constant for RhB degradation, k', it is positively related to the initial Fe-*tpena* concentration and is approximately 2×10^{-4} s^{-1} when $[\text{Fe-}tpena]_0$ is 100 μM with only one exception of 3×10^{-4} s^{-1} when $[H_2O_2]_0$ is 5 mM. This is because: 1) the concentration of Fe^{IV}-*tpena*, which is likely to be the dominant active oxidant at low $[H_2O_2]_0$ (1 and 2 mM), is closely related to $[\text{Fe-}tpena]_0$ and can be protected by rhodamine species from $HO^{\bullet}$ attack, and 2) $[H_2O_2]_0$ positively affects $HO^{\bullet}$ generation though $[Fe^{IV}\text{-}tpena]$ can vary to some extent so, in the 5mM $[H_2O_2]_0$ case, $HO^{\bullet}$ is probably at a concentration high enough that its contribution to RhB degradation is significant. Overall, the initial loading of 1mM H_2O_2 and 200 μM Fe-*tpena* gives the fastest RhB decrease in the range studied; however, other rhodamine species need to be taken into account when pursuing total decolourisation of the dye.

Table 4-3 Pseudo-first order rate constants (*k'*) for RhB degradation at various RhB, H_2O_2 and Fe-*tpena* loadings

$[H_2O_2]_0$ /mM	$[RhB]_0$ / μM	$[\text{Fe-}tpena]_0$ (per Fe) / μM	*k'*/s	$[Fe^{IV}\text{-}tpena]_{max}$ (per Fe) /M	$[HO^{\bullet}]_{max}$ /M
1	2	100	1.5×10^{-4}	2.5×10^{-6}	2.8×10^{-14}
1	5	100	2.2×10^{-4}	3.7×10^{-6}	4.2×10^{-14}
1	10	100	1.9×10^{-4}	3.1×10^{-6}	3.6×10^{-14}
1	10	50	1.0×10^{-4}	1.7×10^{-6}	2.0×10^{-14}
1	10	200	3.9×10^{-4}	6.5×10^{-6}	7.3×10^{-14}
2	10	100	1.9×10^{-4}	3.2×10^{-6}	3.6×10^{-14}
5	10	100	2.8×10^{-4}	4.6×10^{-6}	5.3×10^{-14}

As for other rhodamine species, their generation can be attributed solely to action by Fe^{IV}-*tpena* because RhB degradation by $HO^{\bullet}$ is mainly through a chromopore cleavage mechanism and would not be expected to result in formation of any deethylation products as established in a few studies (Nidheesh and Rajan, 2016, Gazi et al., 2010, Li et al., 2011, Sheng et al., 2018). Despite this, the reactions involved in the Fe-*tpena*/H_2O_2 system are still quite complicated due to the many potential RhB degradation pathways as illustrated in Figure 4-16, requiring a large number of rate constants to be estimated and thus making it challenging to develop a robust kinetic model. To better compare these data including other rhodamine species' generation, a simplified quantification of the overall degradation of RhB is developed below.

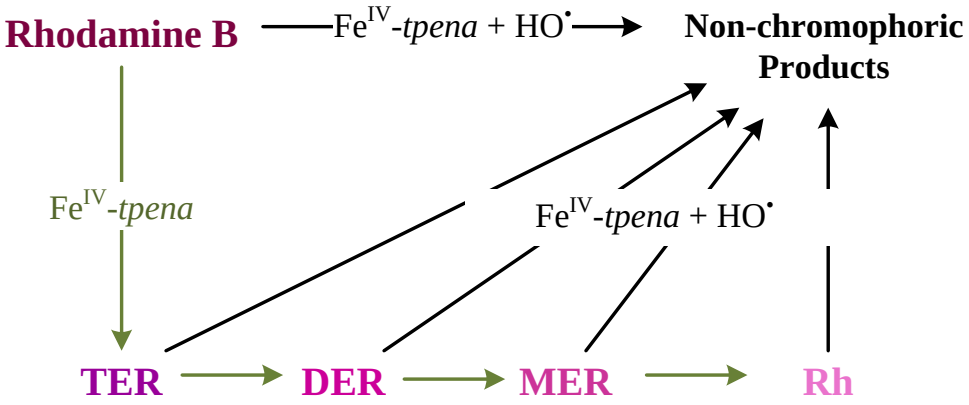

Figure 4-16 Rhodamine B degradation pathways in the Fe-*tpena*/H_2O_2 system

The overall degradation of RhB involves both deethylation and decolourization. Deethylation can be quantified by calculating the number of ethyl groups lost from rhodamine species (*nde* = [TER]+2[DER]+3[MER]+4[Rh]). Decolourization can be quantified by the decrease of total rhodamine species ($\Delta\sum Rh$) however this can occur at any time during the deethylation process and, a such, will cause an under-estimation of the actual *nde* value since all the deethylation steps may not be quantified before the final decolourization. To compensate for this under-estimation, a factor of three was introduced into the decolourization part in this study, representing the average number of oxidation reactions have happened to degrade a RhB molecule to non-chromophoric

products from which takes 2-5 steps (assuming those non-chromophoric products cannot be further be degraded) as demonstrated in figure 4-16. After scaling to the initial concentration of [RhB] ($[RhB]_0$), an equation as shown below is used to indicate the extent of RhB degradation:

$$\frac{nde + 3\Delta\sum Rh}{[\mathrm{RhB}]_0} = \frac{[([\mathrm{TER}] + 2[\mathrm{DER}] + 3[\mathrm{MER}] + 4[\mathrm{Rh}]) + 3(\sum Rh_0 - \sum Rh)]}{[\mathrm{RhB}]_0}$$

For different H_2O_2 concentrations, as shown in Figure 4-17, higher concentrations of H_2O_2 led to more rapid and more extensive degradation. Despite the fact that Fe^{IV}-*tpena* generation may vary in the H_2O_2 loading range, 5mM H_2O_2 yielded nearly complete degradation of RhB with $(nde + 3\Delta\sum Rh)/[RhB]_0 \approx 3$ (where the index of 3 means a complete degradation of RhB with no rhodamine species left) where the contribution from $HO^{\bullet}$ is likely to be important.

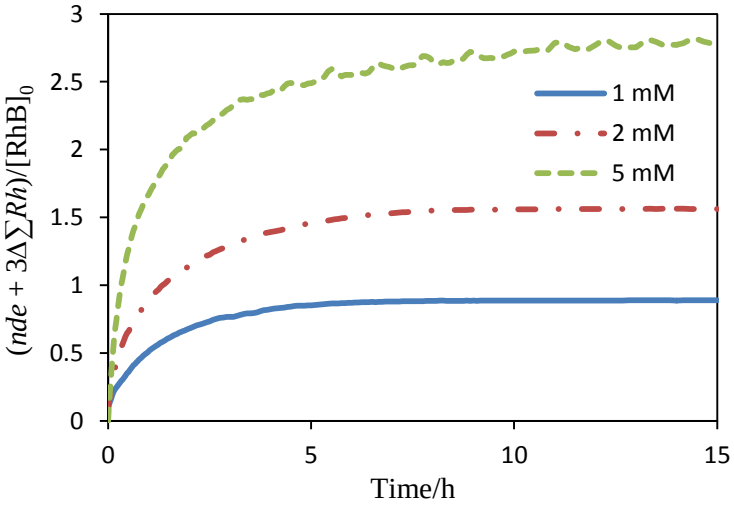

Figure 4-17 RhB degradation by in H_2O_2/Fe-*tpena* system with different H_2O_2 (1, 2 and 5 mM). Initial Rhodamine B loading: 10 μM; Fe-*tpena*: 100 μM; pH 8.

As can be seen from Figure 4-18, higher Fe-*tpena* concentration appears to lead to a faster reaction at first but not necessarily greater overall degradation. This result is to be expected since Fe-*tpena*, when present at high enough concentrations (as in the 200 μM

Fe-*tpena* /1 mM H_2O_2 case), will compete with substrates for $HO^{\bullet}$ and thus is both degraded to inactive, oxidized complexes as well as preventing the $HO^{\bullet}$ that is formed from reacting with rhodamine. In the range investigated, 100 μM Fe-*tpena* (H_2O_2/Fe-*tpena* = 10, Fe-*tpena*/RhB = 10) gives the best degradation, compared to the 50 μM and 200 μM Fe-*tpena* case.

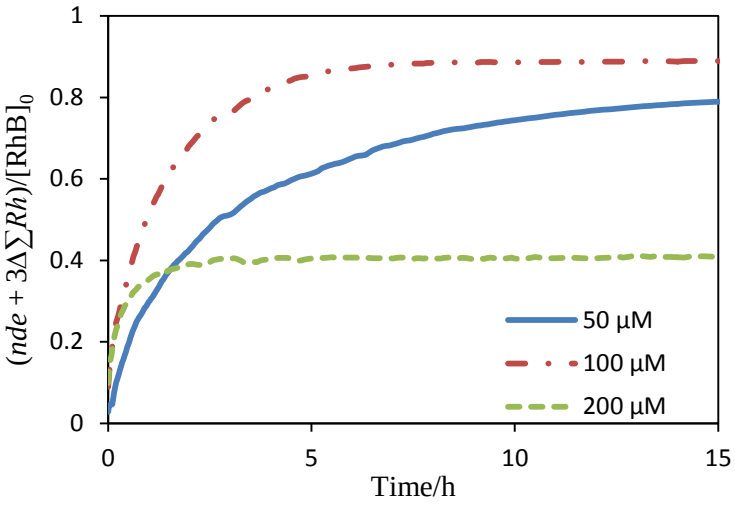

Figure 4-18 RhB degradation by H_2O_2 activated Fe-*tpena* with 10 μM RhB, 1 mM H_2O_2 and different concentrations of Fe-*tpena* (50, 100 and 200 μM) at pH 8.

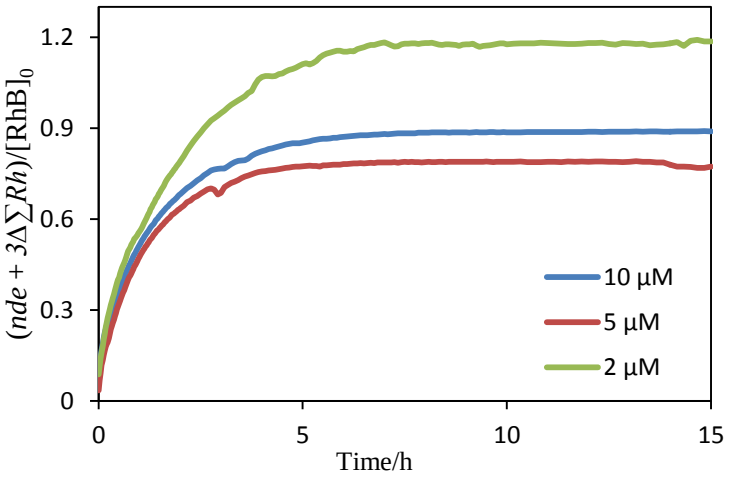

Figure 4-19 RhB degradation by H_2O_2 activated Fe-*tpena* with 1 mM H_2O_2, 100 μM Fe-*tpena* and different RhB loadings (2, 5 and 10 μM) at pH 8.

As for initial RhB concentration, it does not affect the degradation significantly, although a small impact is observed. This is probably because the substrates affect the concentrations of both hydroxyl radicals and Fe^{IV}-*tpena* by competing for these oxidants. Nevertheless, different RhB loadings end up with similar degradation rates and $(nde + 3\Delta\sum Rh)/[RhB]_0$ values ranging from 0.8 to 1.2 (Figure 4-19).

As the rate constants for reaction of RhB with both $HO^{\bullet}$ and Fe^{IV}-*tpena* are known, an estimate of the relative importance of each oxidant can be deduced. Using rate constants for reaction of RhB with Fe^{IV}-*tpena* and $HO^{\bullet}$ of 60 $M^{-1}s^{-1}$ and 9×10^9 $M^{-1}s^{-1}$, respectively combined with the oxidant concentration estimates derived from the model in Figure 4-14b suggests that $HO^{\bullet}$ is responsible for >90% of the observed RhB oxidation.

4.4 Conclusion

It has been demonstrated in this chapter that Fe-*tpena* is able to catalytically degrade H_2O_2 with concomitant formation of both Fe^{IV}-*tpena* and $HO^{\bullet}$.

A kinetic model that well explains the experimental data was developed based on the hypothesis that Fe-*tpena* interacts with H_2O_2 through an initial precursor complex with multiple potential decay pathways, only one of which is homolysis to Fe^{IV}-*tpena* and $HO^{\bullet}$. The generation of $HO^{\bullet}$ results in significant damage to the Fe-*tpena* complex and eventually inactivates it.

In such a system, the best scenario is when the substrate outcompetes Fe-*tpena* for $HO^{\bullet}$, which would result in both substrate degradation and longer lasting Fe-*tpena* for ongoing oxidant generation.

Despite the above issues, Fe-*tpena*/H_2O_2 could still achieve ~40% formate degradation and complete decolourisation of RhB solution. Future work exploring methods that can minimize ligand decomposition in this system, as well as better harness the generated $HO^{\bullet}$ for desired reactions would appear beneficial. The demonstration of the production of both a high-valent iron-oxo species and $HO^{\bullet}$ under mild, ambient conditions without

any energy input respresents a significant contribution to current advanced oxidation processes.

Chapter 5.
Chemical activation of Fe-*tpena* by hypochlorite

5.1 Introduction

Besides electrochemical activation and activation via reaction with hydrogen peroxide, other oxidants could also be used for activating Fe-*tpena*. Of particular interest is use of sodium hypochlorite, a chemical that is used extensively in water and wastewater treatment. It has been used as an alternative to H_2O_2 in the Fenton process because of its lower cost and better resilience to pH change (Behin et al., 2017). Being a powerful oxidising regent itself and with the more active hypochlorous acid (HClO) generated in water, introducing Fe-*tpena* could enhance its efficacy in degrading recalcitrant contaminants providing Fe^{IV}-*tpena* can be produced.

The Fe^{IV} intermediate can be generated in organic solution in the presence of hypochlorite and certain Fe-complexes. Balland et al. (2004) reported formation of a mononuclear Fe^{IV} species upon reaction of NaClO with non-porphyrinic Fe^{II} complexes in methanol at low temperature. Draksharapu et al. (2015) has also identified formation of Fe^{IV} species through a Fe^{III}-OCl pathway during the reaction between $[Fe^{II}(OH_2)(MeN_4Py)]^{2+}$ and NaClO (MeN_4Py = 1,1-di(pyridin-2-yl)-N,N-bis(pyridin-2-ylmethyl)ethanamine). However, hypochlorite activation is seldom used for biomimetic Fe-based complexes in aqueous conditions though its use in activating Fe-TAML has been recently described (Mills et al., 2016). Compared to the 1st-generation TAMLexamined in Chapter 2, the new (third generation) TAML ligand does not have an aromatic ring eith this feature allowing $Fe^{IV/V}$-TAML to be generated via reaction with NaClO in water at pH 2~13 (13 ℃) (Mills et al., 2016).

In this chapter, HClO/ClO^- will be added to a Fe-*tpena* solution at pH 8 for Fe^{IV}-*tpena* generation and formate used as a probe to explore their synergistic activity as oxidants compared to formate oxidation by NaClO alone. Rhodamine B (RhB) is not used as a probe for the Fe^{IV}-*tpena*/NaClO system because RhB has been found to react rapidly with hypochlorite (Tiong and Price, 2012). The probe compound phthalhydrazide cannot be used to examine the rate and extent of hydroxyl radical in the system either,as it is sensitive to NaClO solution (Appendix 4).

5.2 Materials and methods

5.2.1 Solution preparation

A ~200 mM ClO^- stock solution was prepared by diluting a reagent grade sodium hypochlorite solution (from Sigma–Aldrich) in mQ water. The actual ClO^- concentration was checked by UV-vis spectra each time before use.

10 mM NaCl with 2 mM $NaHCO_3$ equilibrated with ambient air (pH ≈ 8) is used as the matrix for all the Fe-*tpena*/ClO^- experiment unless specified. All solutions were prepared in 18 MΩ.cm Milli-Q water (mQ) obtained from a Millipore Milli-Q system.

5.2.2 Study of ClO^--Fe-*tpena* interaction

A certain amount of ClO^- stock solution was added to a Fe^{III}-*tpena* mQ solution in a 1cm quartz cuvette and Fe^{IV}-*tpena* generation monitored by UV/vis spectroscopy using the Agilent 8453 spectrometer. In some cases (high ClO^- dose), a portion of the stock solution was diluted to ~50 mM and adjusted to ~pH 8 (using $HClO_4$) for immediate use (actual HClO/ClO^- concentration was checked by UV-vis where the relative standard deviation (RSD) is less than 1.5%; details are provided in 5.2.4) to minimize pH shift in the pH 8 matrix.

ClO^- (from 200 mM NaClO stock solution) was also added to electro-generated Fe^{IV}-*tpena* solution (0.8 mM per iron, native pH ~3, in 0.1 M $NaClO_4$, as prepared in 3.3.2) to monitor decay of Fe^{IV}-*tpena* in the presence of HClO/ClO^-, pH was measured before/after ClO^- addition using a HORIBA F-51pH meter.

5.2.3 Formate degradation experiment

Formate was employed as the target substrate in the hypochlorite/Fe-*tpena* system. In a similar manner to that described in Chapter 4, HCOONa (from a 200 mM HCOONa stock solution) and $H^{14}COONa$ (45 nM from a 10 µM stock solution) were mixed with Fe^{III}-*tpena* (from a 2 mM per Fe mQ stock solution) in the pH8 matrix with the timer commenced upon ClO^- addition (pH of the ClO^- stock solution used was adjusted to ~pH 8 immediately before use). Samples (0.2 mL) were taken at desired time points (with one taken prior to ClO^- addition) and quenched with 1 M formic acid (1.8 mL). ^{14}C-labelled formate in the sample was then measured using an Ultima Gold scintillation cocktail (PerkinElmer) and a PerkinElmer Tri-Carb 2910TR liquid scintillation analyzer after $^{14}CO_2$ was liberated from the acidified sample by aeration (10 min). The activity of the sample was subsequently converted to concentration thereby enabling change in formate concentration through the reaction period to be determined. In most cases, ClO^- addition was repeated after the previous reaction had concluded.

5.2.4 Data analysis

To calculate HClO/ClO concentration from the UV spectra, 8 points of the UV spectrum were used including three points from near maximum absorbance of HClO (230, 235 and 240 nm) and five points from near maximum absorbance of ClO^- (280, 285, 290, 295 and 300 nm) as shown in Figure 5-1. Concentrations of HClO and ClO^- were then calculated as follows (similar to the calculation of $[H_2O_2]$ described in 2.2.5):

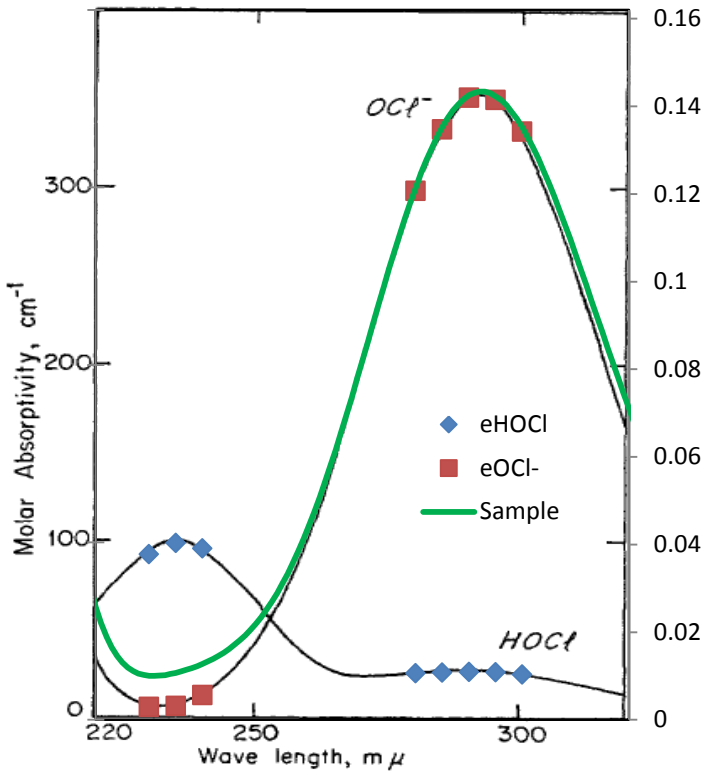

Figure 5-1 A sample UV spectrum (green) and molar absorbance of HClO (red squares) and ClO^- (blue diamonds) (Morris, 1966) at selected wavelengths for data analysis.

$$\begin{bmatrix} A_{230} \\ \vdots \\ A_{300} \end{bmatrix} = \begin{bmatrix} \varepsilon_{230}^{HOCl} & \varepsilon_{230}^{ClO^-} \\ \vdots & \vdots \\ \varepsilon_{300}^{HOCl} & \varepsilon_{300}^{ClO^-} \end{bmatrix} \begin{bmatrix} [HOCl] \\ [ClO^-] \end{bmatrix}$$

$$A = BC$$

$$C = (A^T A)^{-1} A^{-1} B$$

The NaClO concentrations in this chapter refer to the total concentration of HClO and ClO^-.

Exponential decay fits for formate degradation were conducted using SigmaPlot *v.*12.5. Numerical kinetic modelling of the complex reaction schemes was implemented using Kintecus v. 5.20 (Ianni, James C., Kintecus, www.kintecus.com).

5.3 Results and discussion

5.3.1 Fe^{IV}-*tpena* generation and decay on introduction of hypochlorite

Upon the introduction of hypochlorite into a Fe^{III}-*tpena* solution, fast generation of Fe^{IV}-*tpena* is evident from the UV/vis spectra at various NaClO/Fe-*tpena* concentrations (the NaClO/Fe-*tpena* ratio ranged from 5~50), followed by a slow Fe^{IV}-*tpena* decrease (Abs 730 nm) (Figure 5-2). The observable generation of Fe^{IV}-*tpena*, which cannot be achieved in the Fe-*tpena*/H_2O_2 system, shows that Fe^{IV}-*tpena* can be stabilized at a concentration on the order of 10 μM (calculated from the molar absorbance of Fe^{IV}-*tpena*, 256.5 $M^{-1}cm^{-1}$) for more than one hour, especially in the 1 mM NaClO/100 μM Fe-*tpena* case (red line in Figure 5-2b). As a result, substrate degradation efficiency by Fe^{IV}-*tpena* should be significantly improved in the Fe-*tpena*/ClO^- system, though excessive ClO^- /HClO appears to accelerate Fe^{IV}-*tpena* consumption to some extent.

Along with Fe^{IV}-*tpena* generation and decay, a decrease of UV absorbance at around 300 ~ 400 nm was observed in all cases as shown in Figure 5-2a. After the NaClO-Fe-*tpena* reaction, repeat additions of NaClO do not yield any more observable Fe^{IV}-*tpena* generation with this result indicating that Fe-*tpena* is consumed during the course of the reaction. Particular observations suggest that Fe-*tpena* consumption is related to to iron extraction from the ligand: firstly, the decreasing broad absorbance at 300 ~400 nm is consistent with the difference in UV-vis spectra between Na-*tpena* and Fe-*tpena* (shown in Figure 5-3) and, secondly, a yellowish suspension (most likely iron(III) oxyhydroxide precipitate) was observed in the reactor.

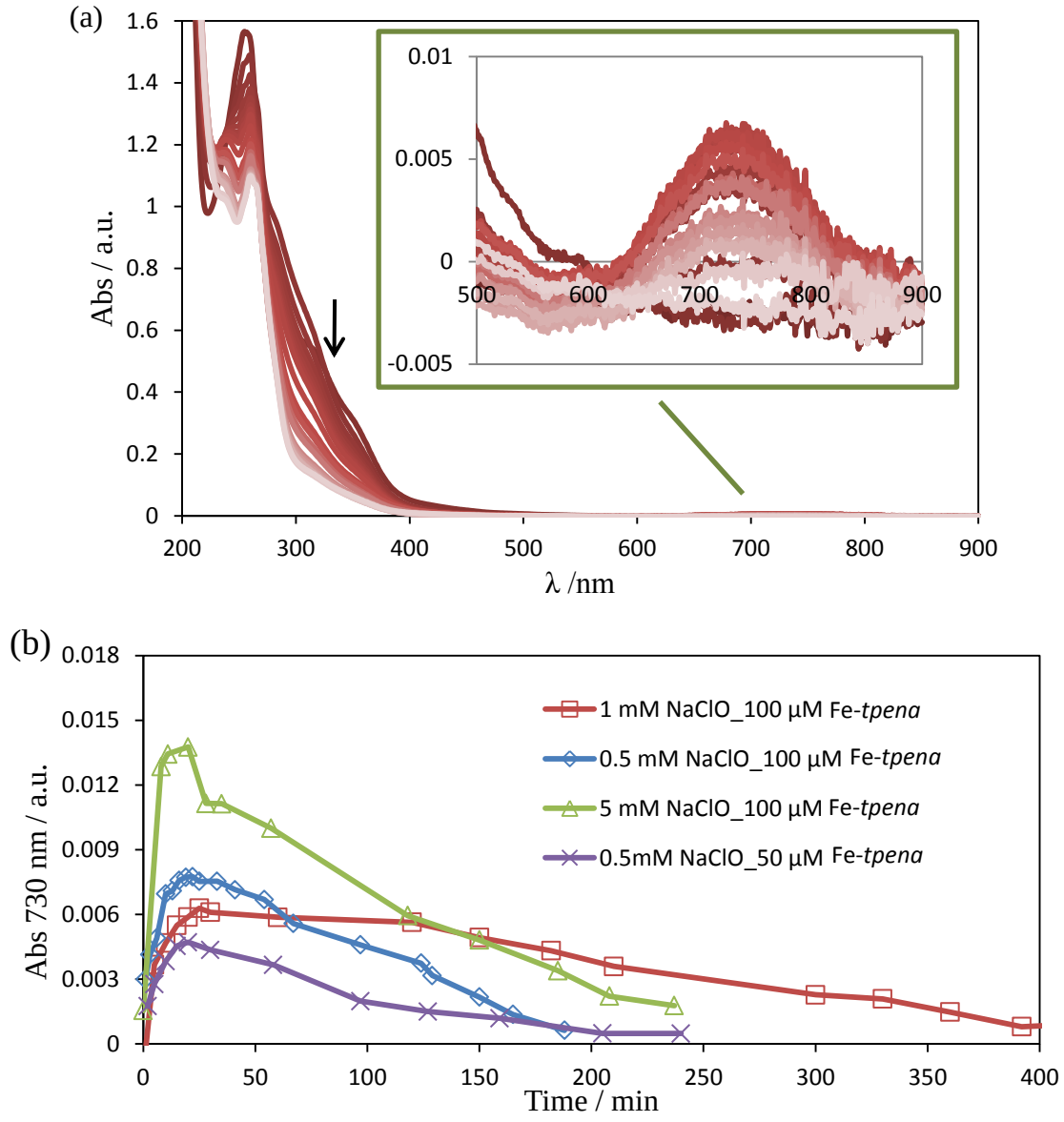

Figure 5-2. (a) Time-resolved UV-vis spectra of 100 µM Fe-*tpena* (per Fe) pH 8 solution after the addition of 1 mM NaClO; (b) Variation of absorbance at 730 nm (representing Fe^{IV}-*tpena*) with time when NaClO (0.5, 1, 2, and 5 mM) was added to Fe-*tpena* (50 and 100 µM per Fe) solution at pH 8

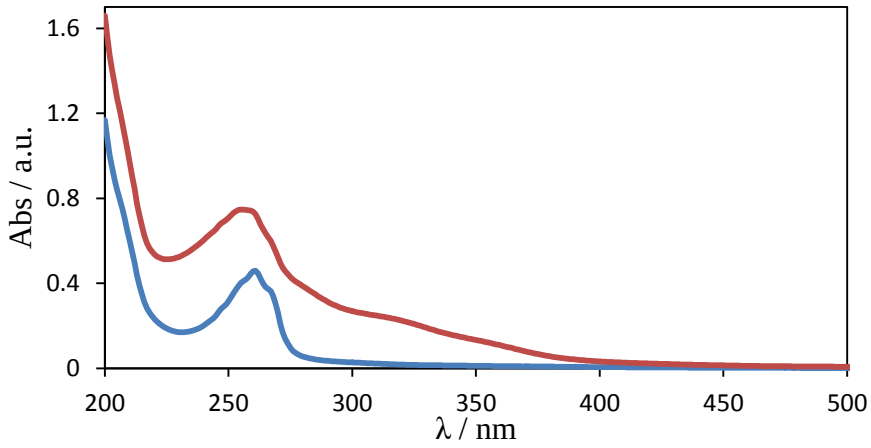

Figure 5-3 UV-vis spectra of 50 μM Na-*tpena* (blue) and 50 μM (per Fe) Fe-*tpena* (red) in the pH 8 matrix.

As shown in Figure 5-4, when NaClO (2, 3 and 5 mM) is added to an electro-generated Fe^{IV}-*tpena* solution (Fe^{III}-*tpena* ~700 μM, final pH 3.6~4), the initial reaction rate (d[Fe^{IV}-*tpena*]/dt) is increasing with NaClO loading where the NaClO/Fe^{III}-*tpena* ratio ranges from ~3 to ~7 (though in this case over 99.95% of NaClO has been converted to HClO given a pK_a = 7.537 at 25 ℃). Introducing NaClO to Fe^{IV}-*tpena* solution could add more Fe^{IV}-*tpena* if the ratio of NaClO/Fe^{III}-*tpena* is high enough (~4). A faster Fe^{IV}-*tpena* decay is also noted for higher NaClO loading at the later stages of the reactions.

Based on above data at pH 8 and ~pH 4, Fe^{IV} generation/degradation does not show very clear correlations with NaClO or Fe-*tpena*. Reactions between HClO/ClO^- and Fe-*tpena* are complex, possibly including but not limited to:1) Fe^{IV}-*tpena* activation by ClO^- species, 2) consumption of Fe^{IV}-*tpena* by ClO^- species and/or intermediate species, and 3) Fe-*tpena* – ClO^- combination via multi pathways.

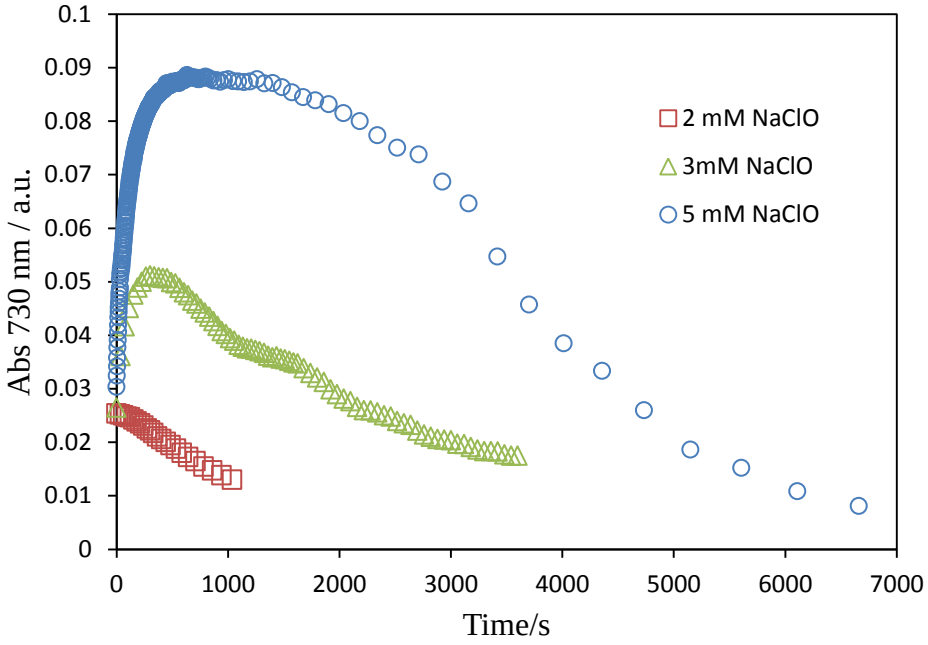

Figure 5-4. Variation of absorbance at 730 nm (representing Fe^{IV}-*tpena*) with time when NaClO (2, 3 and 5 mM, adjusted to pH 8) is added to Fe^{IV}-*tpena*/Fe^{III}-*tpena* (800 µM per Fe with ~ 100 µM initial Fe^{IV}-*tpena*) solution at a final pH of ~4,

5.3.2 Fe^{IV}-*tpena* dynamics in the presence of formate

As observed in the previous section, there is some evidence that the Fe-*tpena* complex is eventually degraded on addition of ClO^-. It is likely that formation of some strong oxidant, such as $HO^\bullet$, $Cl^\bullet$ or $Cl_2^{\bullet-}$ is responsible for this ligand destruction, not the ClO^- itself. Experiments were performed in the presence of formate, both to examine the oxidation of this substrate and also to enable investigation of the Fe-*tpena* – ClO^- interaction under conditions where the complex degradation is minimized, as the formate is likely to be a significant sink for such oxidants and therefore minimize complex degradation. Results for the dynamics of the Fe^{IV}-*tpena* complex will be considered first, with consideration of the formate oxidation presented in a later section.

When variable concentrations of ClO^- are added to solutions containing 100 µM Fe-*tpena* and 1 mM formate, similar dynamics are observed, i.e., the Fe^{IV}-*tpena* concentration rises to a peak, remains stable for a brief period (presumably in a dynamic steady-state) before then decaying, presumably due to exhaustion of the available ClO^- (Figure 5-5). In general, it appears that the Fe^{IV}-*tpena* concentration approaches a

plateau with increasing ClO^- concentration, however, this concentration appears to plateau at approximately half of the total Fe-*tpena* concentration present, i.e., it is *not* stoichiometric oxidation of Fe^{III}-*tpena* to Fe^{IV}-*tpena* but, rather, some sort of dynamic equilibrium (if it was a stoichiometric oxidation then Fe^{IV}-*tpena* would approach quantitative production). Investigation of the growth and decay of the Fe^{IV}-tpena have been considered separately.

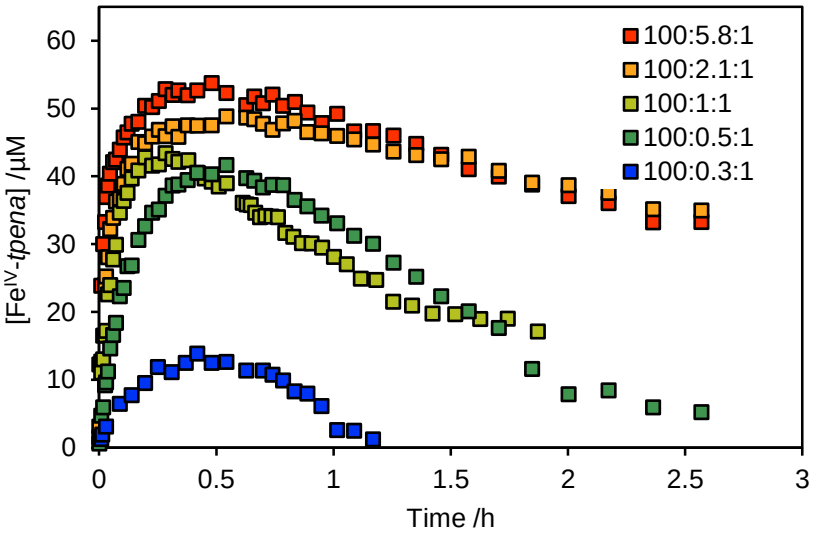

Figure 5-5. Dynamics of Fe^{IV}-*tpena* upon addition of ClO^- (0.3, 0.5, 1, 2.1 and 5.8 mM) to 100 µM Fe-*tpena* and 1 mM formate. Series are labelled [Fe-*tpena*]/µM : [ClO^-]/mM : [formate]/mM

Exponential growth functions were fitted to investigate the dynamics of the Fe^{IV}-*tpena* generation (Figure 5-6). For the high ClO^- concentrations, a two-component exponential growth function of the form shown below was required to obtain a good fit to the rapid initial period.

$$[\mathrm{Fe^{IV}\text{-}tpena}] = C_1\left(1-e^{-k_1' t}\right)+C_2\left(1-e^{-k_2' t}\right)$$

From these fits, both the pseudo first-order rate constant of Fe^{IV}-*tpena* generation and the steady-state Fe^{IV}-*tpena* concentration could be estimated. Presumably, this Fe^{IV}-

tpena generation occurs as a result of some reaction between Fe^{III}-*tpena* and ClO^-; considering this and the properties of exponential functions, an estimate of the pseudo first-order decay rate constant (k'_{ini}) of Fe^{III}-*tpena* can be derived as follows:

$$k'_{ini} = \left(\frac{d[Fe^{III}\text{-}tpena]}{dt}\bigg|_{t=0} \right) \Big/ [Fe^{III}\text{-}tpena]_0$$

Noting that

$$\frac{d[Fe^{III}\text{-}tpena]}{dt} = -\frac{d[Fe^{IV}\text{-}tpena]}{dt}$$

we can determine for the one component fits that:

$$k'_{ini} = \frac{k'_1 C_1}{[Fe^{III}\text{-}tpena]_0}$$

and similarly, for the two-component fits:

$$k'_{ini} = \frac{k'_1 C_1 + k'_2 C_2}{[Fe^{III}\text{-}tpena]_0}$$

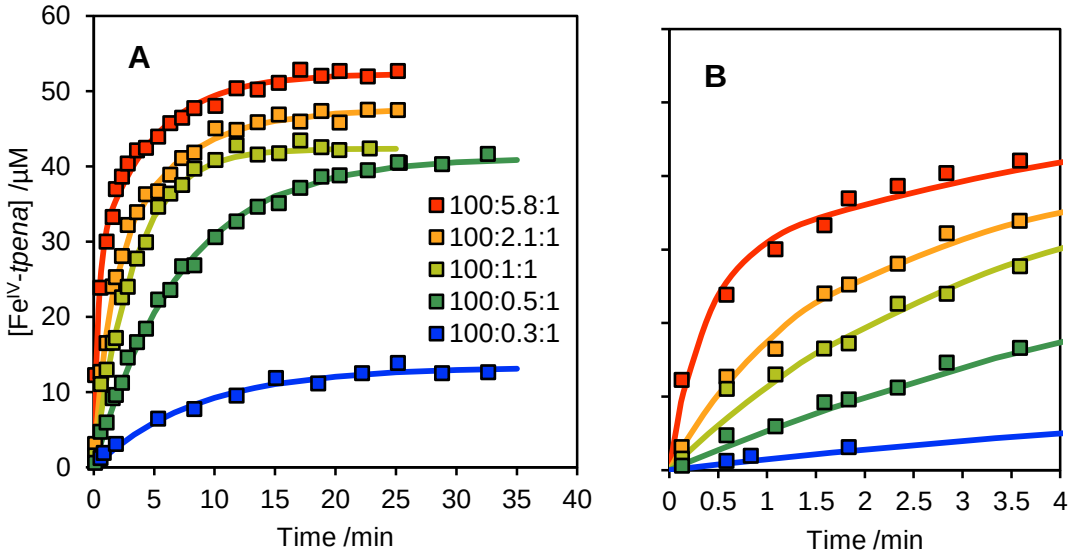

Figure 5-6. Dynamics of Fe^{IV}-*tpena* formation upon addition of ClO^- (0.3, 0.5, 1, 2.1 and 5.8 mM) to 100 μM Fe-*tpena* and 1 mM formate. Series are labelled [Fe-*tpena*]/μM : [ClO^-]/mM : [formate]/mM. Solid lines show exponential growth function fits to the data. Panel B is a close-up of the earlier times in A. Series are labelled [Fe-*tpena*]/μM : [ClO^-]/mM : [formate]/mM.

If the assumption that Fe^{IV}-*tpena* generation proceeds through a rate limiting step involving Fe^{III}-*tpena* and ClO^- is reasonable, then a plot of k'_{ini} against [ClO^-] should yield a straight line, with the slope representing the apparent rate constant for this reaction. As shown in Figure 5-7A below, such behaviour was indeed observed, with $k = 2.4 \pm 0.1\ M^{-1}s^{-1}$ determined. As well as this estimate of the reaction rate, these fits also provide robust estimates of the peak Fe^{IV}-*tpena* concentrations (Figure 5-7 B).

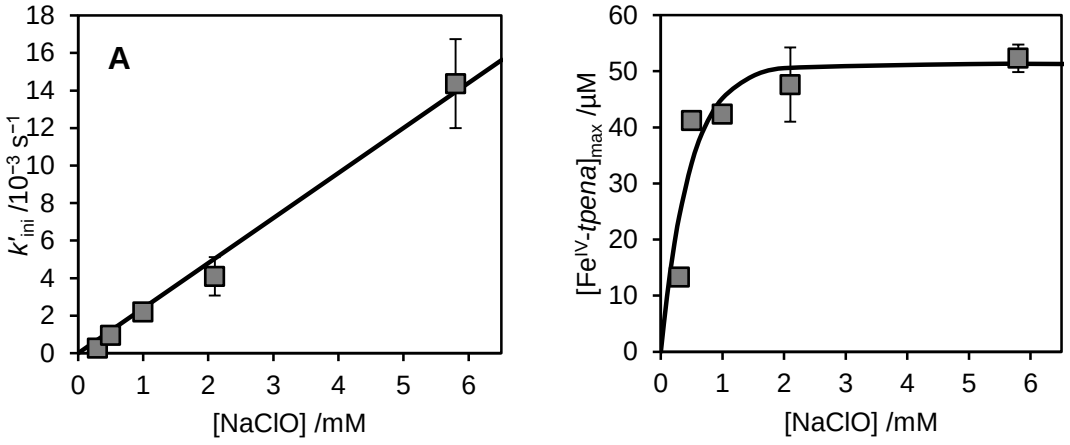

Figure 5-7.(A) Initial pseudo first-order decay rate constants for Fe^{III}-*tpena* (k'_{ini}) determined from Fe^{IV}-*tpena* concentrations as a function of initial NaClO concentration. The slope is found to be $2.4 \pm 0.1\ M^{-1}s^{-1}$. (B) shows the maximum Fe^{IV}-*tpena* concentration achieved as a function of NaClO concentration, with the solid line demonstrating the trend observed.

The second aspect to the Fe^{IV}-*tpena* dynamics is its subsequent decay. It was found that simple exponential decay functions provide a reasonable reproduction of the observed decay kinetics (Figure 5-8). The decay rate was found to be much slower at higher concentrations of ClO^-, with the decay rate only approaching that expected for the self-decay and formate oxidation (determined in Chapter 3) at the lowest concentration of ClO^-. This behaviour suggests that the observed Fe^{IV}-*tpena* concentration reflects a dynamic pseudo-equilibrium condition, which drops to lower Fe^{IV}-tpena concentrations as the ClO^- is consumed, presumably by reaction with both Fe^{III}-*tpena* and Fe^{IV}-*tpena*. It is not clear what is driving this process in detail.

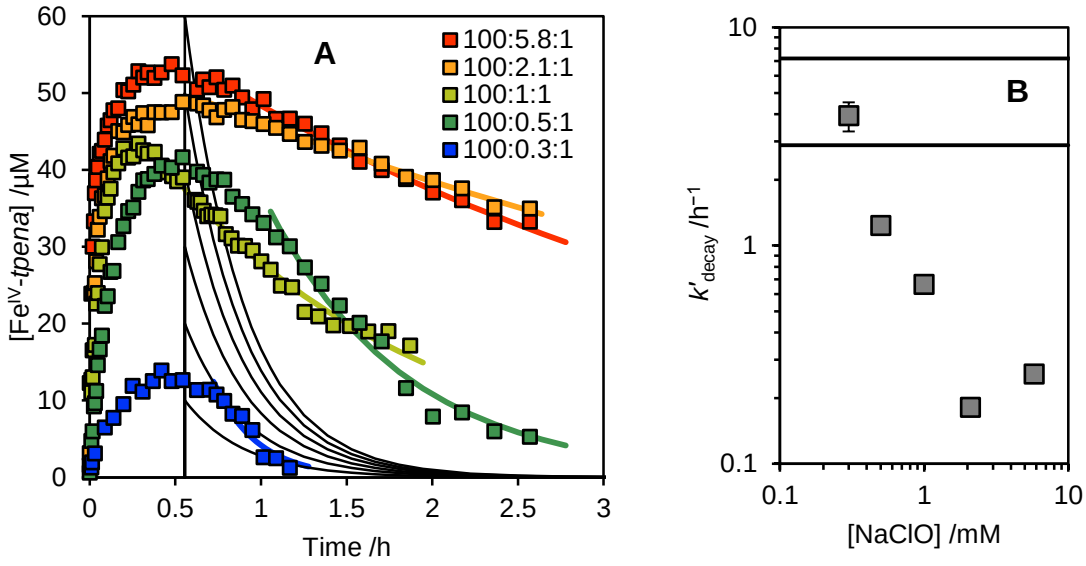

Figure 5-8. (A) Exponential fits to decay of Fe^{IV}-*tpena*. Solid lines are data, solid coloured lines the exponential decay fits. Series are labelled [Fe-*tpena*]/µM : [ClO^-]/mM : [formate]/mM. Solid black lines show the expected self-decay rate for Fe^{IV}-*tpena* determined from Chapter 3. Panel (B) shows the rate constants from (A), with the solid line the self-decay rate constant and the dashed line the self-decay rate constant + decay rate from 1 mM formate (both determined from data in Chapter 3).

As well as the data where Fe-*tpena* was fixed and NaClO varied, data was also collected with [NaClO] = 0.5 mM, [formate] = 1 mM and [Fe-*tpena*] varied from 50 to 200 µM. Now, it was just shown that increasing the ClO^- concentration did not change the peak Fe^{IV}-*tpena* concentration, however, as can be seen in Figure 5-9, when Fe-*tpena* is increased, the Fe^{IV}-*tpena* peak concentration also increases, although this increase is not a simple linear process. The reason for this non-linearity in Fe-*tpena* concentration may be that the ClO^- may have been appreciably reacted before the peak concentration was reached at the higher Fe-*tpena* concentrations The rate of formation and decay do not appear to change significantly.

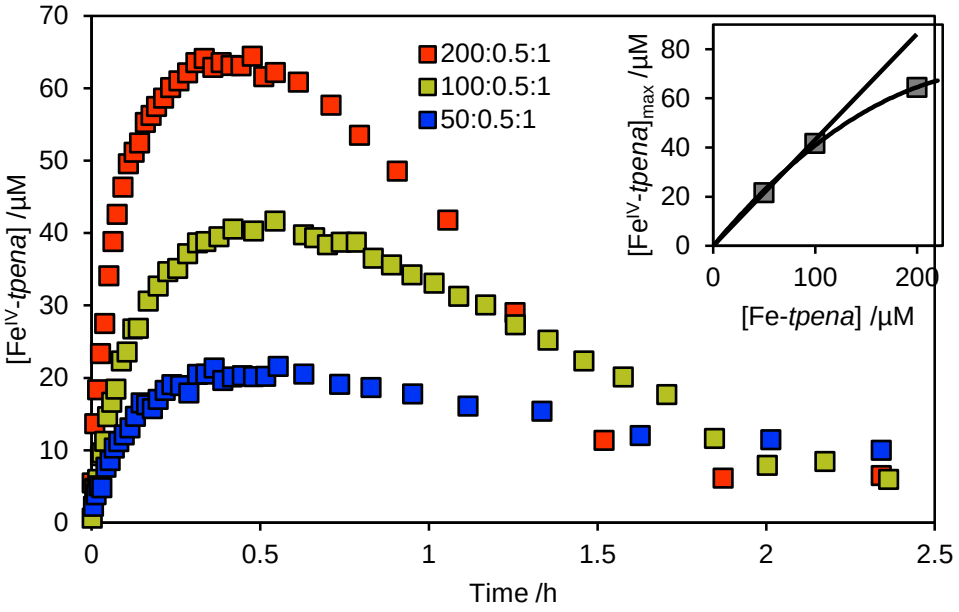

Figure 5-9. Generation of Fe^{IV}-*tpena* at varied Fe-*tpena* concentrations ([NaClO] = 0.5 mM, [formate] = 1 mM). Series are labelled [Fe-*tpena*]/µM : [ClO^-]/mM : [formate]/mM. Inset shows the peak Fe^{IV}-*tpena*

The final condition examined for its impact on Fe^{IV}-*tpena* concentration was the effect of the concentration of formate. When formate concentration is increased, both the longevity and peak concentration of Fe^{IV}-*tpena* are significantly reduced (Figure 5-10). This provides strong support for the notion that formate is a significant sink for Fe^{IV}-*tpena*, and, conversely, also suggests that Fe^{IV}-*tpena* is likely a major oxidant for formate.

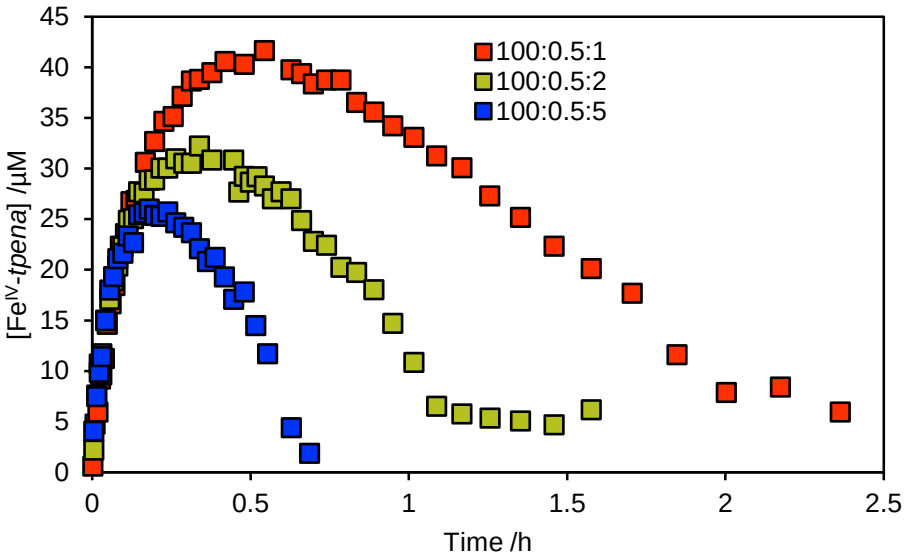

Figure 5-10. Impact of initial formate concentration (1, 2, or 5 mM) on Fe^{IV}-*tpena* generation from 100 μM Fe-*tpena* and 0.5 mM NaClO

5.3.3 Formate oxidation by Fe-*tpena* + NaClO system

The oxidation of formate was observed to occur in the Fe-*tpena* + NaClO system. Experiments were conducted under the same conditions as those discussed in the previous section, allowing the trends observed to be compared amongst them. As well as Fe^{IV}-*tpena* (and any other potential oxidants formed from Fe-*tpena* and ClO^-), the direct reaction of formate with HClO also needs to be considered; Lister and Rosenblum (1963) have previously reported a rate constant for this reaction of 4.1×10^{-2} $M^{-1}s^{-1}$, with the rate constant under the conditions of this work expected to be lower, as ClO^- is the dominant form of hypochlorite at the pH used here. Although the reaction is very slow, it still needs to be considered in this system as control experiments in the absence of Fe-*tpena* do record noticeable degradation at the higher NaClO concentrations. As can be seen in Figure 5-11, the oxidation rate when Fe-*tpena* is present is always substantially greater than that observed in its absence.

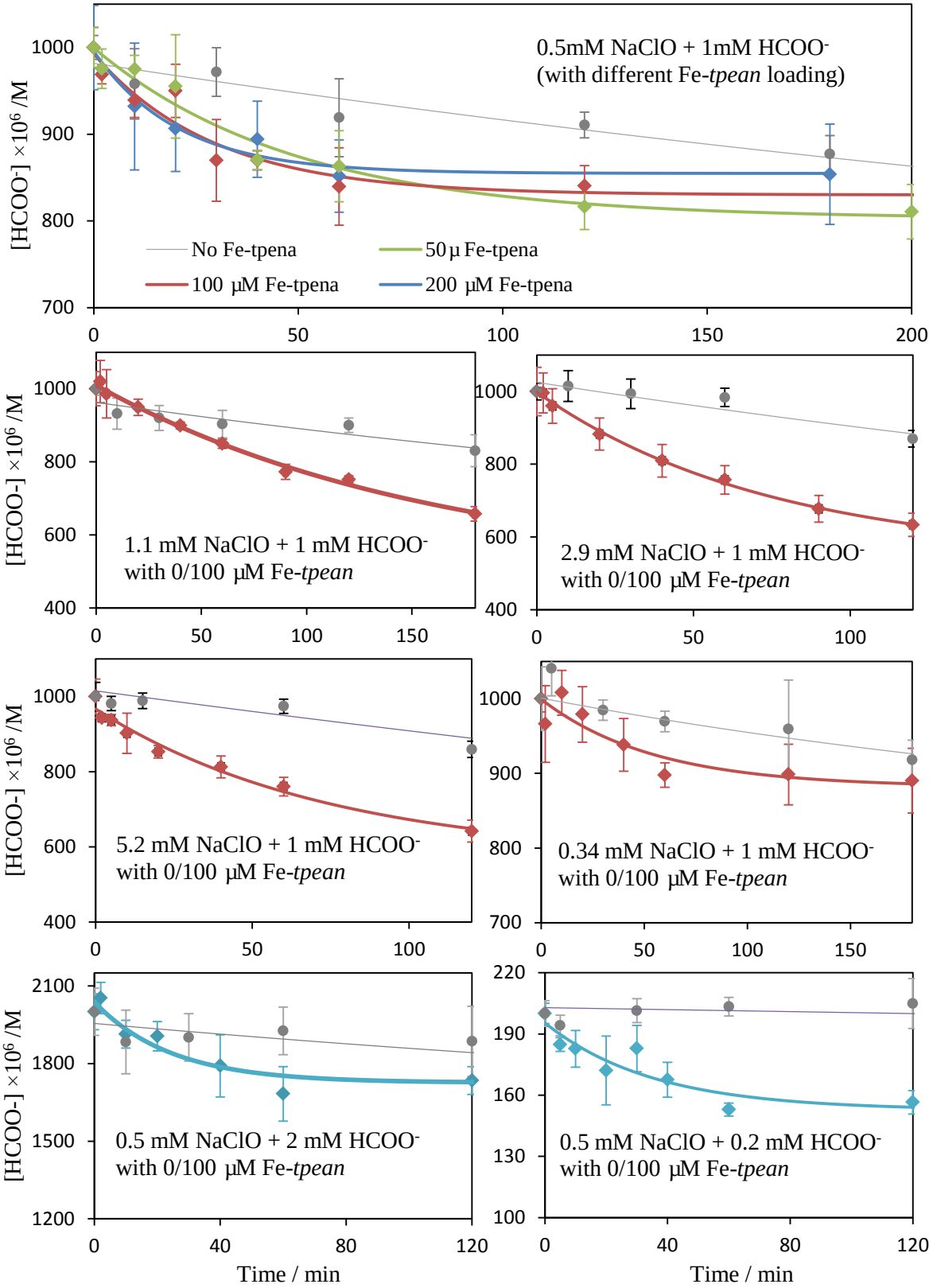

Figure 5-11. Variation of formate concentration with time at different NaClO/formate loadings with (coloured diamonds) or without (grey dots) Fe-tpena, and their exponential fits (solid lines) to extract the observed rate constants.

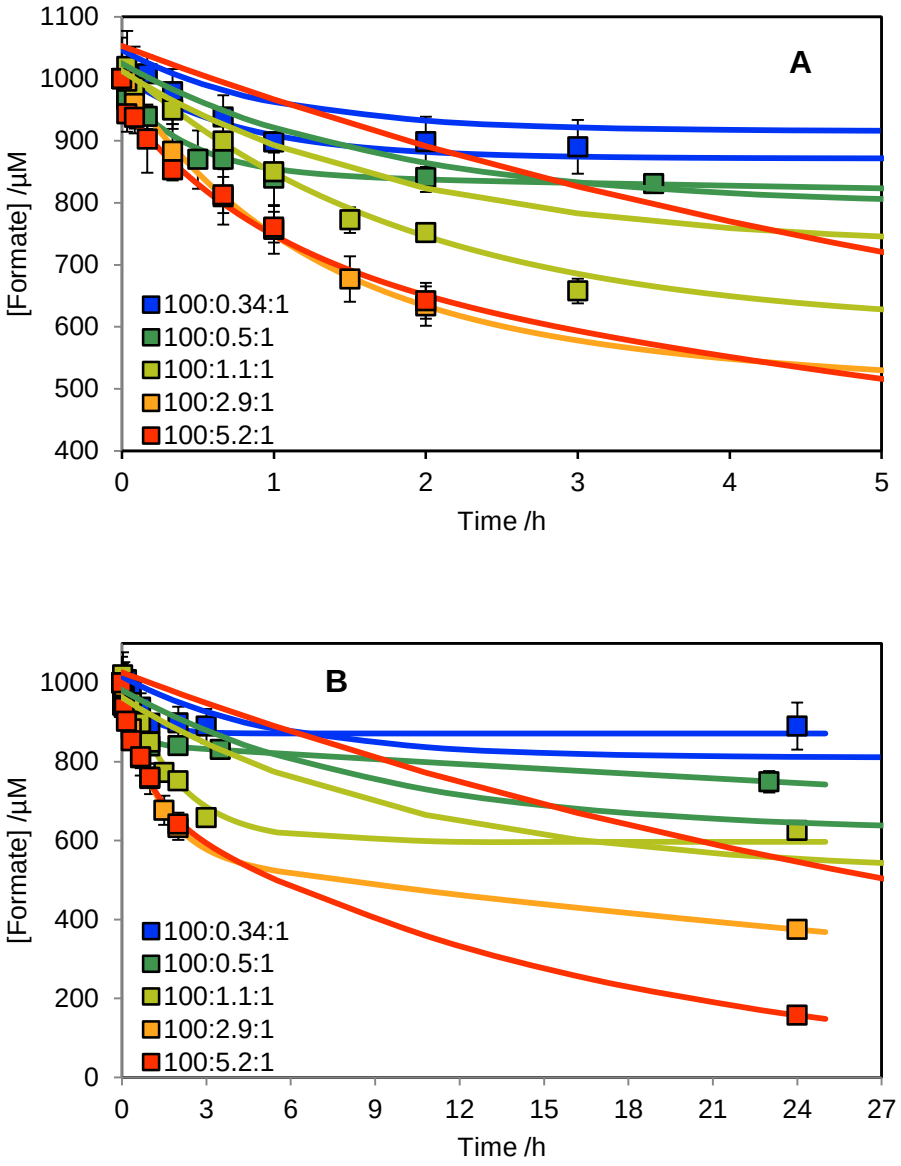

Figure 5-12. Oxidation of formate by NaClO in the presence and absence of Fe-*tpena* at short (A) and long (B) timescales. Symbols are experimental data, solid lines the best fit data in presence of Fe-*tpena* and broken lines the control experiment results in the absence of Fe-*tpena*.

Examining the series where Fe-*tpena* and formate were held constant and the NaClO concentration increased, it is found that the observed decay of formate does not change appreciably (Figure 5-12). This was confirmed through examination of the initial rate of this oxidation determined from curve fitting exponential functions, with the initial rates of formate oxidation, as well as the total formate oxidation observed at one day, shown in Figures 5-13A and B. Although the presence of Fe-*tpena* leads to faster overall

oxidation of formate, in its absence a more complete formate oxidation is observed. Importantly, although more NaClO leads to more extensive degradation, as can be seen in Figure 5-13B, this is not accompanied by a more rapid rate, i.e., this suggests that the main oxidant is present at a similar concentration despite the change in NaClO concentration but is present in the system for longer and therefore able to oxidize more formate. This is consistent with Fe^{IV}-*tpena* being the main oxidant of formate, as its concentration was found to exhibit such behaviour with varying NaClO concentration in the previous section (e.g., see Figure 5-8A)

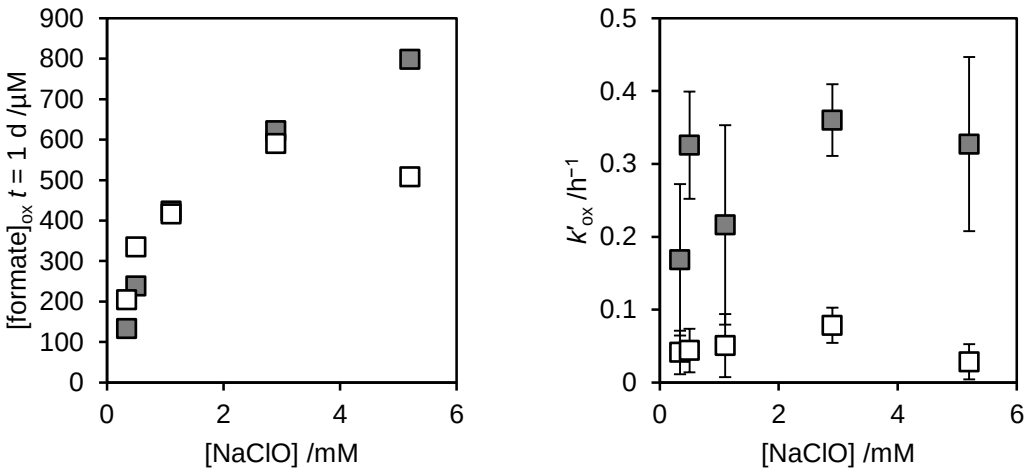

Figure 5-13. Total amount of formate oxidized at one day (A) and overall oxidation rate of formate by NaClO in the presence (closed squares) and absence (open squares) of Fe-*tpena* (B).

As well as varying the HClO concentration, experiments were also undertaken where the Fe-*tpena* concentration was varied. As shown above, this lead to significant changes in the observed Fe^{IV}-*tpena* concentration, which will presumably lead to changes in the observed formate decay. In Figure 5-14, the rate of formate decay at varied Fe-*tpena* is presented, showing that the increase in observed Fe^{IV}-*tpena* does lead to more rapid formate oxidation. Now, looking closely at the observed oxidation rates, although rather noisy, it is possible to estimate the rate constant needed between formate and Fe^{IV}-*tpena* to explain the data (Figure 5-15). It was found that a rate constant for the reaction

between Fe^{IV}-*tpena* and formate of 1.2 ± 0.4 $M^{-1}s^{-1}$ was sufficient to explain the observed formate oxidation rate. This rate constant is in excellent agreement with that determined in Chapter 3, providing some evidence that Fe^{IV}-*tpena* is the dominant strong oxidant generated. However, considering the extensive uncertainty in this figure, this does not provide strong evidence that Fe^{IV}-*tpena* is the only oxidant, but does demonstrate that it is possible that it is the dominant oxidant.

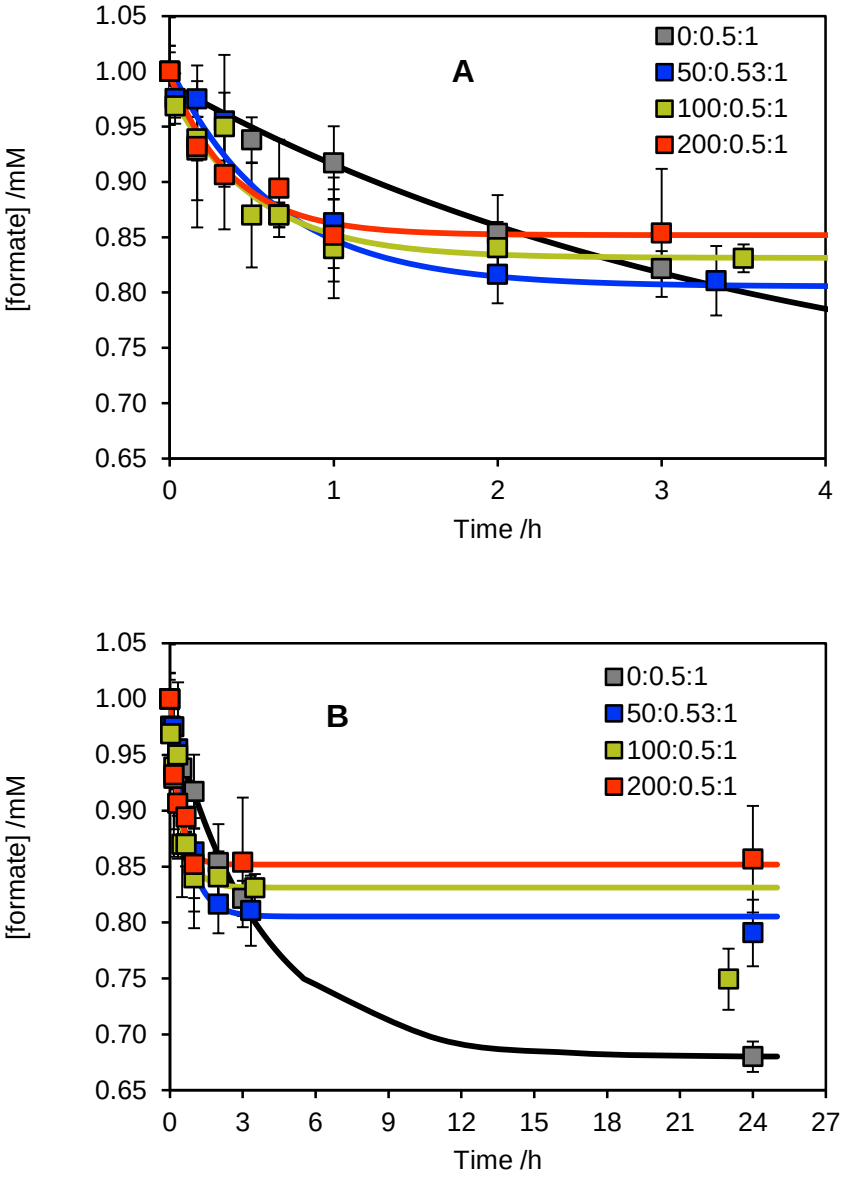

Figure 5-14. Changes in formate oxidation at varied Fe-*tpena* concentration and [NaClO] = 0.5 mM, [formate] = 1 mM at short timescale (a) and longer timescale (b)

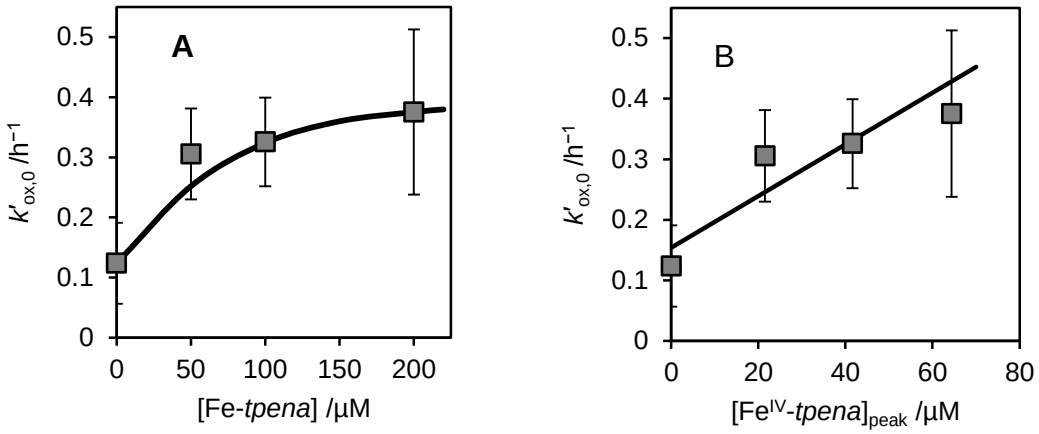

Figure 5-15. Oxidation rate of formate at varied Fe-*tpena* concentration. Panel A shows as a function of the initial Fe-*tpena* concentration, panel B shows this rate correlates with the observed peak Fe^{IV}-*tpena* concentration, with the slope giving $k = 1.2 \pm 0.4$ M^{-1}s^{-1}

The final condition examined was the case where the formate concentration was varied with the Fe-*tpena* and NaClO concentrations held constant (Figure 5-16). Despite changing the formate concentration from 0.2 to 5 mM, the same general behaviour was observed in that within about one hour ~15% of the formate present was oxidized (i.e., ~about 40 μM for initial formate of 0.2 mM but ~400 μM for initial formate of 5 mM), while control experiments in the absence of Fe-*tpena* show no obvious formate oxidation in one hour. The observation that the same relative extent of oxidation occurs with the same apparent rate constant means that in each case the formate is exposed to the same concentration of the oxidant for the same duration of time and indicates that it is not the total amount of oxidant formed that is limiting the extent of oxidation. This would suggest that formate is not significantly influencing the steady-state concentration of the oxidant and that it is perhaps only one rather minor pathway available for its removal. However, in Figure 5-10, formate was shown to quite significantly alter the observed Fe^{IV}-*tpena* profiles, albeit with reasonably similar observed maximum Fe^{IV}-*tpena* concentrations. Under the hypothesis that Fe^{IV}-*tpena* is the main oxidant of formate (as we know that the pseudo first-order rate of its reaction with formate (2.4×10^{-4} to 6.0×10^{-3} s^{-1}) will be comparable to or somewhat greater than its self-decay rate (~8×10^{-4} s^{-1}) under the conditions examined here), this requires that an additional pathway for Fe^{IV}-*tpena* removal must exist if the steady state

concentration of Fe^{IV}-*tpena* is not too change substantially. The most likely explanation must be a reaction with ClO^- which, to be larger than formate under all conditions, would require a rate constant for this reaction of at least ~12 $M^{-1}s^{-1}$. However, the uncertainty in this data can be seen to be rather large, so this deduction is not strongly supported.

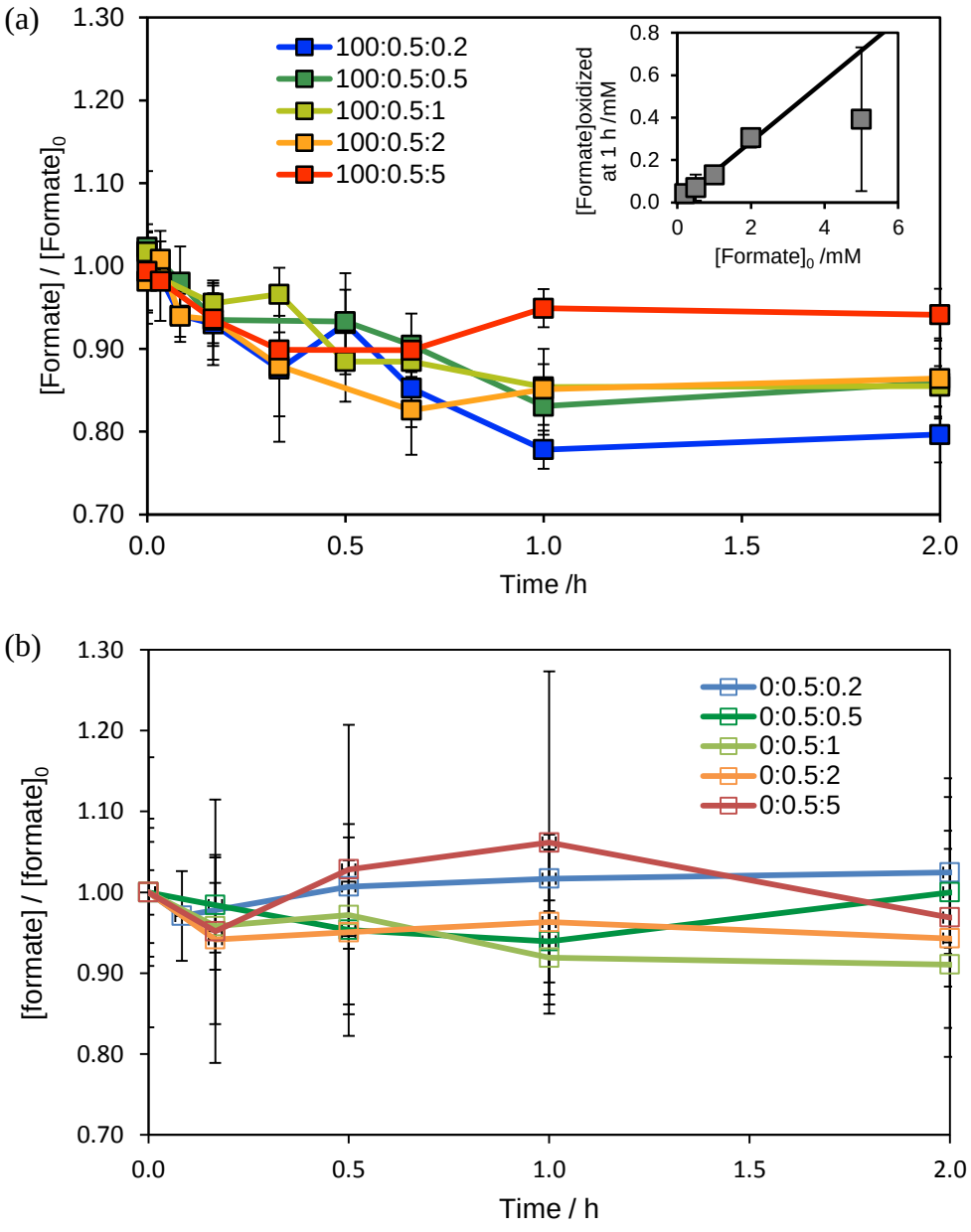

Figure 5-16. Oxidation of formate (0.2, 0.5, 1, 2 and 5 mm) by (a) 100 µM Fe-*tpena* and 0.5 mM NaClO, and (b) 0.5 mM NaClO in the absence of Fe-*tpena*. The relative change in formate concentration is plotted. The inset shows the absolute magnitude of the change in formate concentration after one hour of reaction as a function of initial formate concentration.

5.3.4 Re-activation of Fe-*tpena*

Following the formate degradation experiments described above, NaClO (set at 0.5 mM) was re-introduced into the system and Fe^{IV}-*tpena* generation and, in some cases, further formate degradation was observed though with apparent activity loss. This result indicates re-generation of the resting state Fe-*tpena* with the effectiveness of this regeneration varying at different NaClO/Fe-*tpena*/formate loadings.

Re-activation of residual reactant mixtures with different formate loadings (first spike data in Figure 5-10) were all successful (as shown in Figure 5-17a), which cannot be achieved in the absence of substrate, and which seems more effective at higher substrate loading. This is similar to the H_2O_2/Fe-*tpena* system and could be due to the competition of formate in reactions between Fe-*tpena* and radicals (illustrated in Figure 5-18) though the radicals are not as active to Fe-*tpena* as $HO^{\bullet}$.

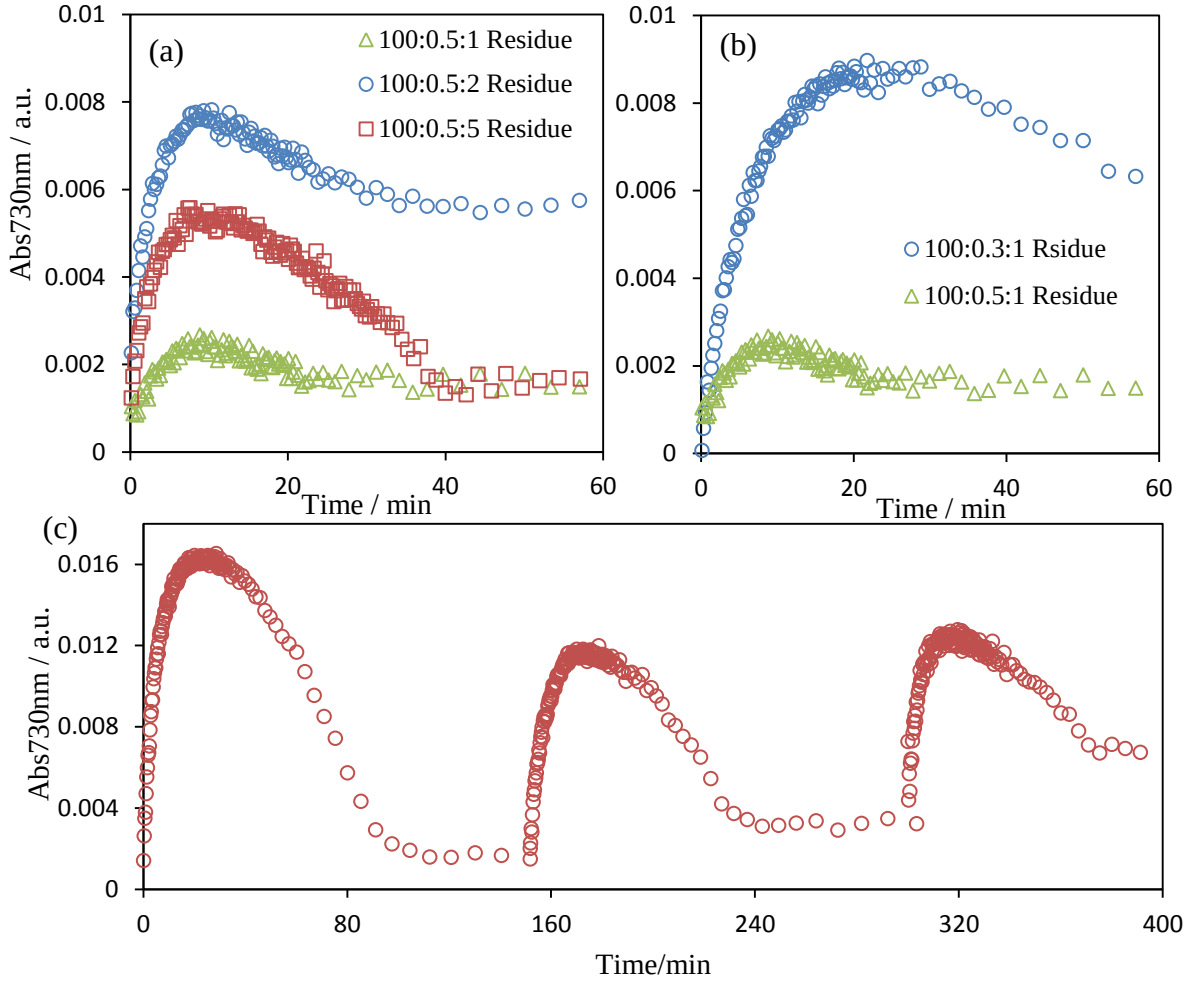

Figure 5-17 Time-trace of Abs 730 nm (Fe^{IV}-*tpena*) from the second shot of NaClO (0.5 mM) when (a) different initial formate loadings (1, 2 and 5 mM) were used for the first NaClO spike, and (b) different NaClO loadings (0.3 and 0.5 mM) were used in the first run. (c) Additions of 0.5 mM NaClO (three spikes) into 200 μM Fe-*tpena* and 1mM HCOONa.

Similarly, the re-activation of Fe^{IV}-*tpena* also prefers lower NaClO loading (Figure 5-17b) and/or higher Fe-*tpena* loading in the first spike. In the cases where NaClO loading was too high (≥ 2 mM) or Fe-*tpena* loading was too low (≤50 μM) in the first run, no Fe^{IV}-*tpena* re-generation can be observed through UV-vis spectra, while a starting Fe-*tpena* loading of 200 μM can survive three shots of 0.5 mM NaClO (Figure 5-17c). Formate degradation by repeated NaClO (0.5 mM) addition in the presence of 200 μM Fe-*tpena* was also monitored and resulted in a total of ~30% [$HCOO^-$] decrease. It seems that Fe-*tpena* left for the third run is already too low for effective formate degradation. Clearly, protection of Fe-*tpena* from radical attack is necessary for its longevity.

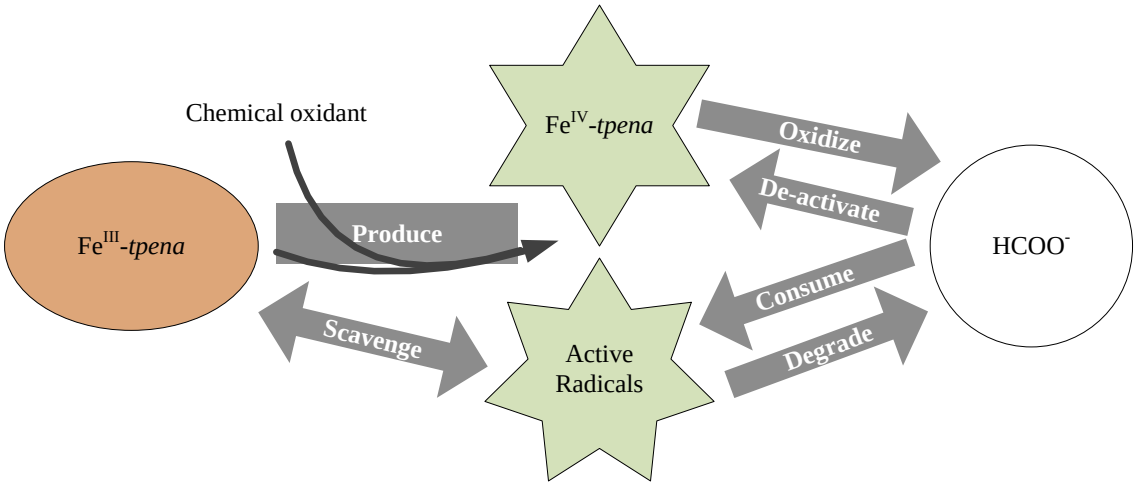

Figure 5-18 Competition in a Fe^{IV}-*tpena*/radicals system

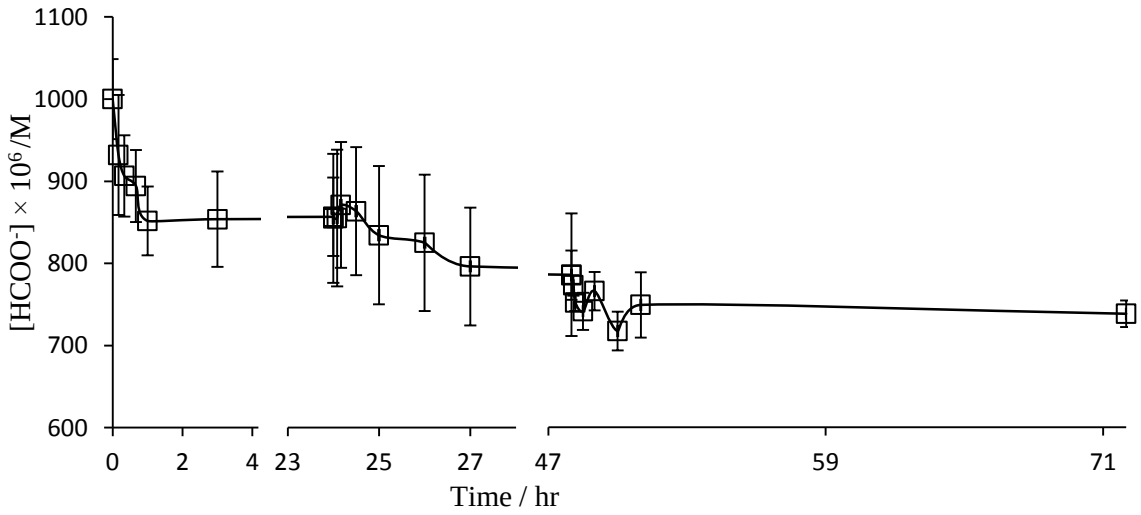

Figure 5-19 Time trace of [HCOO$^-$] upon three additions of 0.5 mM NaClO into 200 μM (per Fe) Fe-*tpena* with 1mM starting [HCOO$^-$].

5.3.5 Basic model of Fe-*tpena* + HClO system

From the previous sections, some of the key features of the system could be conceptualised into a simple reaction scheme which considers i) that ClO^- can both oxidize Fe^{III}-*tpena* and reduce Fe^{IV}-*tpena*, ii) that Fe^{IV}-*tpena* decays by this reaction as well as self-decay by reaction with water and also oxidation of formate and iii) that

formate is directly oxidized by ClO^-. These reactions and their rate constants are set out below. The rate constants were either those determined earlier in this Chapter, in Chapter 3, or from Lister and Rosenblum (1963); the only exception was reaction 2., which was earlier suggested to be ~12 $M^{-1}s^{-1}$ in the previous section, however, reasonable fits could only be achieved with much smaller values, with ~2.5 $M^{-1}s^{-1}$ giving the best fits

1. Fe^{III}-*tpena* + ClO^- → Fe^{IV}-*tpena* $k = 2.4 \pm 0.2\ M^{-1}s^{-1}$
2. Fe^{IV}-*tpena* + ClO^- → Fe^{III}-*tpena* $k = 2.5 \pm 0.3\ M^{-1}s^{-1}$
3. Fe^{IV}-*tpena* → Fe^{III}-*tpena* $k = (8 \pm 1) \times 10^{-4}\ s^{-1}$
4. Fe^{IV}-*tpena* + $HCOO^-$ → Fe^{III}-*tpena* $k = 1.2 \pm 0.2\ M^{-1}s^{-1}$
5. ClO^- + $HCOO^-$ → Products $k = (4 \pm 0.3) \times 10^{-2}\ M^{-1}s^{-1}$

Although the best fits (shown in Figures 5-20 and 5-21) do not coincide precisely with the experimental data, it provides a reasonable description of the basic trends in the system. However, it does a poor job at predicting the impact of the ClO^- concentration on the peak Fe^{IV}-*tpena* concentration, as well as at predicting the observed decay rate of Fe^{IV}-*tpena*. The model as presented is clearly missing some key processes that have yet to be elucidated. Attempts to apply a model similar to that in Chapter 4 were also unsuccessful. Further work will be required to determine what this missing process may be.

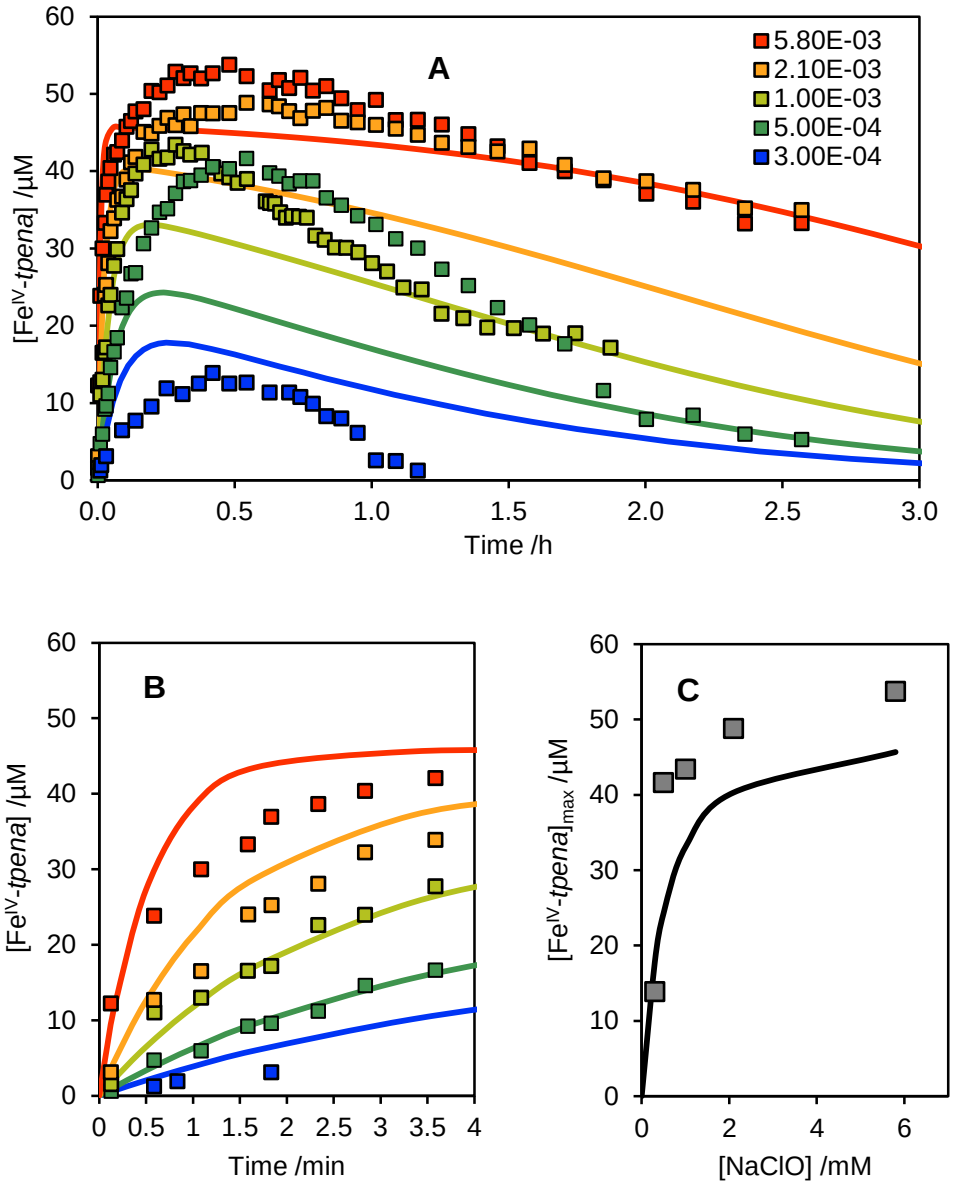

Figure 5-20. Simple model fit to the NaClO variation data. Panel (A) shows the full data, (B) just the initial stage and (C) the predicted (lines) and observed (points) peak Fe^{IV}-*tpena* concentrations

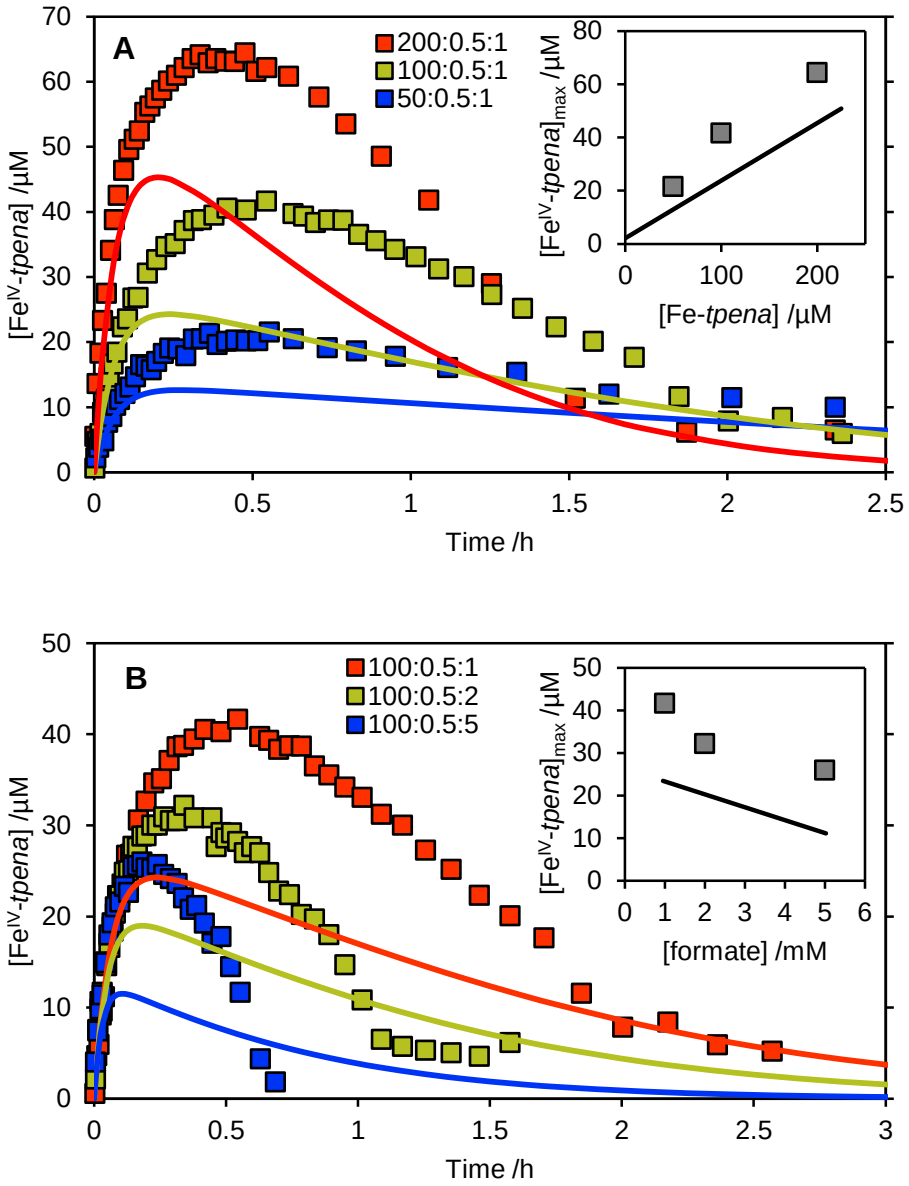

Figure 5-21. Simple model fit to the Fe-*tpena* concentration variation experiments (A) and the formate concentration variation experiments (B). Points are experimental values and lines the model output. Insets show the predicted and observed peak Fe^{IV}-*tpena* concentrations

5.4 Conclusion

In the NaClO/Fe-*tpena* system, Fe^{IV}-*tpena* can be maintained at a significant level for some hours providing appropriate amounts of NaClO and Fe-*tpena* are used. Although some reactions are still missing in the model developed in 5.3.4, it is clear that Fe^{IV}-*tpena* is the main active oxidant since the rate constant (1.2 ± 0.4 $M^{-1}s^{-1}$) between Fe^{IV}-*tpena* and formate is sufficient to explain the observed formate oxidation. There are

possibly radicals (such $ClO^{\bullet}$ and $Cl^{\bullet}$) generated along with Fe^{IV}-*tpena* which can both contribute somewhat to substrate degradation and Fe-*tpena* consumption with further work required to clarify this issue. Adding Fe-*tpena* to a NaClO solution can bring the reaction time of degrading the same amount formate from up to 1 day by NaClO alone down to less than 3 hours. Providing the longevity of Fe-*tpena* can be improved, Fe-*tpena*/NaClO could well be a powerful oxidising agent.

Chapter 6.
Summary and outlook

6.1 Summary

In this thesis, Fe-TAML and Fe-*tpena* – two biomimetic iron complexes that can generate high valence state iron in situ upon activation by electron receptors – have been examined in terms of their potential application for water contaminant degradation.

Initial studies in Chapter 2 focussed on the most widely published biomimetic catalyst Fe-TAML, and focused in particular on the impact of immobilisation on its activity. It was demonstrated that simple fixation of Fe-TAML can improve its longevity and also allows for electrochemical activation. Using RhB as a target compound, heterogeneous Fe-TAML physically adsorbed to graphite particles exhibited good oxidising activity at pH 9 when activated by H_2O_2 when appropriate Fe-TAML/H_2O_2 loadings were used. However, although the supported Fe-TAML retained its reactivity with H_2O_2, its utility was still limited by the same high pH requirement as for homogeneous Fe-TAML, with the best activity observed at the highest pH examined (pH 9.5).

Direct electrochemical activation of the graphite-supported Fe-TAML was also attempted, as this should avoid, or at least minimize, this need for high pH, as the high pH requirement is due to the protonation state requirements of the Fe-TAML – H_2O_2 interaction; this would no longer be relevant if the Fe^{IV} state could be formed directly electrochemically. The graphite-supported Fe-TAML was demonstrated to be able to effectively degrade RhB at neutral pH, although the enhancement relative to direct electrochemical oxidation of RhB by graphite alone suggested that although possible, it was unlikely to be sufficiently active for practical applications.

In Chapter 3 focus was shifted to an emerging biomimetic oxidation catalyst, Fe-*tpena*, which is also known to support formation of Fe^{IV} and was considered likely to possess superior properties to Fe-TAML. The initial studies in Chapter 3 demonstrated that high-valent Fe^{IV}-*tpena* can be readily generated electrochemically in homogeneous conditions, and showed that it is relatively stable (in the absence of substrates) across a wide pH range (from acidic pH to up to pH 9). The ability of this electrochemically generated Fe^{IV}-*tpena* to oxidize a wide range of substrates was then examined. It was found that Fe^{IV}-*tpena* is a promiscuous oxidant able to completely mineralize organic compounds, evidenced by its ability to oxidize formate to CO_2, much like $HO^{\bullet}$, the existing "gold standard" oxidant for water and wastewater treatment. Although the magnitude of its rate constants with organic compounds is much lower than $HO^{\bullet}$, this is offset by the capacity to generate Fe^{IV}-*tpena* at concentrations many orders of magnitude higher than could ever be achieved for $HO^{\bullet}$.

After determining that Fe^{IV}-*tpena* shows great promise as an oxidant, Chapters 4 and 5 then explored chemical means to generate Fe^{IV}-*tpena* as alternatives for the electrochemical approach employed in Chapter 3. Importantly, this chemical activation work was conducted at circumneutral pH ~ 8, which is of relevance to practical applications and also too low for Fe-TAML + H_2O_2 to be effective. Chapter 4 focussed on the use of H_2O_2, considered a green oxidant due to its formation of only H_2O as a by-product of its use, and already widely employed in a range of oxidation technologies, such as the Fenton process. Fe-*tpena* was found to be highly reactive towards H_2O_2, although no direct observation of Fe^{IV}-*tpena* could be made due to Fe^{IV}-*tpena* also being able to react with H_2O_2. None-the-less, the Fe-*tpena* + H_2O_2 system was found to be a competent oxidant generating system with oxidation of RhB, Phth and formate demonstrated. The use of these probe compounds allowed for resolution of the kinetics of the process, with a comprehensive mechanistic kinetic model developed that explained all experimental observations. It was shown that the probe compound degradation could only be explained if both Fe^{IV}-*tpena* and $HO^{\bullet}$ were formed upon interaction of Fe-*tpena* and H_2O_2. This concomittant production of $HO^{\bullet}$ opens up additional possibilities for application of this system in oxidation technologies, although also poses challenges due to undesirable oxidation of the *tpena* ligand.

In Chapter 5 the potential for Fe-*tpena* to be activated by ClO^- was examined; as ClO^- is ubiquitously employed in drinking water treatment globally, there is great potential for practical application, should the process be effective. Much like H_2O_2, ClO^- was found to be reactive with Fe-*tpena*, however, in contrast to H_2O_2, when ClO^- is used there is observable and significant build up of Fe^{IV}-*tpena*, as the Fe^{IV}-*tpena* is apparently much less reactive towards ClO^- than H_2O_2. The Fe-*tpena* + ClO^- system was shown to be able to degrade formate, as was expected from the results of previous Chapters. Due to direct reactions of ClO^- with Phth and RhB complicating the interpretation of oxidation studies with these probes, these probes were not investigated in this system. Although at high ClO^- concentration there was some apparent ligand destruction that reduced the effectiveness of the Fe-*tpena* upon repeated additions of ClO^- to Fe-*tpena*, presumably also due to generation of an unknown radical oxidant, this was less problematic at lower ClO^- concentrations more typical of water treatment applications, with good repeatability of oxidation performance was found on repeated ClO^- additions. A complete mechanistic interpretation of the Fe-*tpena* + ClO^- system could not be made, although the results clearly demonstrate both the effectiveness and potential of this system.

This thesis allows for some comparison to be made between the first generation Fe-TAML and the recently developed Fe-*tpena*; although they can both be electrochemically activated to the Fe^{IV} state in ambient conditions with the Fe^{IV} species active toward degradation of dyes and other chemicals, chemical activation of Fe-TAML is limited to high pH, whereas here it has been shown that Fe-*tpena* exhibits excellent reactivity under circumneutral conditions. For these reasons, Fe-*tpena* appears to be a very promising alternative catalyst under conditions where Fe-TAML is less applicable.

6.2 Outlook and challenge

The results of this thesis suggests that both Fe-*tpena* and Fe-TAML show promise for the development of electrochemical water treatment technologies. However, although physically adsorbed Fe-TAML was shown to be effective in this work, for practical application more robust attachment would be desired, with the development of strong

covalent attachment methods that retain the chemical activity of the Fe complexes a pressing need for future application.

In terms of the chemically-activated oxidant generating systems, it has been shown that physical adsorption of the Fe-TAML, although useful in some ways, does not overcome the rigorous high pH requirements of the H_2O_2 + Fe-TAML system. Although it is unclear what effect more permanent attachment methods may have, any such method is unlikely to show different behaviour in that respect. This result highlights the importance of finding a process with desirable pH behaviour before pursuing attachment strategies, which is indeed the approach being taken in the Collins group regarding their ongoing work on TAML ligand design. In this regard, the excellent functionality of the Fe-*tpena* ligand towards chemical activation under pH conditions relevant to drinking water treatment processes would suggest that this ligand is ripe for future work aiming to better exploit this compound in a practical technology.

The main limitation highlighted in the Fe-*tpena* chemical activation work was the apparent oxidative destruction of the ligand under some conditions, particularly when H_2O_2 was used. Although this is likely to be less problematic in a practical application when other substrates are present to compete with the ligand, strategies to minimize this as much as possible still need to be explored. It may be possible to refine the concentrations of Fe-*tpena* and H_2O_2 to achieve this, and this should be considered. An alternative approach could be to explore in detail the nature of this ligand destruction with the goal of altering the ligand design to remove any motifs that appear particularly prone to oxidative attack.

While the outlook appears positive, challenges remain before the application of these biomimetic compounds to real waters becomes a reality, including: 1) develevelopment of good fixation methods that can prolong the longevity of the Fe complexes and can be easily recycled from the liquid phase, and 2) further process or ligand design to minimize ligand oxidation and extend the longevity of the complex.

References

ALLEN, N. & LOW, G. W. 1933. Preparation of sodium hydroxide solutions of low carbonate content by centrifugation. *Industrial & Engineering Chemistry Analytical Edition,* 5**,** 192-192.

BABUPONNUSAMI, A. & MUTHUKUMAR, K. 2014. A review on Fenton and improvements to the Fenton process for wastewater treatment. *Journal of Environmental Chemical Engineering,* 2**,** 557-572.

BALLAND, V., CHARLOT, M.-F., BANSE, F., GIRERD, J.-J., MATTIOLI, T. A., BILL, E., BARTOLI, J.-F., BATTIONI, P. & MANSUY, D. 2004. Spectroscopic characterization of an Fe^{IV} intermediate generated by reaction of XO^- (X = Cl, Br) with an Fe^{II} complex bearing a pentadentate non-porphyrinic ligand − hydroxylation and epoxidation activity. *European Journal of Inorganic Chemistry,* 2004**,** 301-308.

BASSAN, A., BLOMBERG, M. R. A., BOROWSKI, T. & SIEGBAHN, P. E. M. 2006. Theoretical studies of enzyme mechanisms involving high-valent iron intermediates. *Journal of Inorganic Biochemistry,* 100**,** 727-743.

BEACH, E. S., MALECKY, R. T., GIL, R. R., HORWITZ, C. P. & COLLINS, T. J. 2011. Fe-TAML/hydrogen peroxide degradation of concentrated solutions of the commercial azo dye tartrazine. *Catalysis Science & Technology,* 1**,** 437-443.

BEHIN, J., AKBARI, A., MAHMOUDI, M. & KHAJEH, M. 2017. Sodium hypochlorite as an alternative to hydrogen peroxide in Fenton process for industrial scale. *Water Research,* 121**,** 120-128.

BERGMANN, M. E. H., KOPARAL, A. S. & IOURTCHOUK, T. 2014. Electrochemical Advanced Oxidation Processes, Formation of Halogenate and Perhalogenate Species: A Critical Review. *Critical Reviews in Environmental Science and Technology,* 44**,** 348-390.

BIELSKI, B. H. J., CABELLI, D. E., ARUDI, R. L. & ROSS, A. B. 1985. Reactivity of HO_2/O_2^- Radicals in Aqueous Solution. *Journal of Physical and Chemical Reference Data,* 14**,** 1041-1100.

BLANKSBY, S. J. & ELLISON, G. B. 2003. Bond dissociation energies of organic molecules. *Accounts of Chemical Research,* 36**,** 255-263.

BRAUSAM, A. & VAN ELDIK, R. 2004. Further mechanistic information on the reaction between Fe^{III}(edta) and hydrogen peroxide: Observation of a second reaction step and importance of pH. *Inorganic Chemistry,* 43**,** 5351-5359.

BRILLAS, E., SIRES, I. & OTURAN, M. A. 2009. Electro-Fenton process and related electrochemical technologies based on Fenton's reaction chemistry. *Chemical Reviews,* 109**,** 6570-6631.

BUXTON, G. V., GREENSTOCK, C. L., HELMAN, W. P. & ROSS, A. B. 1988. Critical Review of rate constants for reactions of hydrated electrons, hydrogen atoms and hydroxyl radicals (•OH/•O^-) in Aqueous Solution. *Journal of Physical and Chemical Reference Data,* 17**,** 513-886.

CABELLI, D. E., RUSH, J. D., THOMAS, M. J. & BIELSKI, B. H. J. 1989. Kinetics of the free-radical-induced reduction of Fe^{III}DTPA to Fe^{II}DTPA. a pulse radiolysis study. *The Journal of Physical Chemistry,* 93**,** 3579-3586.

CELANO, G., ŠMEJKALOVÁ, D., SPACCINI, R. & PICCOLO, A. 2008. Reduced toxicity of olive mill waste waters by oxidative coupling with biomimetic catalysis. *Environmental Science & Technology,* 42**,** 4896-4901.

CHAHBANE, N., LENOIR, D., SOUABI, S., COLLINS, T. J. & SCHRAMM, K. W. 2007a. Fe(III)-TAML-catalyzed green oxidative decollorization of textile dyes in wastewater. *Clean-Soil Air Water,* 35**,** 459-464.

CHAHBANE, N., POPESCU, D. L., MITCHELL, D. A., CHANDA, A., LENOIR, D., RYABOV, A. D., SCHRAMM, K. W. & COLLINS, T. J. 2007b. Fe-III-TAML-catalyzed green oxidative degradation of the azo dye Orange II by H2O2 and organic peroxides: products, toxicity, kinetics, and mechanisms. *Green Chemistry,* 9**,** 49-57.

CHANDA, A., KHETAN, S. K., BANERJEE, D., GHOSH, A. & COLLINS, T. J. 2006a. Total degradation of fenitrothion and other organophosphorus pesticides by catalytic oxidation employing Fe-TAML peroxide activators. *Journal of the American Chemical Society,* 128**,** 12058-12059.

CHANDA, A., RYABOV, A. D., MONDAL, S., ALEXANDROVA, L., GHOSH, A., HANGUN-BALKIR, Y., HORWITZ, C. P. & COLLINS, T. J. 2006b. Activity-stability parameterization of homogeneous green oxidation catalysts. *Chemistry-a European Journal,* 12**,** 9336-9345.

CHAPLIN, B. P. 2014. Critical review of electrochemical advanced oxidation processes for water treatment applications. *Environmental Science-Processes & Impacts,* 16**,** 1182-1203.

CHEN, J., DRAKSHARAPU, A., ANGELONE, D., UNJAROEN, D., PADAMATI, S. K., HAGE, R., SWART, M., DUBOC, C. & BROWNE, W. R. 2018. H_2O_2 oxidation by Fe^{III}–OOH intermediates and its effect on catalytic efficiency. *ACS Catalysis,* 8**,** 9665-9674.

CHEN, X., LU, W. Y., XU, T. F., LI, N., ZHU, Z. X., WANG, G. Q. & CHEN, W. X. 2017. Visible-light-assisted generation of high-valent iron-oxo species anchored

axially on g-C_3N_4 for efficient degradation of organic pollutants. *Chemical Engineering Journal,* 328**,** 853-861.

CHRISTOFORIDIS, K. C., LOULOUDI, M., MILAEVA, E. R. & DELIGIANNAKIS, Y. 2010. Mechanism of catalytic decomposition of pentachlorophenol by a highly recyclable heterogeneous SiO_2-[Fe-porphyrin] catalyst. *Journal of Catalysis,* 270**,** 153-162.

COLLINS, T. J. 1994. Designing ligands for oxidizing complexes. *Accounts of Chemical Research,* 27**,** 279-285.

COLLINS, T. J., GORDON-WYLIE, S. W., BARTOS, M. J., HORWITZ, C. P., WOOMER, C. G., WILLIAMS, S. A., PATTERSON, R. E., VUOCOLO, L. D., PATERNO, S. A., STRAZISAR, S. A., PERANIO, D. K. & DUDASH, C. A. 1998. The design of green oxidants. *In:* ANASTAS, P. T. & WILLIAMSON, T. C. (eds.) *Green Chemistry.* the United States: Oxford University Press, Inc., New York.

COLLINS, T. J. & RYABOV, A. D. 2017. Targeting of high-valent iron-TAML activators at hydrocarbons and beyond. *Chemical Reviews,* 117**,** 9140-9162.

COLLINS, T. J. & WALTER, C. 2006. Little green molecules. *Scientific American,* 294**,** 82-90.

COSTAS, M., CHEN, K. & QUE, L. 2000. Biomimetic nonheme iron catalysts for alkane hydroxylation. *Coordination Chemistry Reviews,* 200**,** 517-544.

DE LAAT, J. & GALLARD, H. 1999. Catalytic decomposition of hydrogen peroxide by Fe(III) in homogeneous aqueous solution: Mechanism and kinetic modeling. *Environmental Science & Technology,* 33**,** 2726-2732.

DE SOUSA, D. P., MILLER, C. J., CHANG, Y., WAITE, T. D. & MCKENZIE, C. J. 2017. Electrochemically generated cis-carboxylato-coordinated iron(IV) oxo acid–base congeners as promiscuous oxidants of water pollutants. *Inorganic Chemistry,* 56**,** 14936-14947.

DE SOUSA, D. P., WEGEBERG, C., VAD, M. S., MØRUP, S., FRANDSEN, C., DONALD, W. A. & MCKENZIE, C. J. 2016. Halogen-bonding-assisted iodosylbenzene activation by a homogenous iron catalyst. *Chemistry – A European Journal,* 22**,** 3810-3820.

DEMETER, E. L., HILBURG, S. L., WASHBURN, N. R., COLLINS, T. J. & KITCHIN, J. R. 2014. Electrocatalytic oxygen evolution with an immobilized TAML activator. *Journal of the American Chemical Society,* 136**,** 5603-5606.

DRAKSHARAPU, A., ANGELONE, D., QUESNE, M. G., PADAMATI, S. K., GÓMEZ, L., HAGE, R., COSTAS, M., BROWNE, W. R. & DE VISSER, S. P. 2015. Identification and spectroscopic characterization of nonheme iron(III)

hypochlorite intermediates. *Angewandte Chemie International Edition,* 54**,** 4357-4361.

DUESTERBERG, C. K., COOPER, W. J. & WAITE, T. D. 2005. Fenton-mediated oxidation in the presence and absence of oxygen. *Environmental Science & Technology,* 39**,** 5052-5058.

EISENBERG, G. 1943. Colorimetric determination of hydrogen peroxide. *Industrial & Engineering Chemistry Analytical Edition,* 15**,** 327-328.

ELLIS, W. C., MCDANIEL, N. D., BERNHARD, S. & COLLINS, T. J. 2010. Fast water oxidation using iron. *Journal of the American Chemical Society,* 132**,** 10990-10991.

ENGELMANN, X., MONTE-PÉREZ, I. & RAY, K. 2016. Oxidation reactions with bioinspired mononuclear mon-heme metal-oxo complexes. *Angewandte Chemie-International Edition,* 55**,** 7632-7649.

FENTON, H. J. H. 1894. Oxidation of tartaric acid in presence of iron. *Journal of the Chemical Society, Transactions,* 65**,** 899-910.

FONTAINE, B., DROSOS, M. & MAZZEI, P. 2014. Copolymerization of 2,4-dichlorophenol with humic substances by oxidative and photo-oxidative biomimetic catalysis. *Environmental Science and Pollution Research,* 21**,** 8016-8024.

FONTAINE, B. & PICCOLO, A. 2012. Co-polymerization of penta-halogenated phenols in humic substances by catalytic oxidation using biomimetic catalysis. *Environmental Science and Pollution Research,* 19**,** 1485-1493.

FUKUSHIMA, M., ICHIKAWA, H., KAWASAKI, M., SAWADA, A., MORIMOTO, K. & TATSUMI, K. 2003a. Effects of humic substances on the pattern of oxidation products of pentachlorophenol induced by a biomimetic catalytic system using tetra(*p*-sulfophenyl)porphineiron(III) and $KHSO_5$. *Environmental Science & Technology,* 37**,** 386-394.

FUKUSHIMA, M., SAWADA, A., KAWASAKI, M., ICHIKAWA, H., MORIMOTO, K., TATSUMI, K. & AOYAMA, M. 2003b. Influence of humic substances on the removal of pentachlorophenol by a biomimetic catalytic system with a water-soluble iron (III) - Porphyrin complex. *Environmental Science & Technology,* 37**,** 1031-1036.

FUKUSHIMA, M., SHIGEMATSU, S. & NAGAO, S. 2010. Influence of humic acid type on the oxidation products of pentachlorophenol using hybrid catalysts prepared by introducing iron(III)-5,10,15,20-tetrakis(*p*-hydroxyphenyl) porphyrin into hydroquinone-derived humic acids. *Chemosphere,* 78**,** 1155-1159.

GALLARD, H., DE LAAT, J. & LEGUBE, B. 1999. Spectrophotometric study of the formation of iron(III)-hydroperoxy complexes in homogeneous aqueous solutions. *Water Research,* 33**,** 2929-2936.

GARG, S., ROSE, A. L. & WAITE, T. D. 2007. Production of reactive oxygen species on photolysis of dilute aqueous quinone solutions. *Photochemistry and Photobiology,* 83**,** 904-913.

GAZI, S., RAJAKUMAR, A. & SINGH, N. D. P. 2010. Photodegradation of organic dyes in the presence of [Fe(III)-salen]Cl complex and H_2O_2 under visible light irradiation. *Journal of Hazardous Materials,* 183**,** 894-901.

GHOSH, A., DE OLIVEIRA, F. T., YANO, T., NISHIOKA, T., BEACH, E. S., KINOSHITA, I., MÜNCK, E., RYABOV, A. D., HORWITZ, C. P. & COLLINS, T. J. 2005. Catalytically active μ-oxodiiron(IV) oxidants from iron(III) and dioxygen. *Journal of the American Chemical Society,* 127**,** 2505-2513.

GHOSH, A., MITCHELL, D. A., CHANDA, A., RYABOV, A. D., POPESCU, D. L., UPHAM, E. C., COLLINS, G. J. & COLLINS, T. J. 2008. Catalase-peroxidase activity of iron(III)-TAML activators of hydrogen peroxide. *Journal of the American Chemical Society,* 130**,** 15116-15126.

GHOSH, M., PATTANAYAK, S., DHAR, B. B., SINGH, K. K., PANDA, C. & SEN GUPTA, S. 2017. Selective C-H bond oxidation catalyzed by the Fe-bTAML complex: Mechanistic implications. *Inorganic Chemistry,* 56**,** 10852-10860.

GLAZE, W. H., KANG, J. W. & CHAPIN, D. H. 1987. The chemistry of water-treatment processes involving ozone, hydrogen-peroxide and ultraviolet-radiation. *Ozone-Science & Engineering,* 9**,** 335-352.

GROVES, J. T. & GILBERT, J. A. 1986. Electrochemical generation of an iron(IV) porphyrin. *Inorganic Chemistry,* 25**,** 123-125.

GROVES, J. T., HAUSHALTER, R. C., NAKAMURA, M., NEMO, T. E. & EVANS, B. J. 1981. High-valent iron-porphyrin complexes related to peroxidase and cytochrome P-450. *Journal of the American Chemical Society,* 103**,** 2884-2886.

GROVES, J. T., NEMO, T. E. & MYERS, R. S. 1979. Hydroxylation and epoxidation catalyzed by iron-porphine complexes. Oxygen transfer from iodosylbenzene. *Journal of the American Chemical Society,* 101**,** 1032-1033.

GU, Z. Y., PARK, J., RAIFF, A., WEI, Z. W. & ZHOU, H. C. 2014. Metal-organic frameworks as biomimetic catalysts. *Chemcatchem,* 6**,** 67-75.

HAHN, D., COZZOLINO, A., PICCOLO, A. & ARMENANTE, P. M. 2007. Reduction of 2,4-dichlorophenol toxicity to Pseudomonas putida after oxidative incubation with humic substances and a biomimetic catalyst. *Ecotoxicology and Environmental Safety,* 66**,** 335-342.

HALMA, M., CASTRO, K., PRÉVOT, V., FORANO, C., WYPYCH, F. & NAKAGAKI, S. 2009. Immobilization of anionic iron(III) porphyrins into ordered macroporous layered double hydroxides and investigation of catalytic activity in oxidation reactions. *Journal of Molecular Catalysis a-Chemical,* 310**,** 42-50.

HAN, A.-R., JIN JEONG, Y., KANG, Y., YOON LEE, J., SOOK SEO, M. & NAM, W. 2008. Direct evidence for an iron(IV)-oxo porphyrin π-cation radical as an active oxidant in catalytic oxygenation reactions. *Chemical Communications***,** 1076-1078.

HAN, J. E. S. & CHAO, T. Y. 1932. Carbonate content of volumetric sodium hydroxide solutions. *Industrial & Engineering Chemistry Analytical Edition,* 4**,** 229-232.

HAN, Z. B., HAN, X., ZHAO, X. M., YU, J. T. & XU, H. 2016. Iron phthalocyanine supported on amidoximated PAN fiber as effective catalyst for controllable hydrogen peroxide activation in oxidizing organic dyes. *Journal of Hazardous Materials,* 320**,** 27-35.

HANANIA, G. I. H., IRVINE, D. H., EATON, W. A. & GEORGE, P. 1967. Thermodynamic aspects of the potassium hexacyanoferrate(III)-(II) system. II. Reduction potential. *The Journal of Physical Chemistry,* 71**,** 2022-2030.

HESSENAUER-ILICHEVA, N., FRANKE, A., MEYER, D., WOGGON, W.-D. & VAN ELDIK, R. 2007. Low-temperature rapid-scan detection of reactive intermediates in epoxidation reactions catalyzed by a new enzyme mimic of cytochrome p450. *Journal of the American Chemical Society,* 129**,** 12473-12479.

HU, J., LIU, H., WANG, L., LI, N., XU, T., LU, W., ZHU, Z. & CHEN, W. 2016. Electronic properties of carbon nanotubes linked covalently with iron phthalocyanine to determine the formation of high-valent iron intermediates or hydroxyl radicals. *Carbon,* 100**,** 408-416.

HUONG LE, T. X., BECHELANY, M. & CRETIN, M. 2017. Carbon felt based-electrodes for energy and environmental applications: A review. *Carbon,* 122**,** 564-591.

IANNI, J. C. 2014. Kintecus, Windows Version 5.20. *www.kintecus.com*.

JEON, S. & BRUICE, T. C. 1992. Redox chemistry of water-soluble iron, manganese, and chromium metalloporphyrins and acid-base behavior of their lyate axial ligands in aqueous solution: influence of electronic effects. *Inorganic Chemistry,* 31**,** 4843-4848.

JOO, S. H., FEITZ, A. J. & WAITE, T. D. 2004. Oxidative degradation of the carbothioate herbicide, molinate, using nanoscale zero-valent iron. *Environmental Science & Technology,* 38**,** 2242-2247.

KANAKARAJU, D., GLASS, B. D. & OELGEMOLLER, M. 2014. Titanium dioxide photocatalysis for pharmaceutical wastewater treatment. *Environmental Chemistry Letters,* 12**,** 27-47.

KIWI, J., LOPEZ, A. & NADTOCHENKO, V. 2000. Mechanism and kinetics of the OH-radical intervention during fenton oxidation in the presence of a significant amount of radical scavenger (Cl^-). *Environmental Science & Technology,* 34**,** 2162-2168.

KUMAR, D., LATIFI, R., KUMAR, S., RYBAK-AKIMOVA, E. V., SAINNA, M. A. & DE VISSER, S. P. 2013. Rationalization of the barrier height for *p*-Z-styrene epoxidation by iron(IV)-oxo porphyrin cation radicals with variable axial ligands. *Inorganic Chemistry,* 52**,** 7968-7979.

KUNDU, S., CHANDA, A., THOMPSON, J. V. K., DIABES, G., KHETAN, S. K., RYABOV, A. D. & COLLINS, T. J. 2015. Rapid degradation of oxidation resistant nitrophenols by TAML activator and H_2O_2. *Catalysis Science & Technology,* 5**,** 1775-1782.

KURNIAWAN, T. A. & LO, W.-H. 2009. Removal of refractory compounds from stabilized landfill leachate using an integrated H_2O_2 oxidation and granular activated carbon (GAC) adsorption treatment. *Water Research,* 43**,** 4079-4091.

KWAN, W. P. & VOELKER, B. M. 2002. Decomposition of hydrogen peroxide and organic compounds in the presence of dissolved iron and ferrihydrite. *Environmental Science & Technology,* 36**,** 1467-1476.

LEI, J. P., JU, H. X. & IKEDA, O. 2004. Catalytic oxidation of nitric oxide and nitrite mediated by water-soluble high-valent iron porphyrins at an ITO electrode. *Journal of Electroanalytical Chemistry,* 567**,** 331-338.

LENNARTSON, A. & MCKENZIE, C. J. 2012. An iron(III) iodosylbenzene complex: A masked non-heme $Fe^{V}O$. *Angewandte Chemie-International Edition,* 51**,** 6767-6770.

LI, X., HOU, Y., ZHAO, Q. & WANG, L. 2011. A general, one-step and template-free synthesis of sphere-like zinc ferrite nanostructures with enhanced photocatalytic activity for dye degradation. *Journal of Colloid and Interface Science,* 358**,** 102-108.

LIM, M. H., LEE, Y. J., GOH, Y. M., NAM, W. & KIM, C. 1999. Hydroxylation of aliphatic hydrocarbons with m-chloroperbenzoic acid catalyzed by electron-deficient iron(III) porphyrin complexes. *Bulletin of the Chemical Society of Japan,* 72**,** 707-713.

LISTER, M. W. & ROSENBLUM, P. 1963. The oxidation of sodium formate by sodium hypochlorite. *Canadian Journal of Chemistry,* 41**,** 2727-2729.

LIU, H. Y., BAO, S. X., CAI, Z. T., XU, T. F., LI, N., WANG, L. L., CHEN, H. X., LU, W. Y. & CHEN, W. X. 2017. A novel method for ultra-deep desulfurization of liquid fuels at room temperature. *Chemical Engineering Journal,* 317**,** 1092-1098.

MA, J. X., HE, D., COLLINS, R. N., HE, C. S. & WAITE, T. D. 2016. The tortoise versus the hare - Possible advantages of microparticulate zerovalent iron (mZVI) over nanoparticulate zerovalent iron (nZVI) in aerobic degradation of contaminants. *Water Research,* 105**,** 331-340.

MEHRJOUEI, M., MULLER, S. & MOLLER, D. 2015. A review on photocatalytic ozonation used for the treatment of water and wastewater. *Chemical Engineering Journal,* 263**,** 209-219.

MILLER, C. J., ROSE, A. L. & WAITE, T. D. 2009. Impact of natural organic matter on H_2O_2-mediated oxidation of Fe(II) in a simulated freshwater system. *Geochimica et Cosmochimica Acta,* 73**,** 2758-2768.

MILLER, C. J., ROSE, A. L. & WAITE, T. D. 2011. Phthalhydrazide chemiluminescence method for determination of hydroxyl radical production: Modifications and adaptations for use in natural systems. *Analytical Chemistry,* 83**,** 261-268.

MILLER, C. J., ROSE, A. L. & WAITE, T. D. 2016. Importance of iron complexation for Fenton-mediated hydroxyl radical production at circumneutral pH. *Frontiers in Marine Science,* 3.

MILLER, C. J., YU, H. & WAITE, T. D. 2013. Degradation of rhodamine B during visible light photocatalysis employing Ag@AgCl embedded on reduced graphene oxide. *Colloids and Surfaces A: Physicochemical and Engineering Aspects,* 435**,** 147-153.

MILLS, M. R., BURTON, A. E., MORI, D. I., RYABOV, A. D. & COLLINS, T. J. 2015. Iron(IV) or iron(V)? Heterolytic or free radical? Oxidation pathways of a TAML activator in acetonitrile at −40 ℃. *Journal of Coordination Chemistry,* 68**,** 3046-3057.

MILLS, M. R., WEITZ, A. C., HENDRICH, M. P., RYABOV, A. D. & COLLINS, T. J. 2016. NaClO-generated iron(IV)oxo and iron(V)oxo TAMLs in pure water. *Journal of the American Chemical Society,* 138**,** 13866-13869.

MINKE, C., KUNZ, U. & TUREK, T. 2017. Carbon felt and carbon fiber - A techno-economic assessment of felt electrodes for redox flow battery applications. *Journal of Power Sources,* 342**,** 116-124.

MORRIS, J. C. 1966. The acid ionization constant of HOCl from 5 to 35 °. *The Journal of Physical Chemistry,* 70**,** 3798-3805.

NAM, W. 2007. High-valent iron(IV)-oxo complexes of heme and non-heme ligands in oxygenation reactions. *Accounts of Chemical Research,* 40**,** 522-531.

NAM, W., GOH, Y. M., LEE, Y. J., LIM, M. H. & KIM, C. 1999. Biomimetic alkane hydroxylations by an iron(III) porphyrin complex with H_2O_2 and by a high-valent iron(IV) oxo porphyrin cation radical complex. *Inorganic Chemistry,* 38**,** 3238-3240.

NAM, W., JIN, S. W., LIM, M. H., RYU, J. Y. & KIM, C. 2002. Anionic ligand effect on the nature of epoxidizing intermediates in iron porphyrin complex-catalyzed epoxidation reactions. *Inorganic Chemistry,* 41**,** 3647-3652.

NAM, W., LEE, Y. M. & FUKUZUMI, S. 2014. Tuning reactivity and mechanism in oxidation reactions by mononuclear nonheme iron(IV)-oxo complexes. *Accounts of Chemical Research,* 47**,** 1146-1154.

NEBE, T., BEITAT, A., WURTELE, C., DUCKER-BENFER, C., VAN ELDIK, R., MCKENZIE, C. J. & SCHINDLER, S. 2010. Reinvestigation of the formation of a mononuclear Fe(III) hydroperoxido complex using high pressure kinetics. *Dalton Transactions,* 39**,** 7768-7773.

NETA, P., HUIE, R. E. & ROSS, A. B. 1988. Rate constants for reactions of inorganic radicals in aqueous solution. *Journal of Physical and Chemical Reference Data,* 17**,** 1027-1284.

NIDHEESH, P. V. & RAJAN, R. 2016. Removal of rhodamine B from a water medium using hydroxyl and sulphate radicals generated by iron loaded activated carbon. *Rsc Advances,* 6**,** 5330-5340.

OSZAJCA, M., FRANKE, A., DRZEWIECKA-MATUSZEK, A., BRINDELL, M., STOCHEL, G. & VAN ELDIK, R. 2014. Temperature and pressure effects on C-H abstraction reactions involving compound I and II mimics in aqueous solution. *Inorganic Chemistry,* 53**,** 2848-2857.

PAILLARD, H., BRUNET, R. & DORE, M. 1988. Optimal conditions for applying an ozone-hydrogen peroxide oxidizing system. *Water Research,* 22**,** 91-103.

PHAM, A. N., ROSE, A. L., FEITZ, A. J. & WAITE, T. D. 2006. Kinetics of Fe(III) precipitation in aqueous solutions at pH 6.0–9.5 and 25 ℃. *Geochimica et Cosmochimica Acta,* 70**,** 640-650.

PIGNATELLO, J. J., OLIVEROS, E. & MACKAY, A. 2006. Advanced oxidation processes for organic contaminant destruction based on the Fenton reaction and related chemistry. *Critical Reviews in Environmental Science and Technology,* 36**,** 1-84.

POPESCU, D. L., VRABEL, M., BRAUSAM, A., MADSEN, P., LENTE, G., FABIAN, I., RYABOV, A. D., VAN ELDIK, R. & COLLINS, T. J. 2010. Thermodynamic, electrochemical, high-pressure kinetic, and mechanistic studies

of the formation of oxo Fe^{IV}-TAML species in water. *Inorganic Chemistry,* 49**,** 11439-11448.

POURAN, S. R., RAMAN, A. A. A. & DAUD, W. 2014. Review on the application of modified iron oxides as heterogeneous catalysts in Fenton reactions. *Journal of Cleaner Production,* 64**,** 24-35.

QUE, L. & TOLMAN, W. B. 2008. Biologically inspired oxidation catalysis. *Nature,* 455**,** 333-340.

RITTLE, J. & GREEN, M. T. 2010. Cytochrome P450 compound I: Capture, characterization, and C-H bond activation kinetics. *Science,* 330**,** 933-937.

RUTKOWSKA-ZBIK, D., DRZEWIECKA-MATUSZEK, A. & WITKO, M. 2014. The influence of structural parameters on the reactivity of model complexes for Compound II: A mini review. *Topics in Catalysis,* 57**,** 946-952.

RYABOV, A. D. 2013. Green challenges of catalysis via iron(IV)oxo and iron(V)oxo species. *In:* VANELDIK, R. & HUBBARD, C. D. (eds.) *Advances in Onorganic Chemistry, Vol 65: Homogeneous Catalysis.*

SAHERFIELD, C. N. & BONNELL, A. H. 1955. Interferences in the titanium sulfate method for hydrogen peroxide. *Analytical Chemistry,* 27**,** 1174-1175.

SATHISHKUMAR, P., MANGALARAJA, R. V. & ANANDAN, S. 2016. Review on the recent improvements in sonochemical and combined sonochemical oxidation processes - A powerful tool for destruction of environmental contaminants. *Renewable & Sustainable Energy Reviews,* 55**,** 426-454.

SAUER, M. C., BROWN, W. G. & HART, E. J. 1984. Oxygen(^{3}P) atom formation by the photolysis of hydrogen peroxide in alkaline aqueous solutions. *The Journal of Physical Chemistry,* 88**,** 1398-1400.

SCHILLER, J., ARNHOLD, J., SCHWINN, J., SPRINZ, H., BREDE, O. & ARNOLD, K. 1999. Differences in the reactivity of phthalic hydrazide and luminol with hydroxyl radicals. *Free Radical Research,* 30**,** 45-57.

SEN GUPTA, S., STADLER, M., NOSER, C. A., GHOSH, A., STEINHOFF, B., LENOIR, D., HORWITZ, C. P., SCHRAMM, K. W. & COLLINS, T. J. 2002. Rapid total destruction of chlorophenols by activated hydrogen peroxide. *Science,* 296**,** 326-328.

SHAPPELL, N. W., VRABEL, M. A., MADSEN, P. J., HARRINGTON, G., BILLEY, L. O., HAKK, H., LARSEN, G. L., BEACH, E. S., HORWITZ, C. P., RO, K., HUNT, P. G. & COLLINS, T. J. 2008. Destruction of estrogens using Fe-TAML/peroxide catalysis. *Environmental Science & Technology,* 42**,** 1296-1300.

SHEN, L. Q., BEACH, E. S., XIANG, Y., TSHUDY, D. J., KHANINA, N., HORWITZ, C. P., BIER, M. E. & COLLINS, T. J. 2011. Rapid, biomimetic degradation in

water of the persistent drug sertraline by TAML catalysts and hydrogen peroxide. *Environmental Science & Technology,* 45**,** 7882-7887.

SHENG, Y., SUN, Y., XU, J., ZHANG, J. & HAN, Y.-F. 2018. Fenton-like degradation of rhodamine B over highly durable Cu-embedded alumina: Kinetics and mechanism. *AIChE Journal,* 64**,** 538-549.

SIRES, I., BRILLAS, E., OTURAN, M. A., RODRIGO, M. A. & PANIZZA, M. 2014. Electrochemical advanced oxidation processes: today and tomorrow. A review. *Environmental Science and Pollution Research,* 21**,** 8336-8367.

ŠMEJKALOVÁ, D. & PICCOLO, A. 2006. Rates of oxidative coupling of humic phenolic monomers catalyzed by a biomimetic iron-porphyrin. *Environmental Science & Technology,* 40**,** 1644-1649.

ŠMEJKALOVÁ, D., PICCOLO, A. & SPITELLER, M. 2006. Oligomerization of humic phenolic monomers by oxidative coupling under biomimetic catalysis. *Environmental Science & Technology,* 40**,** 6955-6962.

TANG, L. L., GUNDERSON, W. A., WEITZ, A. C., HENDRICH, M. P., RYABOV, A. D. & COLLINS, T. J. 2015. Activation of dioxygen by a TAML activator in reverse micelles: Characterization of an $Fe^{III}Fe^{IV}$ dimer and associated catalytic chemistry. *Journal of the American Chemical Society,* 137**,** 9704-9715.

TIAGO DE OLIVEIRA, F., CHANDA, A., BANERJEE, D., SHAN, X., MONDAL, S., QUE, L., JR., BOMINAAR, E. L., MUNCK, E. & COLLINS, T. J. 2007. Chemical and spectroscopic evidence for an Fe^{V}-oxo complex. *Science,* 315**,** 835-838.

TIONG, T. J. & PRICE, G. J. 2012. Ultrasound promoted reaction of Rhodamine B with sodium hypochlorite using sonochemical and dental ultrasonic instruments. *Ultrasonics Sonochemistry,* 19**,** 358-364.

TRUONG, L., DENARDO, M. A., KUNDU, S., COLLINS, T. J. & TANGUAY, R. L. 2013. Zebrafish assays as developmental toxicity indicators in the green design of TAML oxidation catalysts. *Green Chemistry,* 15**,** 2339-2343.

TU, W. W., LEI, J. P., JIAN, G. Q., HU, Z. & JU, H. X. 2010. Noncovalent assembly of picket-fence porphyrins on nitrogen-doped carbon nanotubes for highly efficient catalysis and biosensing. *Chemistry-a European Journal,* 16**,** 4120-4126.

VAD, M. S., LENNARTSON, A., NIELSEN, A., HARMER, J., MCGRADY, J. E., FRANDSEN, C., MORUP, S. & MCKENZIE, C. J. 2012. An aqueous non-heme Fe(IV)oxo complex with a basic group in the second coordination sphere. *Chemical Communications,* 48**,** 10880-10882.

VAD, M. S., NIELSEN, A., LENNARTSON, A., BOND, A. D., MCGRADY, J. E. & MCKENZIE, C. J. 2011. Switching on oxygen activation by cobalt complexes of pentadentate ligands. *Dalton Transactions,* 40**,** 10698-10707.

VILHUNEN, S. & SILLANPAA, M. 2010. Recent developments in photochemical and chemical AOPs in water treatment: a mini-review. *Reviews in Environmental Science and Bio-Technology,* 9**,** 323-330.

WALLING, C., PARTCH, R. E. & WEIL, T. 1975. Kinetics of the decomposition of hydrogen peroxide catalyzed by ferric ethylenediaminetetraacetate complex. *Proceedings of the National Academy of Sciences,* 72**,** 140-142.

WANG, J. H., SUN, H. & ZHAO, X. S. 2010. Electrochemical catalysis and stability of tetraamido macrocyclic ligands iron immobilized on modified pyrolytic graphite electrode. *Catalysis Today,* 158**,** 263-268.

WANG, L. L., LU, W. Y., NI, D. J., XU, T. F., LI, N., ZHU, Z. X., CHEN, H. X. & CHEN, W. X. 2017. Solar-initiated photocatalytic degradation of carbamazepine on excited-state hexadecachlorophthalocyanine in the presence of peroxymonosulfate. *Chemical Engineering Journal,* 330**,** 625-634.

WEGEBERG, C., LAURITSEN, F. R., FRANDSEN, C., MORUP, S., BROWNE, W. R. & MCKENZIE, C. J. 2018. Directing a Non-Heme Iron(III)-Hydroperoxide Species on a Trifurcated Reactivity Pathway. *Chemistry-a European Journal,* 24**,** 5134-5145.

WINGATE, K. G., STUTHRIDGE, T. R., WRIGHT, L. J., HORWITZ, C. P. & COLLINS, T. J. 2004. Application of TAML® catalysts to remove colour from pulp and paper mill effluents. *Water Science and Technology,* 49**,** 255-260.

WU, F., HUANG, H. W., XU, T. F., LU, W. Y., LI, N. & CHEN, W. X. 2017. Visible-light-assisted peroxymonosulfate activation and mechanism for the degradation of pharmaceuticals over pyridyl-functionalized graphitic carbon nitride coordinated with iron phthalocyanine. *Applied Catalysis B-Environmental,* 218**,** 230-239.

YUAN, G., ZHANG, G., ZHOU, Y. & YANG, F. 2015. Synergetic adsorption and catalytic oxidation performance originating from leafy graphite nanosheet anchored iron(II) phthalocyanine nanorods for efficient organic dye degradation. *RSC Advances,* 5**,** 26132-26140.

ZHU, Z. X., LU, W. Y., LI, N., XU, T. F. & CHEN, W. X. 2017. Pyridyl-containing polymer blends stabilized iron phthalocyanine to degrade sulfonamides by enzyme-like process. *Chemical Engineering Journal,* 321**,** 58-66.

Appendix 1.
Cyclic voltametric analysis of homogeneous Fe-TAML

Cyclic Voltammetry (CV) for homogeneous Fe-TAML (in 0.1 M $NaClO_4$) was conducted using the 3-eletrode setup consisting of a blank glassy carbon working electrode, a platinum counter electrode and a Ag/AgCl (3 M KCl) reference electrode at room temperature and uncontrolled pH of ~6.5.

Fe-TAML concentrations used were 100 µM and 200 µM, which are much higher than the heterogeneous study where an equivalent Fe-TAML loading of ~4.1 µM was used. However, the anodic current peaks, that seem to appear at ~0.8 V and ~1.2 V (*vs*. NHE), are weak and broad with no apparent corresponding cathodic peaks.

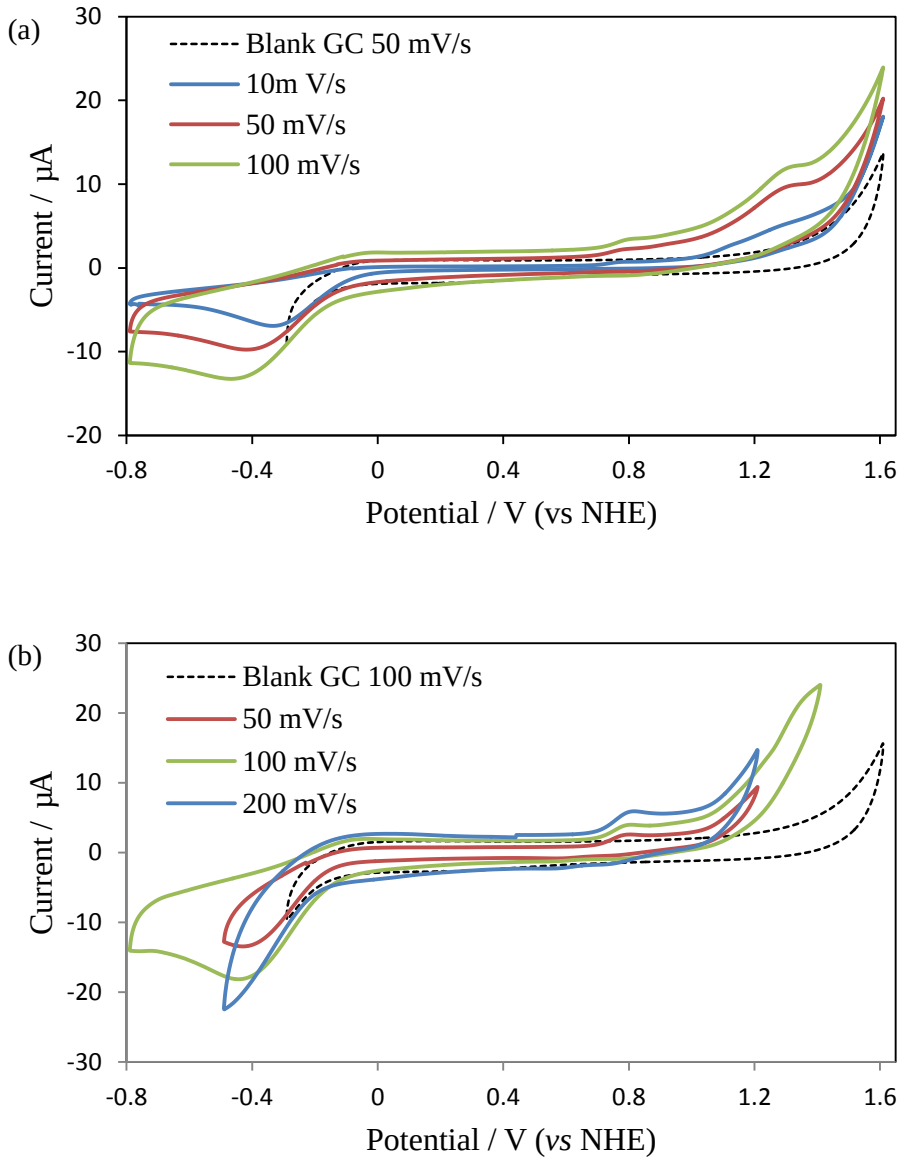

Figure A1-1. CVs of (a) 100 µM and (b) 200 µM Fe-TAML at different scan rates in 0.1M $NaClO_4$ without pH control.

Appendix 2.
Recovery factors for rhodamine B desorption from carbon materials by methanol

When investigating speciation of rhodamine B(RhB) degradation by electro-activated Fe-TAML/Graphite (FeTG), rhodamine species adsorbed on carbon felt electrode and graphite particles were washed out by methanol at the end of the experiment and quantified by UV spectra, which, together with the liquid phase data, gives the whole picture of RhB degradation products as shown in Figure 2-10. However, rhodamine species washed out by methanol in certain process would always end up with some losses due to the adsorption-desorption equilibrium in methanol. This is where the recovery factors used in section 2.3.4.2 are introduced, where all the rhodamine species are assumed to behave as RhB. Three recovery factors for carbon felt electrodes, blank graphite and the FeTG used in electrochemical experiments are measured respectively because of their different adsorbing capacity.

A2.1 Experimental method

Recovery factor experiments were conducted based on electrochemically RhB degradation experiments (section 2.2.4). For FeTG (or blank graphite), ~10 μM RhB and 25 mg FeTG (or blank graphite) were mixed in 20 mL 0.1 M $NaClO_4$ without pH control and stirred at room temperature for 150 min; the graphite sediment (separated from the suspension by centrifuge) was then soaked in 10 mL methanol for 30 minutes to extract adsorbed RhB. For carbon felt electrodes, two carbon felt electrodes were immersed in 20mL RhB solution (~10 μM, in 0.1 M $NaClO_4$) and stirred for 2 hours, which were then washed by 20 mL methanol in the same process. Initial RhB loading ($[RhB]_i$), RhB remained in the liquid phase ($[RhB]_L$) and washed out by methanol

($[RhB]_{MeOH}$) were measured by UV-vis spectrometer respectively for recovery factor calculation as below:

$$F = \frac{[RhB]_{MeOH} \times V_{MeOH} + [RhB]_L \times V_{initial}}{[RhB]_i \times V_{initial}}$$

A2.2 Results and discussion

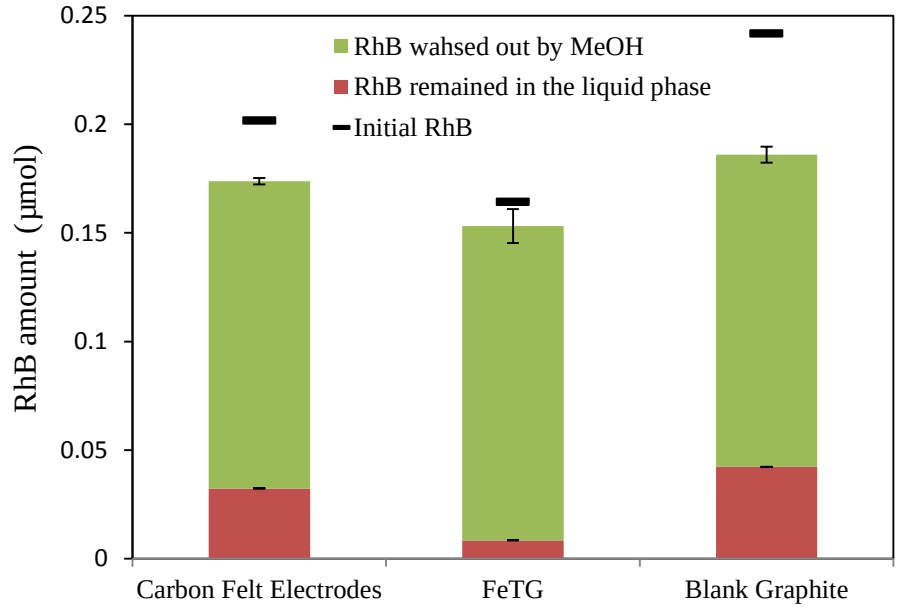

Figure A2-1 Measured RhB amount in the liquid phase (red column) and in different solid phases (green column) comparing to the initial RhB loading (black bars) in µmol.

As shown in Figure A2-1, a one-off methanol wash process can effectively release RhB from all solid phases, though blank graphite particles present the lowest recovery because of its strong absorbability to RhB molecules. FeTG, despite containing the same amount of graphite particles, have demonstrated a satisfying recovery.

Recovery factors were calculated from three repeated experiments. As stated in the main thesis, the methanol wash recovery factor for carbon felt, blank graphite particles and the FeTG used (Fe-TAML loading: 3.3µmol/g) are 83±1%, 72±2% and 93±5%, respectively.

Appendix 3.

The non-precursor model for H_2O_2/Fe-*tpena* System

A reactions scheme without the precursor ("Fe*tpena*H_2O_2") can not simulate the H_2O_2 consumptions or the observed substrate oxidation results from the experiments. The biggest problem for this non-precursor model is that with hydroxyl radicals generated 1:1 to Fe^{IV}-tpena, there is no way to simulate the measured formate degradation and H_2O_2 consumption at the same time because of the insufficient $HO^{\bullet}$ sink. When adjusting the unknown rate constants, it is possible to either obtain a good fit to the substrate decay data, or to the H_2O_2 degradation data, but never both with the same set of rate constants. There are no known or plausible reactions that could be considered to ameliorate this problem.

Table A3-1 shows a model that has been adjusted to provide a "best fit" for the formate oxidation data, however, the modelled H_2O_2 consumption is far too low compared to experimental data as shown in Figure A3-1. Although the model also provides a reasonable fit to theh Phth data, the Phth-OH fit cannot be obtained without changing the rate constant for $\mathbf{PhthOH} + \boldsymbol{Fe^{IV}tpena} \rightarrow \boldsymbol{Fe^{III}tpena} + \mathbf{PhthOx} + {}^{\bullet}\mathbf{O_2}^{-}$. to an unreasonably large value (as the best fit shown in Figure A3-2 when this value is set as 1×10^5 – which is $>10^3$ times larger than any other known reaction of Fe^{IV}-*tpena*).

If efforts are instead given to provide a good fit to the H_2O_2 data, the non-precursor mode (as listed in Table A3-2) can only obtain a "best" H_2O_2 fit as shown in Figure A3-3 and present an extravagant formate degradation which is against experimental results. In addition to this, this attempt cannot generate a good Phth/Phth-OH fit as the closest fits (but still poor) shown in Table A3-4.

In summary, there are important reactions missing in this model, and a reasonable mechanism is the formation of a peroxo complex with Fe^{III}-*tpena* as discussed in Chapter 4.

Table A3-1 Non-precursor model for the degradation of formate and Phth by H_2O_2 activated homogeneous Fe-*tpena* with a good-formate- but poor-H_2O_2-fit

Reaction	k ($M^{-1}\cdot s^{-1}$)	Comment
$Fe^{III}tpena + H_2O_2 \rightarrow HO^{\bullet} + Fe^{IV}tpena$ **(3)**	0.1	Fe-*tpena* activation and deactivation
$Fe^{IV}tpena + H_2O_2 \rightarrow Fe^{III}tpena + {}^{\bullet}O_2^-$ **(13)**	1×10^2	
$Fe^{IV}tpena + {}^{\bullet}O_2^- \rightarrow Fe^{III}tpena + O_2$ **(14)**	1×10^6	
Phth $+Fe^{IV}tpena \rightarrow Fe^{III}tpena +$ **PhthOx** $+ {}^{\bullet}O_2^-$ **(24)**	225[a]	Phth/Phth-OH oxidations
PhthOH $+Fe^{IV}tpena \rightarrow Fe^{III}tpena +$ **PhthOx** $+ {}^{\bullet}O_2^-$ **(25)**	1×10^5	
$HO^{\bullet}$ **+ Phth →** **PhthOH** $+ {}^{\bullet}O_2^-$ **(26)**	5.3×10^{9} [a]	
$HO^{\bullet}$ **+ PhthOH →** **PhthOx** $+ {}^{\bullet}O_2^-$ **(27)**	5.3×10^{9} [a]	
All the reactions in other groups and their rate constants remain the same with Table 4-2		

[a] same as Table 4-2

Table A3-2 Non-precursor model for the degradation of formate and Phth by H_2O_2 activated homogeneous Fe-*tpena* with a closest- H_2O_2- but poor-formate/Phth-fit

Reaction	k ($M^{-1}\cdot s^{-1}$)	Comment
$Fe^{III}tpena + H_2O_2 \rightarrow HO^{\bullet} + Fe^{IV}tpena$ **(3)**	15	Fe-*tpena* activation and deactivation
$Fe^{IV}tpena + H_2O_2 \rightarrow Fe^{III}tpena + {}^{\bullet}O_2^-$ **(13)**	15	
$Fe^{IV}tpena + {}^{\bullet}O_2^- \rightarrow Fe^{III}tpena + O_2$ **(14)**	500	
Phth $+Fe^{IV}tpena \rightarrow Fe^{III}tpena +$ **PhthOx** $+ {}^{\bullet}O_2^-$ **(24)**	0.5	Phth/Phth-OH oxidations
PhthOH $+Fe^{IV}tpena \rightarrow Fe^{III}tpena +$ **PhthOx** $+ {}^{\bullet}O_2^-$ **(25)**	0.5	
$HO^{\bullet}$ **+ Phth →** **PhthOH** $+ {}^{\bullet}O_2^-$ **(26)**	5.3×10^{9} [a]	
$HO^{\bullet}$ **+ PhthOH →** **PhthOx** $+ {}^{\bullet}O_2^-$ **(27)**	5.3×10^{9} [a]	
All the reactions in other groups and their rate constants remain the same with Table 4-2		

[a] same as Table 4-2

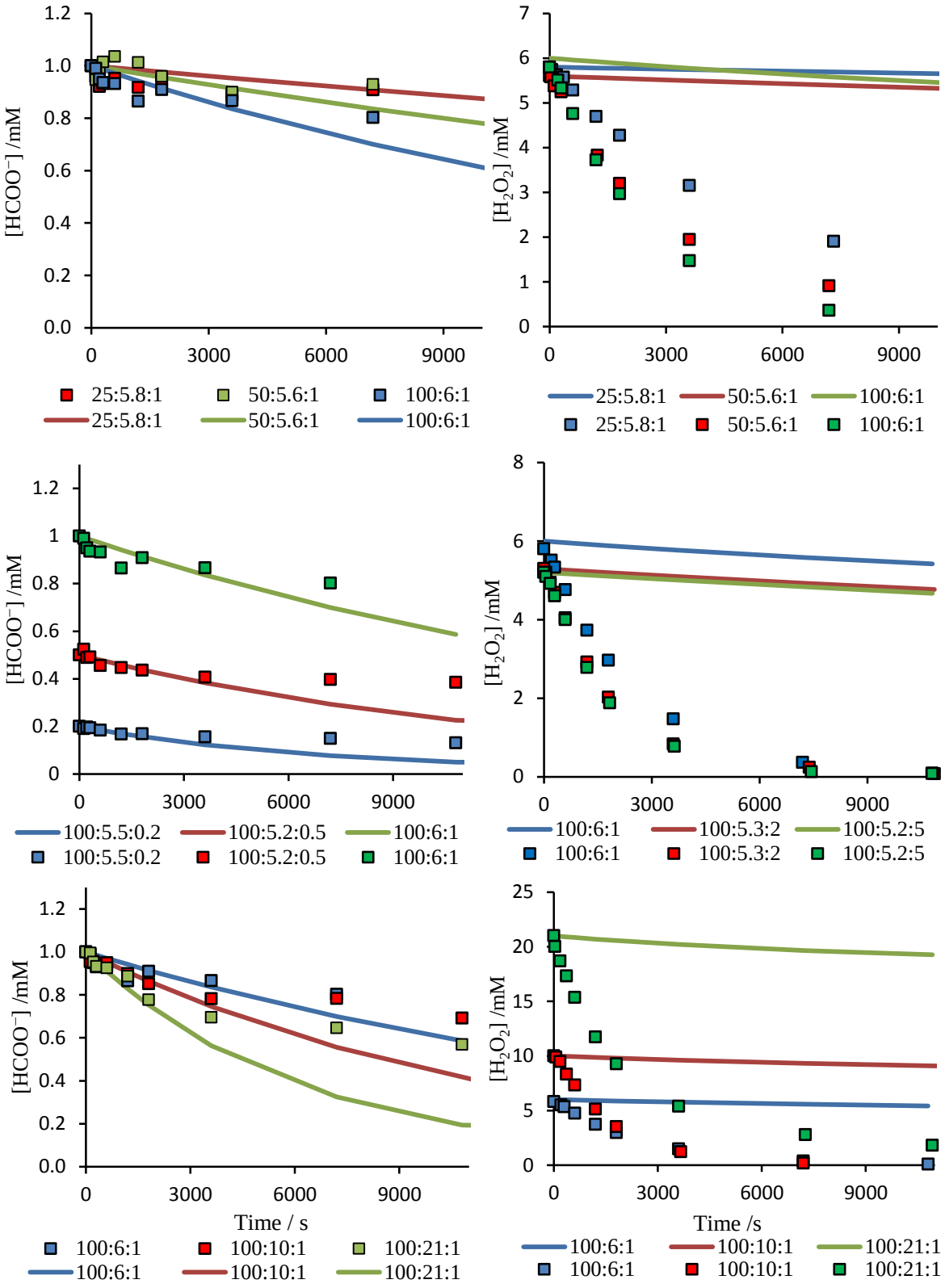

Figure A3-1 Experimental (squares) and modelled (from the non-precursor model listed in **Table A3-1**) (lines) formate/peroxide concentration change at different *Fe-tpena (*μM per Fe*) : peroxide(mM) : formate* (mM) ratios at pH 8.

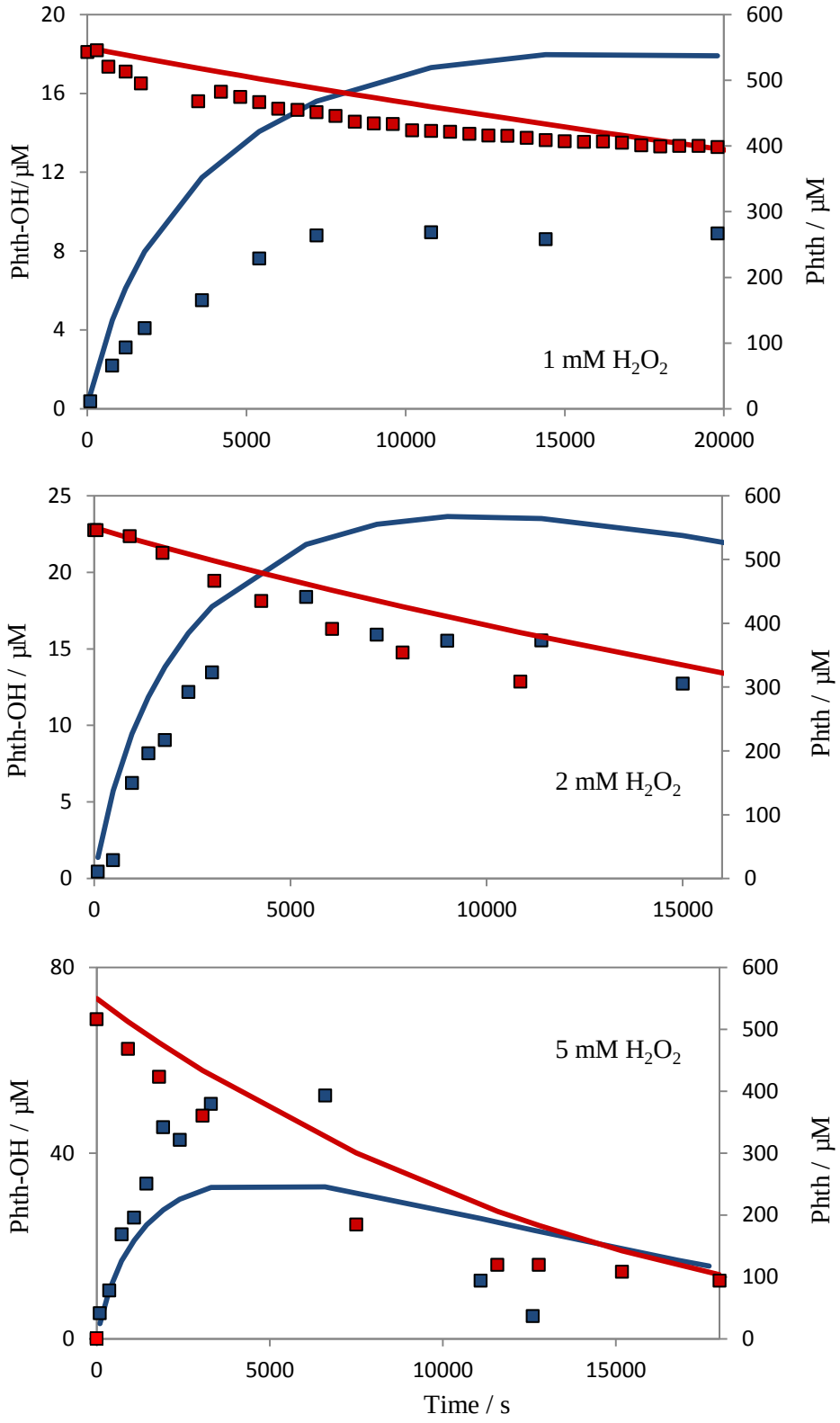

Figure A3-2 Experimental (squares) and modelled (from the non-precursor model listed in **Table A3-2**) (lines) Phth (red) and Phth-OH (blue) concentrations change when different amount of H_2O_2 is added to 100 µM Fe-*tpena* (per Fe) and 550 µM Phth at pH 8.

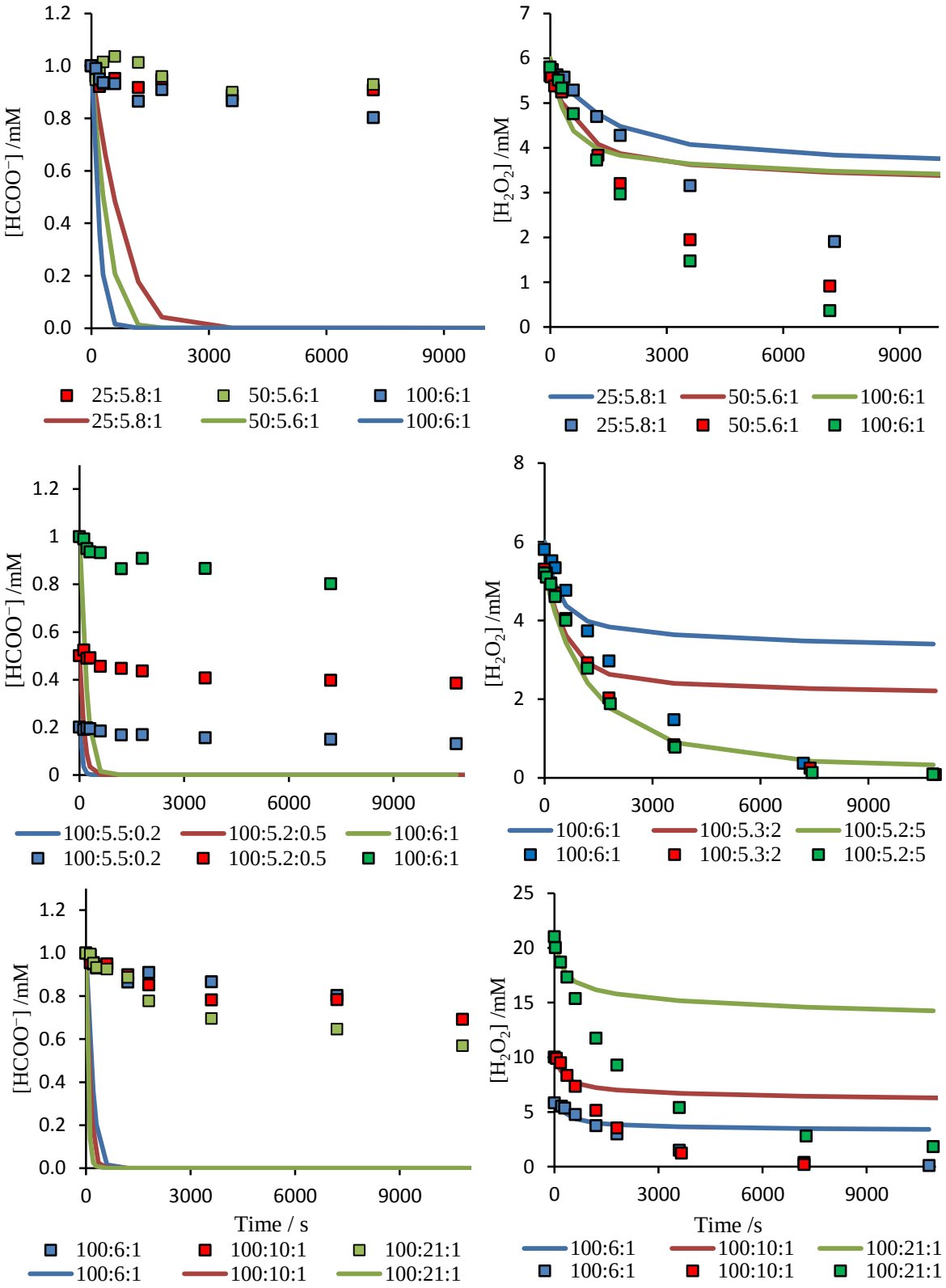

Figure A3-3 Experimental (squares) and modelled (from the non-precursor model listed in **Table A3-2**) (lines) formate/peroxide concentration change at different *Fe-tpena (*μM per Fe*) : peroxide(mM) : formate* (mM) ratios at pH 8.

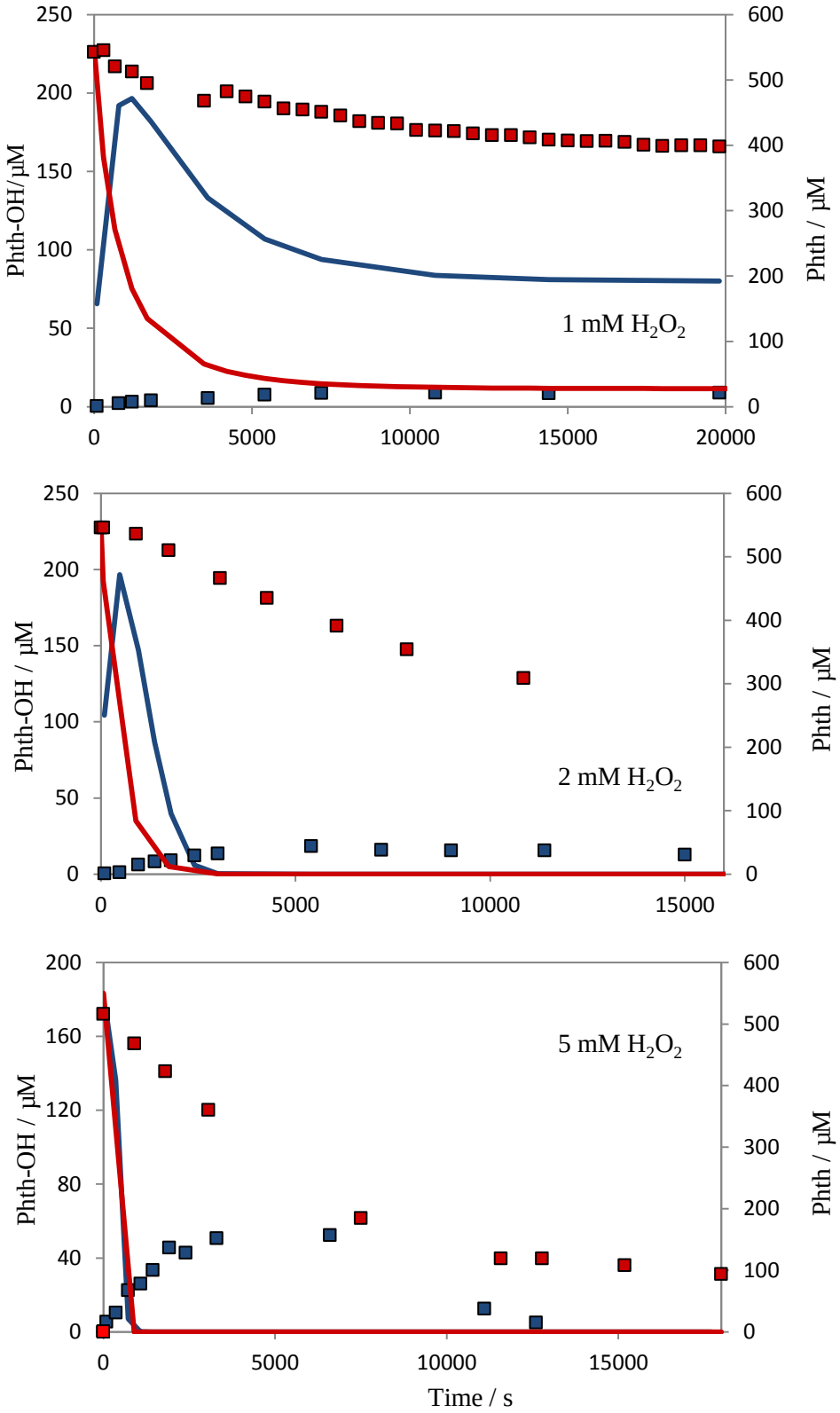

Figure A3-4 Experimental (squares) and modelled (from the non-precursor model listed in Table **A3-2**) (lines) Phth (red) and Phth-OH (blue) concentrations change when different amount of H_2O_2 is added to 100 µM Fe-*tpena* (per Fe) and 550 µM Phth at pH 8.

Appendix 4.

Oxidation of phthalhydrazide by hypochlorite

Adding NaClO (0.5 ~1.5 mM) to a phthalhydrazide- contained carbonate buffer results in an instant UV spectrum change as shown in the Figure A4-1, while H_2O_2 at a much higher dose (5 mM) does not incur obvious Phth oxidation (Figure A4-2).

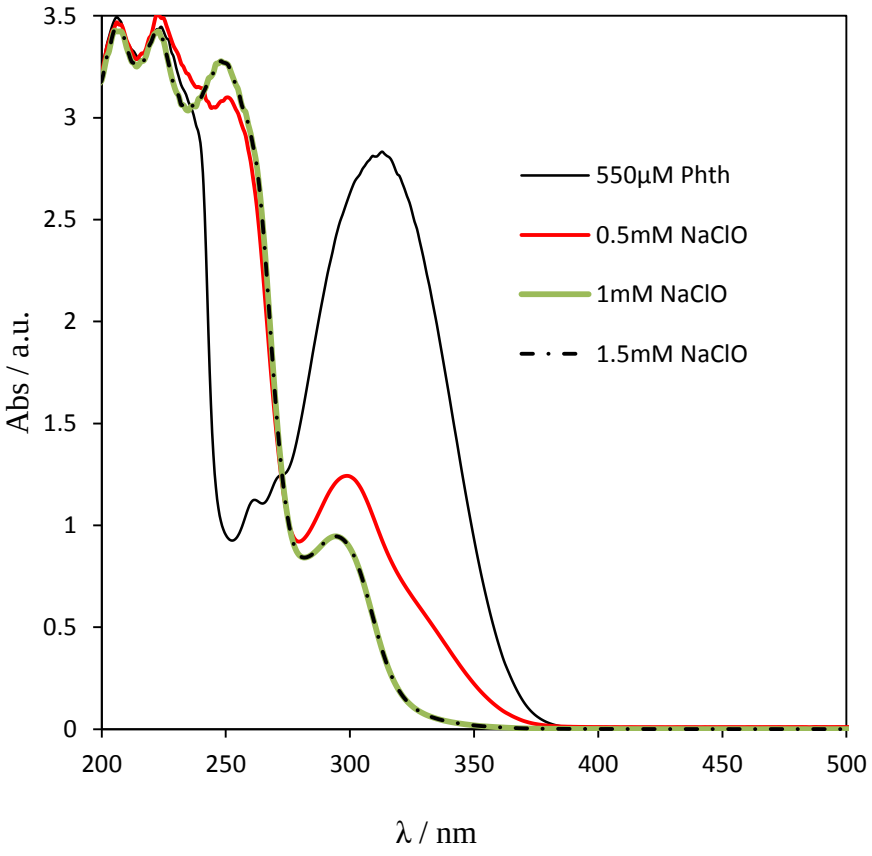

Figure A4-1 UV-vis spectra of 550 μM Phth (in 10 mM NaCl and 2 mM $NaHCO_3$) when different amount of NaClO (0, 0.5, 1 and 1.5 mM) was added

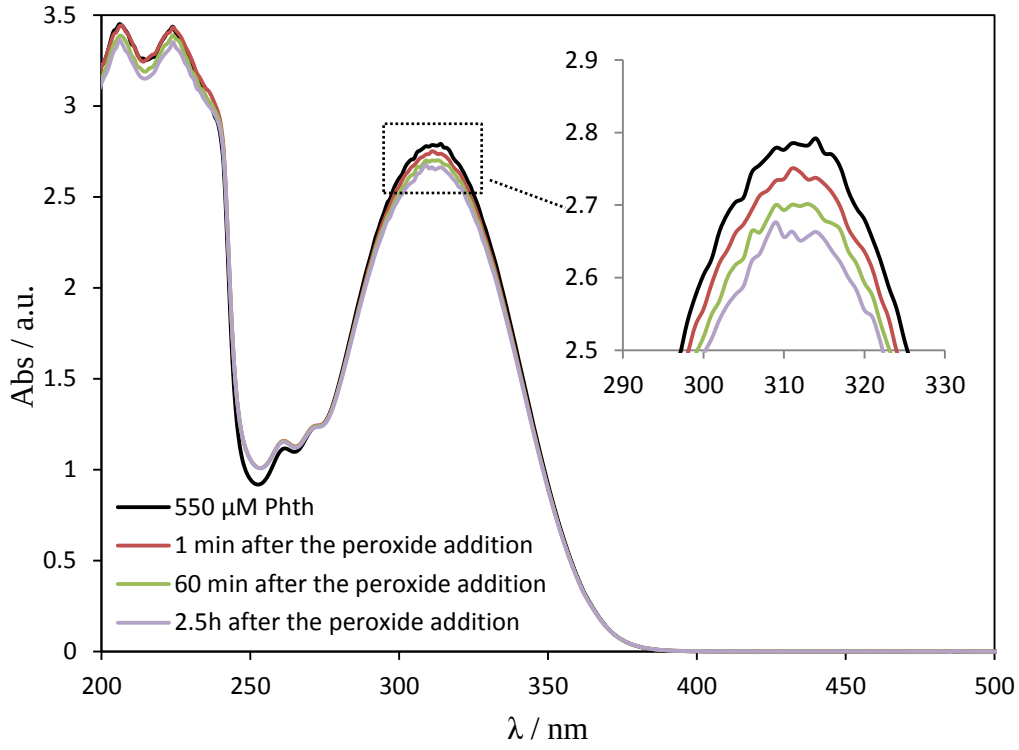

Figure A4-2 UV-vis spectrum of 550 µM Phth (in 10 mM NaCl and 2 mM $NaHCO_3$) and its change after 5 mM hydrogen peroxide was added

Appendix 5.

Formate degradation in the Fe-TAML/H_2O_2 system

5 mM H_2O_2 was added to 100 µM Fe-TAML – and 1 mM HCOONa – contained pH 9 carbonate buffer. ~10% $HCOO^-$ decrease was observed after 3 hours as shown in the following figure.

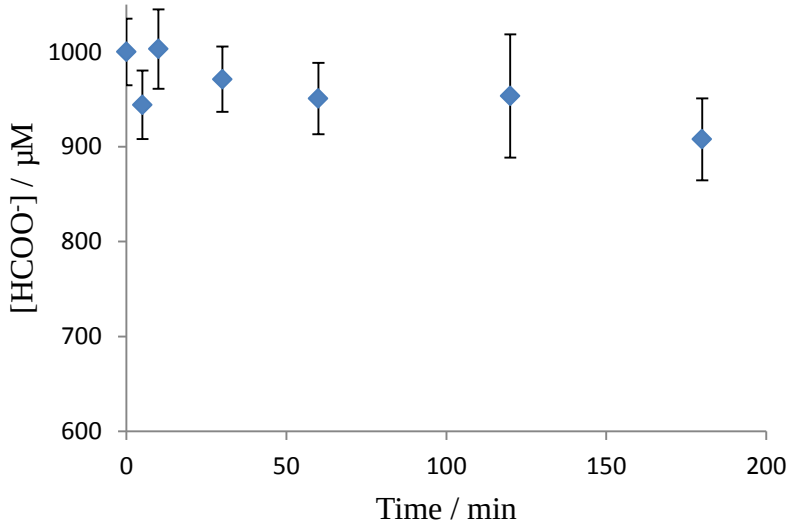

Figure A5-1. Variation of formate concentration with time when 5 mM H_2O_2 was added to 100 µM Fe-TAML and 1mM HCOONa in pH 9 carbonate buffer.